PDMS Deformation Effects during Start-up Flow in Microchannels of Different Depths and Containing Various Obstacles

by

Chan-Kyu Kang

A dissertation submitted to the Graduate Faculty of
Auburn University
in partial fulfillment of the
requirements for the Degree of
Doctor of Philosophy

Auburn, Alabama
May 6, 2013

Key words: PDMS bulging, friction factor, hydraulic diameter, obstacles, pressure drop, microfluidic channel

Approved by

Ruel A. Overfelt, Chair, Professor of Mechanical Engineering
Barton C. Prorok, Associate Professor of Mechanical Engineering
Dong-Joo Kim, Associate Professor of Mechanical Engineering
Leonardo De La Fuente, Assistant Professor of Entomology and Plant Pathology

Abstract

New experimental data for the microfluidic flow of a water-based liquid at very low Reynolds numbers (10^{-4} to 10^{-3}) are provided for an optically transparent polydimethylsiloxane (PDMS) microfluidic chip with rectangular flow channels obstructed by periodically arranged objects of varying shapes and sizes. Four obstacle shapes of circular, hexagonal, square and triangular contours with three characteristic dimensions of 132μm, 152μm and 172μm were fabricated within microchannels 243μm wide and depths of 15, 50, 100 and 200 μm. The flow velocity and applied pressure during the start-up flow of a water-based, colored liquid solution were directly measured by optical microscopy and a pressure transducer. The resultant CCD images and pressure data were used to determine the extent of the start-up transients and evaluate the establishment of quasi-steady flow conditions.

PDMS bulging was observed by fluorescence intensity differences at low flow rates. Microchannel bulging effects were found to be strongly affected by the pressure drop while being less affected by the flow velocity. As a result, the measured pressure drop increased less than 60% when the flow rate was doubled. The bulging modified mean hydraulic diameter, mean quasi-steady state flow velocity and pressure drop along the microfluidic channels were used to evaluate the Reynolds numbers and Darcy friction factors. The experimentally determined relationship between friction factor and Reynolds number indicated a much stronger dependence on Reynolds number than expected for the

15μm deep microchannels, even though the friction factor data from the current investigation were found to agree with literature data. Minimal elastic deformation of PDMS microfluidic channels was observed in the deepest channels and, the relationship between friction factor and Reynolds number agreed more closely with theoretical expectations for the deepest microchannels.

Experimental measurements of bulging displacements of the flexible PDMS microchannels using fluorescence microscopy provided a cost effective alternative method to confocal microscopy. Measurements of bulging agreed with theoretical predictions using both the simplified scaling analysis of Gervais et al. (2006) as well as 2D finite element simulations.

Acknowledgments

I sincerely thank my advisor, Dr. Ruel A. Overfelt, for his continuous effort of supervision and encouragement. Without his immense support and patience, it would not have been possible to finish the research work. I also would like to thank Dr. La Fuente for his full support to use fluorescence microscopy during the early research projects of my Ph.D. work. Sincere thanks go to my committee members: Dr. Barton C. Prorok and Dr. Dong-Joo Kim for their comments and suggestion on the proposal and dissertation.

I would like to express my deep gratitude to Dr. Tae-Hoon Kim, Dr. Jae-Jin Shim, Mr. Alfred Bennett, and Ms. Dorothy Heather for their strong support and advice related to this research and my life. I also would like to extend my gratitude to Mr. Steven Moore and Mr. L.C.Mathison (deceased) for their technical support and assistance in my research, and especially Ms. Amanda Davis who helped edit and proofread this dissertation. Sincere thanks are extended to my lab current and previous lab colleagues: Dr. Shih-Feng Chou, Mobbassarhassan Sk, John Andress and Amanda Neer.

Finally, I would love to express my great appreciation to my parents, my wife, and two sons for their endless love and support.

Table of Contents

List of Tables

List of Figures

List of Abbreviations

PDMS	Polydimethylsiloxane
MEMS	Microelectromechanical Systems
RIE	Reactive Ion etching
D_H	Hydraulic diameter
$\overline{D_H}$	The mean modified hydraulic diameter
$\overline{V}$	The mean fluid velocity
f	Darcy friction factor
Re	Reynolds number
ε	The aspect ratio
U_j	Individual uncertainty
U_G	The total uncertainty
ρ	The fluid density
μ	The dynamic viscosity
σ	The density of the solution
θ	The liquid/capillary contact angle
λ	Obstacle characteristic length
C*	The friction constant ratio
QS	Quasi Steady State

CHAPTER 1

INTRODUCTION

1.1 Background

Over the decades, microfluidic devices have demonstrated that their miniaturized components such as pumps, valves, mixers and reactors could be integrated together, leading to successful applications for chemical mixing, biochemical analysis and biomolecular separation. The “lab on a chip” concept in microfludics is similar to the way that a microelectronic circuit in a computer is on a single chip and aims to integrate many dynamics functions into a single device. These conceptual functions allow the increase of their efficiencies and eventually expanding their applications. One of the fascinating successful applications to biomedical instruments is the micro-pump, which delivers insulin into the liver for diabetic treatment. Classical fields of applications are flow property analysis, chemical reaction and drug delivery, with the advantages being fast response time, low sample and reagent consumption. Now, microfluidics devices are looking forward to exploring more advanced fields beyond current applications. The promising functional microfluidic devices can be applied to energy supply, thermal management and chemical production. However, these successful advances are based on the development of microfabrication technologies. Microfluidic devices equipped with sensors and actuators are generally made of silicon. The increasing material and processing costs become a hindrance to the success of silicon based devices for a

commercial market. Elastic materials such as polydimethylsiloxane (PDMS) have recently emerged as excellent alternatives to silicon because of their low production cost. The advent of PDMS has promptly replaced traditional silicon-based micro-machining technologies. Therefore, an appropriate understanding of such a paradigm shift in microfludic devices is very important to enable further advances. In addition, it is necessary to have a good understanding of the underlying physics in PDMS microfluidic devices.

This chapter begins with a general introduction in regard to several features of microfluidic devices (i.e. advantages and disadvantages), followed by PDMS chip microfabrication technologies and applicable general fluid mechanics theories. In addition, unexpected physical phenomena due to elastic deformation of PDMS can arise, so a review of the elastic material properties of PDMS is included in this chapter.

1.2 Microfluidics for "Lab on a Chip" applications

In the last decade, the number of microfluidics-related publications has increased by an order of magnitude and this trend is now shifting toward even smaller scales such as nanofluidics and multicomponent systems. The number of microfluidic publications is shown in Figure 1.1 (Nguyen and Werelry 2006). This trend indicates that microfluidics has received great interest even though microfluidic devices exhibit a number of complicated physical phenomena that are not easily understood. Many studies have explored their complicated behaviors, but unsolved questions still remain. The question confronting researchers is why microfluidics devices have become so attractive and promising in spite of these disadvantages in the fields of several areas. The huge amount

of investigations indicates that changing from macro-scale to micro-scale processes offers numerous advantages. In addition, the material property of PDMS itself provides undeniable economic benefits along with elastic material properties. These advantages are introduced in the following chapters.

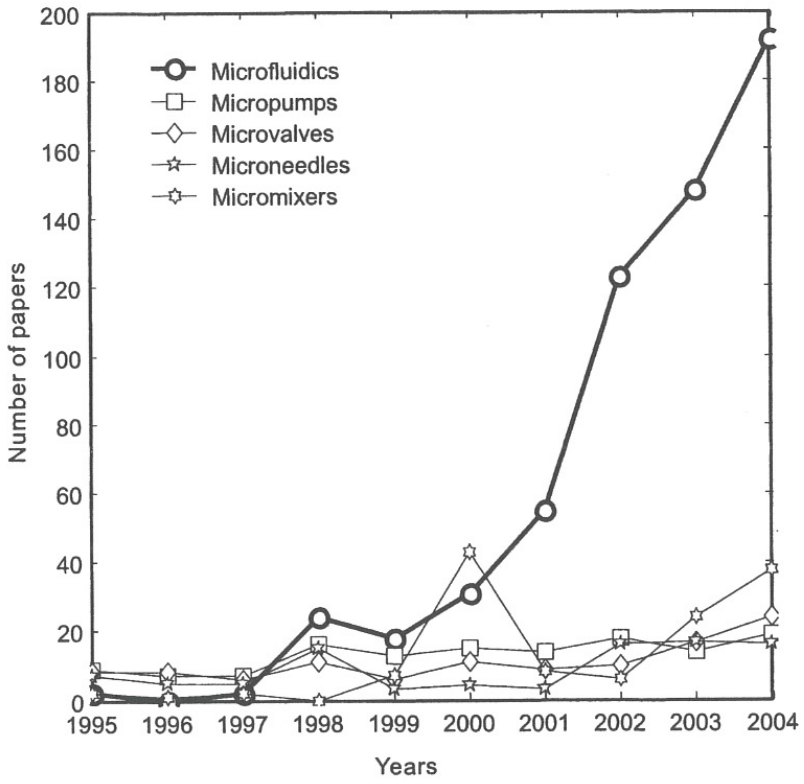

Figure 1.1 Publications of microfluidics-related papers (Nguyen and Werelry 2006)

One of the most obvious examples of such advantages is enzyme kinetic reaction using a microfluidics chip. This has miniaturized components and automated some of the work of microfluidic engineers. The small volumes of fluid that are used lead to reduced consumption of expensive reagents and enhanced response time. Small quantities of test samples are now used to apply screening assays because microfluidic devices provide very accurate sample control, which leads to reduced waste production.

Microfluidic devices with small components tend to have a large surface area- to-volume ratio. This characteristic feature facilitates rapid heat transfer and accurate temperature control as observed by Mello et al. (2004). Their investigation showed that a microfluidic device equipped with fluid heaters maintained its target temperature within 0.2°C using tiny transparent ionic liquids (~750pL per channel). Also, the large surface area to volume ratio has been utilized for solid-phase synthesis and enzyme kinetics. Figure 1.2 shows one of the outstanding examples for enzyme kinetic reaction to extract kinetic parameters from a single chip system (Yun et al. 2011). In this study, they used a micro- active mixer which enables sequential mixing valve and rapid mixing. Rapid mixing at small length scales is also important in the fields of biochemistry analysis, drug delivery and synthesis of nuclear acids because passive and active micro-mixers often accelerate the speed of chemical reaction by means of either external power supplies or complex geometries (Nguyen and Wu 2005). Passive mixers that operate without external power supply is a popular device used to get chaotic advection and mixing. Inserting various shapes of micro-obstacles inside microfluidic channels or rearranging micro-obstacles of microfludic channels increase recirculation and mixing (Wang et al. 2003; Cortes-Quiroz et al. 2010; Ansari et al 2010). In contrast to the passive mixer, the active mixer requires external power sources. Pneumatic valves are key components in micro-reactors due to increasing artificial mixings. The principle and geometry of the pneumatic valve system developed by Caltech research group using multilayer soft lithography was adopted for fast and effective mixing purposes in spite of complicated operations and external power sources (Unger and Chou 2000). Micromixing processes have been

applied to microfluidic assays and dramatically improve performance by means of reducing measurement time and improving repeatability.

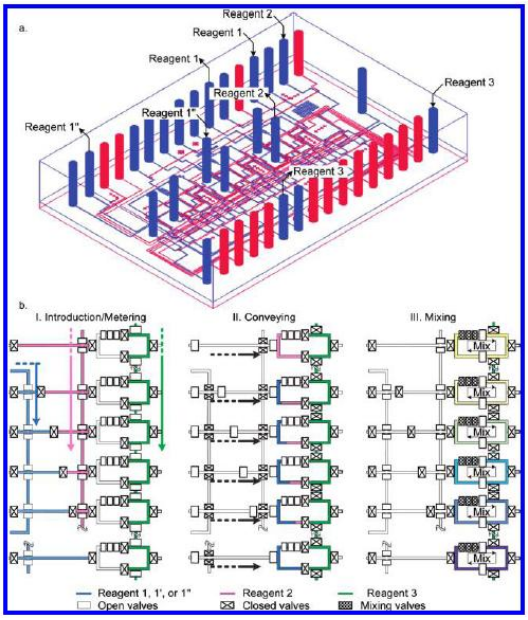

Figure 1.2 Enzyme kinetic reactor using micromixing valves (Yun et al. 2011)

Development of microfabrication technology permits integration of multi-component systems onto a single chip with full automation (Reyes et al. 2002). The performances of the integrated microfluidic devices show outstanding efficiency and are comparable to the classical chip. The first fully integrated microfluidic chip was initially used to increase the mixing of reactants, enzymatic reaction and separation (Jacobson et al. 1994). Advances continue to be made in this area and extend applications to biology such as DNA microarray processing.

Liu et al. (2006) carried out the fully integrated microfluidic device, consisting of microfluidic pumps/mixers, fluid channels, reagent chambers, and DNA microarray chips. On-chip washing, mixing and pumping in the single chip provide cost-effective

solutions because this chip does not suffer from intensive labor, sample loss and contamination, and inaccurate fluidic handling for DNA analysis. Fully automated microfluidic devices also provide ease of use, increased repeatability, and accurate performance by reducing human errors. An integrated analysis system has been called "micro total analysis system (μTAS)" or "lab-on-a-chip," but was not fully developed until the early 1990s. These two terms are now almost synonymous (Patrick Tabeling 2005). The positive feasibility of automation is promoted by developing remote control technology using microfluidic-based systems, making them attractive candidates for bedside diagnosis, environmental monitoring, drug discovery and bio-defense applications from inaccessible locations. Full automation by hundreds to thousands of integrated components in a single chip is becoming the new paradigm.

Melin and Quake (2007) invented a large-scale integrated microfluidic device for biological automation. This microfluidic device allowed performing hundreds or thousands of assays in parallel with multiple reagents. The fully automated microfluidic devices utilized synchronization and provided a simple operation compared to a non-parallel chip. There are more possible applications with the fully automated microfluidic devices. Protein crystallography, genetic analysis, amino acid analysis, high-throughput screening, bioreactors and single cell analysis need several components to control fluid handling and replace today's conventional methods (Hansen et al. 2006; Liu et al. 2003; Skelley et al. 2005; Thorsen 2003).

A Balagadde et al. (2005) invented the microfluidic bioreactor to enable long-term cell culture and monitoring of small populations of bacteria in a single chip. They controlled the cell density through a feedback mechanism by a synthetic circuit. They installed six

microchemostatics, which autonomously regulate the cell density based on quorum sensing. Figure 1.3a shows the actual image of a microfluidic bioreactor and Figure 1.3b is a schematic diagram of a microchemostat.

(a)

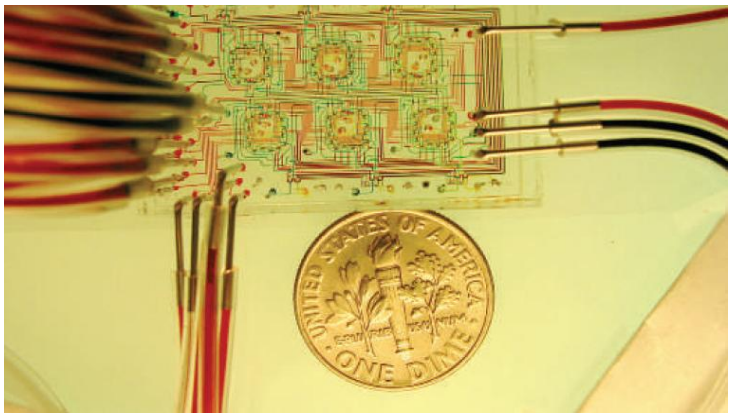

(b)

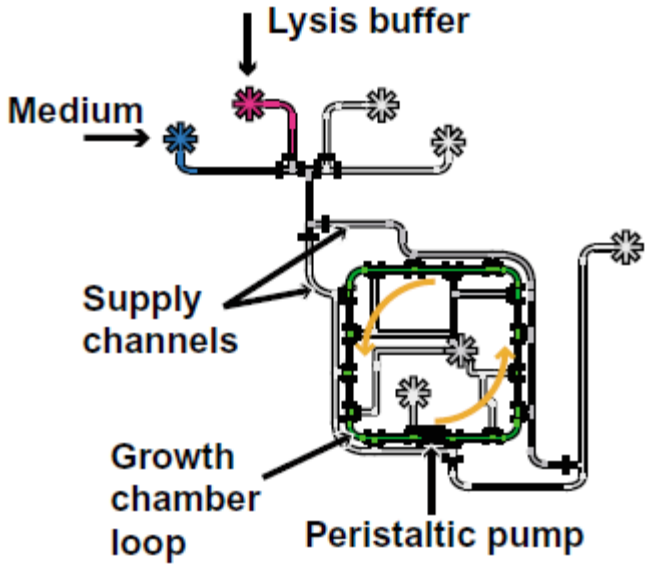

Figure 1.3 A multi-component microfluidic bioreactor **a** image of microfluidic bioreactor **b** schematic diagram of microchemostat (Balagadde et al. 2005)

1.3 Microfabrication technologies

The basic microfabrication techniques are not only applied to microfluidics devices but also to microelectronics using elastic PDMS materials. To fabricate micro-scale channels and structures, photolithography is one of the most significant core techniques. Lithography techniques can be catagorized by what types of energy beam are used. There are four categories: photolithography, electron lithography, X-ray lithography, and ion lithography (Thompson et al. 1994). The patterning process for photolithography makes use of a transparent glass plate, with metal (chromium) deposited on it. The accurate pattern is then transferred to the substrate by means of a photosensitive emulsion layer. For the general application in microfluidic devices, a plastic transparency film is one of the cost-effective options due to its high resolution and fast processing. Photolithography is composed of three steps (Nguyen and Wereley 2006):

- Positioning process: Deposition of photo-sensitive polymer resister using spin-coater uniformly covers a substrate. The distance between mask and substrate needs to adjust for the future process.
- Exposure process: The resister layer is exposed to a uniform beam such as optical or X-ray, transferring the film pattern to the photo-resist layer. This process is called the ‘transfer’ step of the pattern.
- Development process: Unwanted regions are eliminated by the developer solution. Two methods (Negative and positive photo-resist) are the most popular methods.

1.3.1 Fabrication of polymeric microdevices

There are three primary PDMS replication methods: molding, casting and microinjection (Patrick 2005).

- Molding: A polymer containing a catalyst is poured onto a patterned substrate and appropriately cured. The polymer is then peeled off the substrate and contains the pattern from the substrate.
- Casting: The mold is squeezed into a heated deformable material, followed by cooling and heating processes. A structure from this method represents the negative of the mold.
- Microinjection: Liquid state plastic material is directly injected into a mold. After the separation process, the negative photo-resist mold is achieved.

PDMS is from a family of polymers with the formula $(-Si(CH_3)_2O)-$ as shown in Fig. 1.4a. The PDMS polymer becomes an elastomer when the temperature and the reagent put into the PDMS mixing solution are beyond polymerization condition as shown in Fig. 1.4b. Soft lithography of PDMS consists of three steps: fabrication of the mold, pouring PDMS into the mold and peeling off the PDMS. The fabricated structures provide surprisingly sub-micrometric precision when the dimensions of microchannels lie between 5 and 50μm (Kim et al.1995). The main mold materials used are silicon wafers, electrodeposited metal and SU-8 polymers. Therefore, understanding of the microfabrication methods for silicon or glass is very important along with PDMS fabrication.

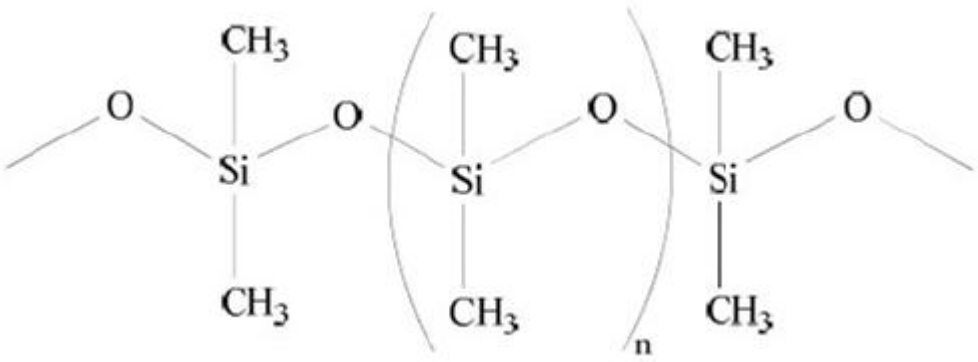

(a)

$$-O(CH_3)Si-CH=CH_2+H-Si(CH_3)O-\xrightarrow{\Delta}-O(CH_3)Si-(CH_2)_2-Si(CH_3)O-$$

(b)

Figure 1.4 A dominant molding based on PDMS (polydimethylsiloxane) **a** chemical structure of polydimethylsiloxane (PDMS) **b** covalent bonding curing process (Campbell et al. 1999)

1.3.2 Fabrication of silicon and glass microdevices

Single crystal silicon provides the following advantages (Tabeling 2005):

- Well known materials and well-established microfabrication processes, providing well documented properties.
- Very accurate fabrication of devices (less than submicrometric precision).
- Compatible with electronic circuits.
- Physical and chemical characteristics incorporate a large number of processes.

There are two different types of etching techniques for silicon. Wet etching is the etching process of a solid material with chemical solutions. During this process, the UV exposed substrate is either dipped into the solution or the chemical solution is sprayed onto the UV exposed substrate. In most cases, wet etching techniques provide isotropic structures, which are independent of crystalline orientation. The mixture of

$HF/HNO_3/CH_3COOH$ is a general example of isotropic etching. The major advantages of these processes are:

- High selectivity
- High repeatability
- Relative planar etching surface

However, isotropic etching has a significant limitation in the fabrication of lateral structures. Isotropic wet etching now focuses on removing thin layers or thin films from the substrate.

Dry etching can be categorized into physical dry etching and chemical dry etching. The main advantages are:

- Depending on the etching conditions, anisotropic or isotropic shapes of structures can be obtained.
- Diversity and refinement of engineered structures.

Physical dry etching makes use of ion, electron or photon beams to attack the target substrate. The kinetic energy of ions initially forcefully breaks atoms from the silicon surface, and then the high energy beam begins to evaporate unwanted materials. Even though many silicon etching techniques are used to apply this method because of its accuracy, this technique is faced with several drawbacks, such as slow etching rate, low selectivity and trench effect by reflected ions. Chemical dry etching makes use of chemical reactions between etchant gases to attack the silicon surface. The created structures are usually isotropic, similar to the wet etching technique. This method provides high selectivity because the etchant gas can react directly with the etched material (Nguyen and Wereley 2006).

1.4 PDMS material properties

Polydimethylsiloxane (PDMS) is a commercially successful silicon rubber due to its physical and chemical stability. The rubber elastic properties of PDMS have become versatile tools for microfluidic devices and have been used in micro flow cytometry, peristaltic pumping and mixing, and a novel pressure sensor (Tung et al. 2004; Wang et al. 2011; Wang et al. 2009). Highly flexible PDMS microfluidic channels also were used to maintain chemostatic conditions for bacterial and yeast colony growth (Groisman et al. 2005). Several researchers have examined their elastic properties (Clarson and Semlyen 1993; Van Krevelen and Hoftyzer 1976) and found:

- A low glass transition temperature (Tg≒-125°C)
- A unique flexibility (The shear modulus G varies between 100kPa and 3MPa)
- Very low loss tangent (tanδ « 0.001)
- Small temperature variations of the physical constants
- High dielectric strength (~14 V μm^{-1})
- Compatibility over a wide temperature range (-100°C up to +100°C)
- Low chemical reactivity (except at extremes of pH)

Lötters et al. (1997) investigated the PDMS shear modulus as a function of temperature and frequency. They found that the shear modulus did not depend on the applied frequency but the applied temperature. They also investigated adhesion strengths of cured PDMS to polished tungsten and report an adhesive strength up to 180kPa. Liu et al. (2009) investigated the relation between the mechanical strength and the Young's modulus of thin PDMS membrane. The Young's modulus of PDMS membranes

significantly increased when the thickness of PDMS decreased. The Young's modulus ranged from 600kPa (1.8mm thickness) to 1400kPa (50μm thickness). Hocheng et al. (2010) examined the relation between the density and Young's modulus of PDMS under various conditions. They found that there was a linear relationship between the density and mixing ratio of PDMS. In addition, the Young's modulus of PDMS was strongly dependent on the amount of the curing agent. The larger the amount of the curing agent, the larger the value of Young's modulus has.

1.5 Advantages of PDMS material

Early microfluidic devices made of hard materials such as glass and silicon had been fabricated with MEMS (microelectromechanical systems) technology. Since George Whitesides' group at Harvard University introduced PDMS (polydiemthyl siloxane) based microfluidic devices, this material has been widely used in the fabrication of complex patterned microfludic devices. The benefits of PDMS are numerous, such as:

- Replica molding of micro-sized microfluidic channel shapes
- Implementation of quick and inexpensive applications
- Flexible materials with high strength
- Optical transparency (240nm to 1100nm) for microscopy.
- Good gas permeability in low pressure
- Excellent applications to aqueous media
- Variety of mechanical properties: Young's modulus usually depends on mixing ratio between PDMS/curing agent and provides different mechanical properties based on experimental purposes

- Easy peeling from substrates

However, undesirable properties of PDMS also exist, such as:

- Evaporation of water vapor due to high permeability
- Strong hydrophobic surface
- Very strong C-H chemical bonding
- Swelling of PDMS due to organic solvents

Effective remedies are currently being studied to compensate for the shortcomings. For instance, oxygen plasma or immersion in a strong base solution modifies the surface properties from a strong hydrophobic to a hydrophilic surface. Also, PDMS microfluidic channels treated with oxygen plasma provide strong adhesion to glass, silicon, or polyethylene. As a result, a PDMS material is becoming a common material in microfluidic devices. PDMS microfluidics devices have expanded their applications to several fields of industry because of the advantages. One of them is outstanding economic cost, and another is the simplicity of microfabrication. The material cost of PDMS is relatively cheap, and simple PDMS device fabrication does not require prior microfabrication experience. Once the silicon wafer is fabricated in a clean room, there are no special instruments needed and the remaining job can be accomplished in a standard laboratory. In contrast to the PDMS replica process, materials like glass and silicon require the following complicated processes: wet chemical etching, dry etching using reactive ion etching (RIE) and thermal bonding. These techniques require a lot of time from researchers and expert knowledge about the necessary instruments. As a result, PDMS has become a superior candidate for a wide variety of commercial manufacturers.

In addition, the fabrication of disposable microdevices using glass and silicon requires expensive material price, time and effort compared to PDMS material.

The next important advantage is the integration of several components in a single chip, which was mentioned previously. The integration process requires two-layer alignment without additional complicated processes. Some of the components such as valves, reactors and pumps need significant power sources to control fluids through micro-devices. In spite of this drawback, one of the huge advantages is that micro-valves are independent of fluid properties. PDMS micro-valves also have small dead volumes, resulting in fast response times in fluid reactions. Furthermore, PDMS micro-valves have excellent durability compared to glass and silicon materials, because PDMS is relatively free from wear or fatigue.

Another advantage is that PDMS material allows simple connections with tubing, providing tremendous benefits compared to rigid material devices. Plastic microbore tubing is usually inserted into the punched holes using a microprobe. The delivered pressure from other instruments using connected microbore tubing can accommodate up to several atmospheres.

1.6 Classical fluid mechanics for microfluidic system design

Based on experimental setup, liquid motion in micro/nanofluidic devices can be controlled in several ways. Some systems use a hydrostatic system or a pressure generator to control the flow rates using pressure difference, whereas many users use a syringe pump to impose a constant flow rate. In addition, an electro-osmotic pump also can be used to generate a liquid flow through a microfluidics device. Figure 1.5

introduces several types of commercial external liquid flow systems, such as hydrostatic pressure, pressure generator, syringe pump and electro-osmotic pump. One of the simplest ways to control the liquid flow in a microfluidic device is using hydrostatic pressure. Pressure generators consist of three main parts: a pressure source (e.g. compressor, bolt), a pressure regulator using a membrane and a pressure monitoring device such as a manometer. The accuracy is strongly dependent on the compatibility of the three components. One of the major drawbacks is the deformation of the membrane, which prevents fast response times. Electronic pressure generators with two valves can generate unwanted fluctuation of pressure. The origin of the syringe pump system was initially established in the field of medicine using a perfusion system. The approach has extended its application to become a key part of microfluidic devices. The syringe pump is a general tool in microfluidic devices because of its capability to provide a constant flow rate regardless of the fluid resistance. However, a flow with regular periodic variations known as a pulsatile flow can occur at low flow rates. Thus, a time requirement for stabilization of the flow is mandatory. The problem of flow fluctuation in the case of a syringe pump system is mitigated by the electro-osmotic pump system. The electrical energy is able to deliver the liquid through porous materials which tend to eliminate fluctuations. However, this technique can generate large unwanted back pressures.

(a)

(b)

(c)

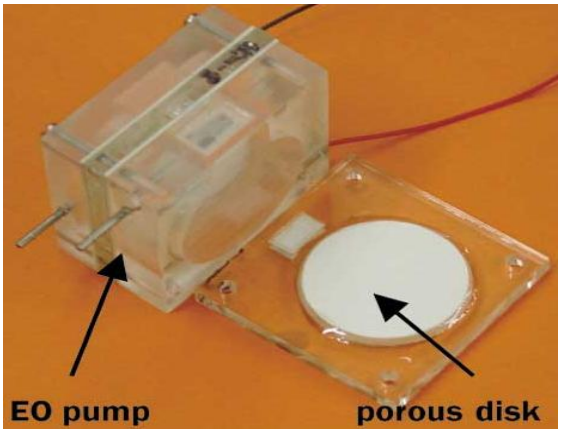

Figure 1.5 a Pressure generator for microfluidic chip **b** syringe pump system **c** electro-osmotic pump (http://www.mictonit.com)

Microfluidics devices are characterized by the shrinking of the dimension from macro-scale to roughly 100nm to 100μm. The small scale provides many advantages in the microelectronics and microchannel devices as described in the previous section. At the nanoscales, the governing physical laws can change rapidly compared to classical

scale. In general, the Reynolds number in microfluidic systems is low (not exceed 10^{-1}) and the flow is laminar. In contrast, high Peclet numbers (Pe) leading to mass transfer is often observed in microfluidic mixing system. A classical fluid theory has been applied to microfluidic system and showed a good agreement in most cases. Brief reviews in regard to some physical properties of fluids at micro-scale are described in this chapter. The behaviors of incompressible fluids are governed by the Navier-Stokes equation where for Newtonian fluids for constant density (ρ) and viscosity (μ) (Geankoplis 1993):

$$\rho\left(\frac{\partial v_x}{\partial t} + v_x \frac{\partial v_x}{\partial x} + v_y \frac{\partial v_y}{\partial y} + v_z \frac{\partial v_x}{\partial z}\right) = \mu\left(\frac{\partial^2 v_x}{\partial x^2} + \frac{\partial^2 v_x}{\partial y^2} + \frac{\partial^2 v_x}{\partial z^2}\right) - \frac{\partial p}{\partial x} + \rho g_x \qquad (1.1)$$

$$\rho\left(\frac{\partial v_y}{\partial t} + v_x \frac{\partial v_y}{\partial x} + v_y \frac{\partial v_y}{\partial y} + v_z \frac{\partial v_y}{\partial z}\right) = \mu\left(\frac{\partial^2 v_y}{\partial x^2} + \frac{\partial^2 v_y}{\partial y^2} + \frac{\partial^2 v_y}{\partial z^2}\right) - \frac{\partial p}{\partial y} + \rho g_y \qquad (1.2)$$

$$\rho\left(\frac{\partial v_z}{\partial t} + v_x \frac{\partial v_z}{\partial x} + v_y \frac{\partial v_y}{\partial y} + v_z \frac{\partial v_z}{\partial z}\right) = \mu\left(\frac{\partial^2 v_z}{\partial x^2} + \frac{\partial^2 v_z}{\partial y^2} + \frac{\partial^2 v_z}{\partial z^2}\right) - \frac{\partial p}{\partial y} + \rho g_z \qquad (1.3)$$

This can be more succinctly written as:

$$\rho \frac{\overline{\partial v}}{\partial t} = -\nabla \bar{p} + \mu \nabla^2 \bar{v} + \rho \bar{g} \qquad (1.4)$$

Where v is the fluid velocity, g is the gravity, p is the pressure and f represents other body forces exerted on the bulk of the fluid elements. This equation is generally simplified in micro and nanofluidic system under the following assumptions.

- Material is assumed to be a Newtonian fluid
- The flow is assumed to be an axial flow
- Flow is in a steady state condition
- No external body forces exist

Using these conditions, Eq. (1.4) can be simplified to:

$$0 = = -\nabla p + \mu \nabla^2 v \tag{1.5}$$

This equation can then be applied to solve the case of cylindrical microfluidic channels. In the case of cylindrical microfluidic channels, the relationship between flow rates and pressure drops is represented by the Hagen-Poiseuille equation.

$$\nabla p = \mu \nabla^2 v = \frac{8 \mu L Q}{\pi r^4} \tag{1.6}$$

If the flow moves through a circular microfluidic channel of radius R with a no-slip boundary condition, the solution from the previous equation is (Bird et al.2002):

$$U(r) = \frac{-\nabla p}{4 \pi L} (R^2 - r^2) \tag{1.7}$$

This is a fully-developed parabolic velocity profile.

The Reynolds number is a dimensionless number and is defined as the ratio between inertial forces and viscous forces. Thus

$$Re = \frac{D v \rho}{\mu} \tag{1.8}$$

A low Reynolds number means that viscous forces dominate over inertial forces and the flow is laminar. Liquid/gas flows through microfluidic channels are smooth-mannered and exhibit no turbulence. Under this condition, inertial terms can be neglected because the ratio of inertial terms to viscous force terms becomes very small.

For steady-state incompressible flows, Eq. (1.4) reduces to Bernoulli's equation (Streeter and Wyle 1975)

$$p_1 + \rho g h_1 + \rho \frac{v_1^2}{2} = p_2 + \rho g h_2 + \rho \frac{v_2^2}{2} \tag{1.9}$$

Along a microfluidic chip without significant differences in elevation, $h_1 = h_2$ and Eq. (1.9) can be rearranged as

$$p_1 + \rho \frac{v_1^2}{2} = p_2 + \rho \frac{v_2^2}{2} \tag{1.10}$$

CHAPTER 2

LITERATURE REVIEW

One of the main goals of this chapter is to introduce current research trends and scientific issues in regards to flow properties using micro-scale channels. A lot of studies have reported experimental data and concluded that classical theory showed either good agreements or large discrepancies from the data. Since the use of microchannel flow became general in a number of industrial applications, the rapid growth of debates has been fueled by finding significant deviations of actual experiment results from predicted values. The essentials of traditional and modern fluid mechanics theories are widely applied to macro and microfluidics devices. However, friction factor (f) discrepancies from predicted values have been disputed for a long time. As a result, the fundamental flow behavior in microchannels remains the subject of worldwide experimental and theoretical investigation. The continuum assumption and usage of the Navier-Stokes equations are generally assumed valid for liquid flow in microchannels with hydraulic diameters greater than 1μm (Steinke and Kandlikar, 2006).

2.1 Viscous friction effects in microfluidic flow

In many published papers, the authors have reported flow parameters such as pressure drop, Poiseuille number, flow velocity, Reynolds number and friction factor. Due to ease of microfabrication, rectangular cross-section microchannels are widely used

compared to other microchannel cross sections. The channel aspect ratio (α) is usually defined as $\alpha = \frac{H}{W}$ where H is the channel height, and W is the channel width. The deep microchannels have relatively high values of the aspect ratio. It is obvious that deep microchannels have large heat transfer areas compared to more shallow microchannels, so heat transfer performance is better.

Peng et al. (1994) characterized water flowing through rectangular microchannels, with hydraulic diameters of 0.133-0.367mm and H/W ratios of 0.333-1. They found that decreasing α in rectangular microchannels increased the friction factor significantly. The frictional behaviors exhibited large deviations from classical predictions, and the friction factor, *f*, was proportional to $Re^{-1.98}$. The slope of the friction factor plotted versus the Reynolds number was thus much steeper than expected (i.e., *f*= 1/Re) as shown in Fig 2.1. In addition, Peng et al. (1994) claimed that these odd relations were due to the low aspect ratio.

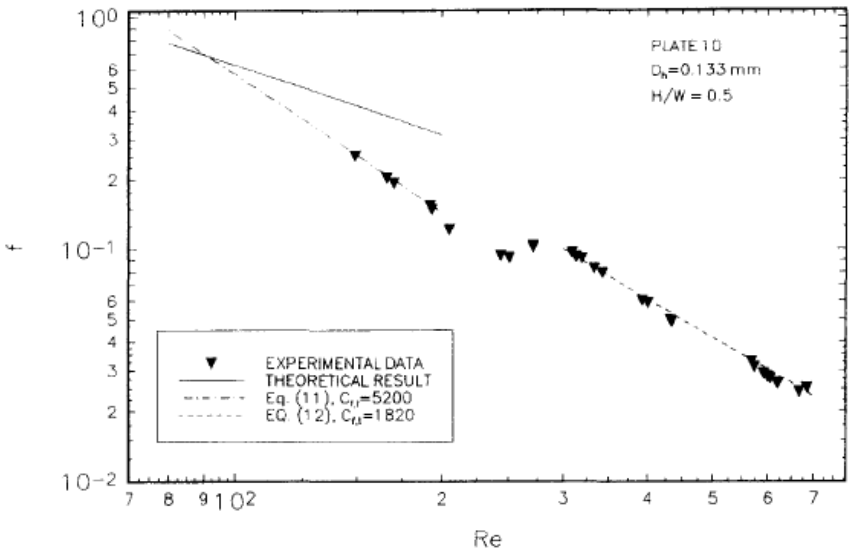

Figure 2.1 Analysis of experimental and theoretical friction factors in plate (Peng et al. 1994)

Papautsky et al. (1999) also investigated the effect of rectangular microchannel aspect ratio on laminar flow. They investigated the behavior of liquid flows with surface micromachined rectangular metallic pipette arrays. The geometry of each array, consisting of 5 or 7 pipettes, was that channel widths varied from 150μm to 6000μm and channel heights ranging from 22.71μm to 26.35μm. The Reynolds numbers investigated were less than 10 and the experimental data are shown in Fig 2.2. An approximate 20% increase in the friction constant was observed at low aspect ratios. Similarly, an increasing friction factor was also observed in experimental data when the Reynolds numbers were less than 100.

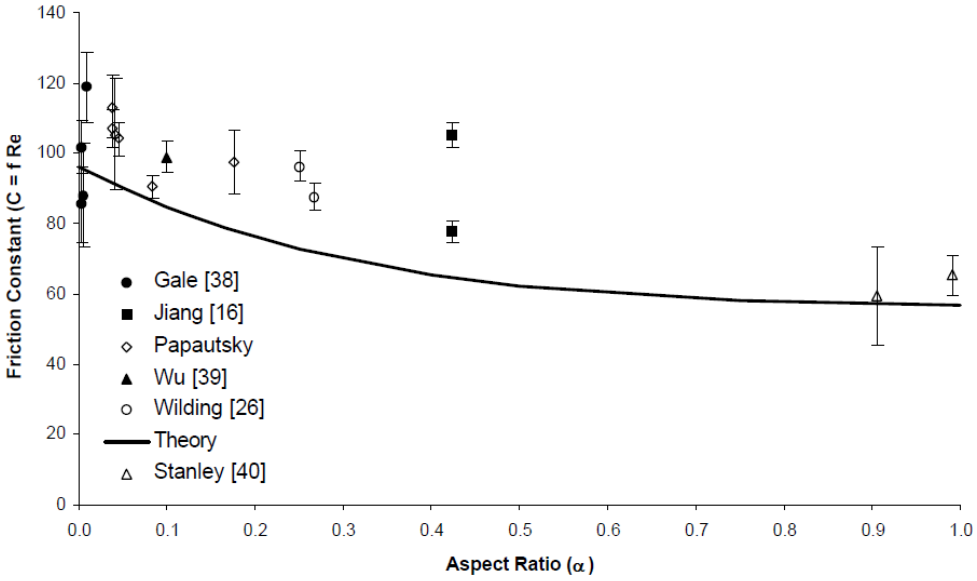

Figure 2.2 Experimental friction data as a function of aspect ratio (Papautsky et al. 1999)

Steinke and Kandlikar (2006) analyzed single-phase liquid friction factors in microchannels and expressed their results in terms of the Poiseuille number (*fRe*). The C* ratio (i.e., normalized friction coefficient) is the ratio between the experimental value of *fRe* to the theoretical value of *fRe*. Thus

$$C^* = \frac{(f\ \mathrm{Re})_{experiment}}{(f\ \mathrm{Re})_{theory}} \tag{2.1}$$

Steinke and Kandlikar claimed that a great deal of discrepancy between the experimental and the predicted values was because of several reasons. One of reason was due to the entrance and exit losses. After accounting for the entrance and exit losses, the friction factor showed better agreement with the predicted values. The second reason was the experimental uncertainties. Many published papers and Steinke and Kandlikar reviewed the C* ratio was between 0.6< C*<1.6 as shown in Fig 2.3. Generally, higher values of uncertainty were observed at higher Reynolds numbers. The last reason was due to inadequate characterization of the specific dimensions of the fabricated microchannels.

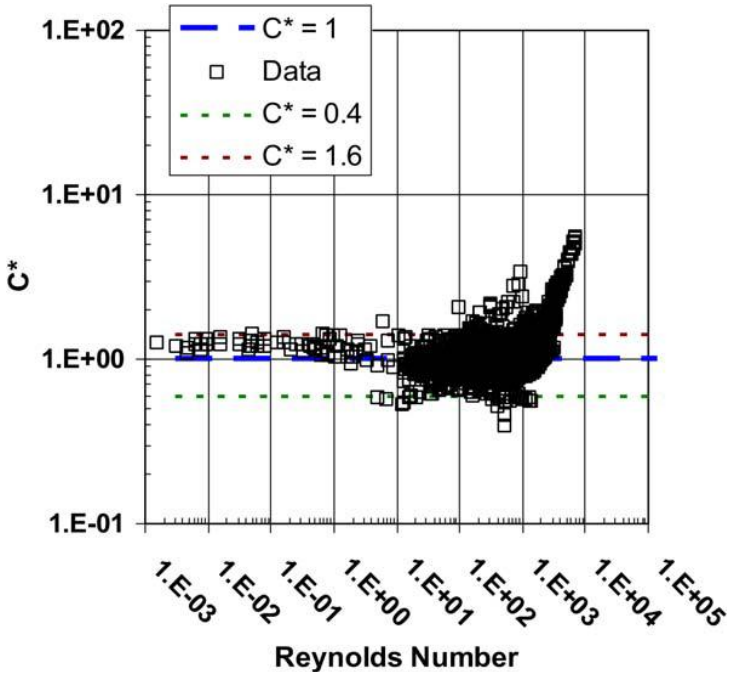

Figure 2.3 Analysis of literature studies with respect to the Poiseuille number and Reynolds number (Steinke and Kandlikar 2006)

Sharma et al. (2006) reported the deviation of the normalized friction coefficient from the predicted values using air as the fluid. The dimensions of three microfabricated silicon channels were 3000μm x 360 μm, 1500μm x 180 μm, and 750μm x 90 μm with depth 360 μm. The investigated C* ratios ranged from 1.45 to 2.85. Experimental deviations were observed for Reynolds number in the range of 100-1000.

Hsieh et al. (2004) studied incompressible liquid flow in rectangular microchannels. The dimension of microchannels investigated was 115μm deep, 200μm wide and 24mm long with hydraulic diameter of 146μm.The pressure drop and flow rates were measured and friction factors were calculated for different Reynolds numbers. At low Reynolds numbers, the friction factor was almost constant and was slightly larger than the conventional theory. The friction factor was influenced by the Reynolds number and the hydraulic diameter under the high Reynolds number regime. In addition, pressure drop along the microchannel showed linear behavior at Re> 200, while a nonlinear trend was observed if Re<200.

Jung and Kwak (2008) measured the friction factor for flow of water through rectangular cross-section microchannels. The obtained friction factors from the 100μm width channels were between 53.7 and 60.4, which were close to the theoretical value of 56.9. However, the channel width change from 100μm to 200μm indicated the measured values of the friction factors were 25% higher than expected from theory (f=62.2/Re). Figure 2.4 shows that the friction factors as a function of the Reynolds number are dependent on channel width with the same depth of 100μm and the same length of 15mm.

Experimental investigations have been performed on various cross- sectional shapes of microchannels to analyze flow properties. Yang et al. (2003) reported the friction factor of air, water and liquid refrigerant R-134a through circular tubes, ranging from 0.173 to 4.01mm in diameter. The laminar-turbulent transition Reynolds number increased with decreasing circular tube diameters. They claimed that the friction factors showed a good agreement for water and refrigerant R-134a (f=0.079Re$^{-0.25}$).

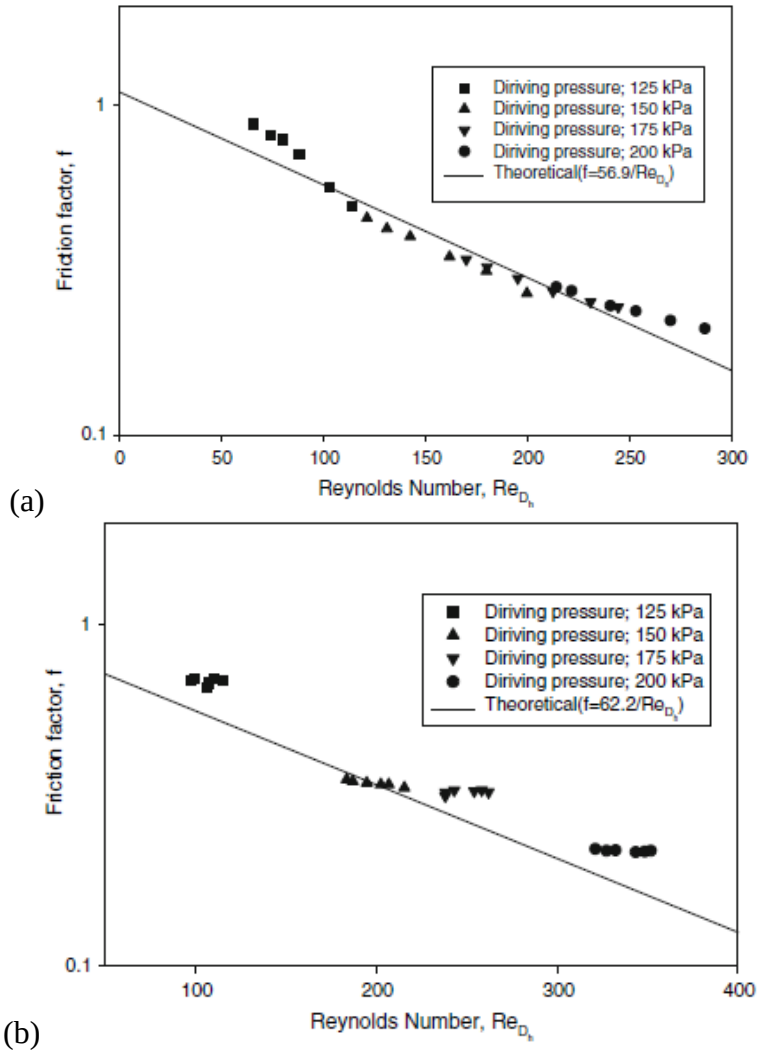

Figure 2.4 a Friction factors as a function of the Reynolds number for 100μm channel width **b** Friction factors as a function of the Reynolds number for 200μm channel width (Jung and Kwak 2008)

Khan et al. (2011) also performed a similar study using circular microchannels. The microchannels had a hydraulic diameter of 279μm and a length of 45mm. The microchannels were made of stainless steel and deionized water was used in the study. Seventy nine microchannels were arranged in circumferential manner, and the measured Reynolds numbers ranged from 300 to 3000. The experimental result showed good agreement with the classical correlations of friction factor as well as the proposed equation, as shown in Fig 2.5. The researchers also found that channel length and diameter were key factors to heat dissipation.

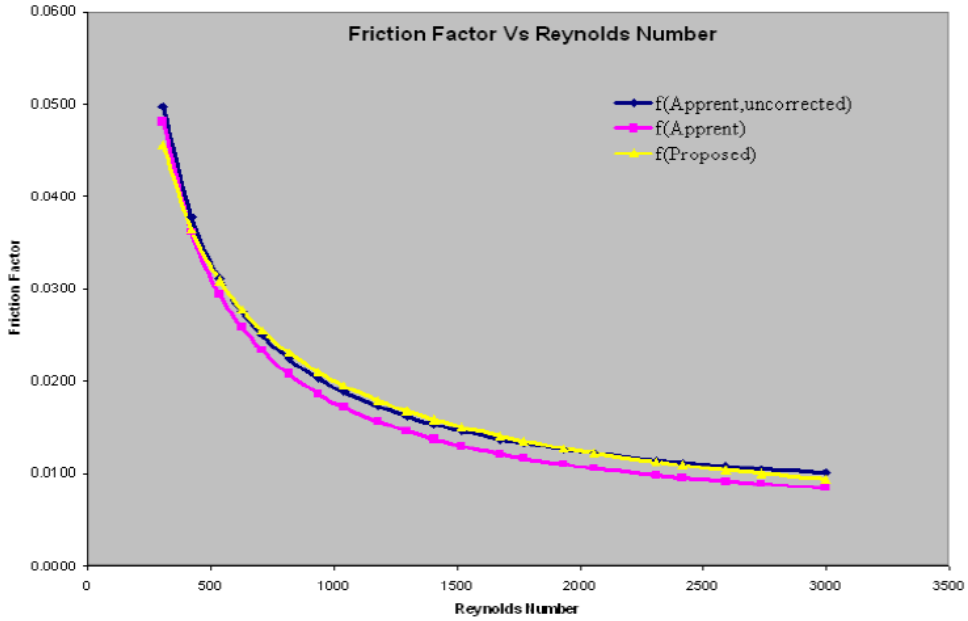

Figure 2.5 Comparative plot of experimentally determined friction factor with the proposed equation (Khan et al. 2011)

However, Mala and Li (1999) investigated water flow through circular microtubes from 50μm to 254μm in diameter. Microtubes were made of fused silica (FS) and stainless steel (SS). Flow characteristics such as pressure drop and flow rates were measured and then compared with the predicted values using conventional theory. A significant

deviation of flow characteristics was observed with the smaller diameter tubes, whereas there was rough agreement with the conventional theory with the larger diameter tubes. Small diameter microchannels generated large deviations from predicted values by a significant increase in pressure gradient. The friction constant ratio, C*, was always greater than 1 in this study due to surface roughness of the tubes. The fused silica microtubes observed a higher pressure gradient than the stainless steel microtubes due to their rough surfaces.

Peiyi and Little (1983) conducted the first study of microscale fluid flow through trapezoidal cross-sectional area and measured Darcy friction factors for both laminar and turbulent gas flow. The hydraulic diameters they used ranged from 50μm to 80μm. They observed that experimentally measured Darcy friction factors were around 22% larger than classical theory.

Wu and Cheng et al. (2003) reported the friction factor of laminar flow using deionized water in smooth silicon microchannels. The trapezoidal cross-section had a hydraulic diameters in the range of 25.9~291.0μm. They found that the friction factor was strongly dependent on the cross-sectional aspect ratio. Their experimental data agreed with an existing analytical solution for an incompressible, fully developed, laminar flow under no slip boundary condition. Figure 2.6 shows the comparison of experimental data and analytical solution.

Qu et al. (2000) investigated flow behavior of water through trapezoidal silicon microchannels. They used hydraulic diameters ranging from 51μm to 169μm. The pressure drop and flow velocity across microchannels were measured and compared with the conventional laminar flow theories. Qu et al. (2000) also claimed that the pressure

gradient and friction in microchannels were higher than the predicted values due to surface roughness. The C* ratio was 8-38% higher than the theoretical prediction in the range of Reynolds numbers investigated.

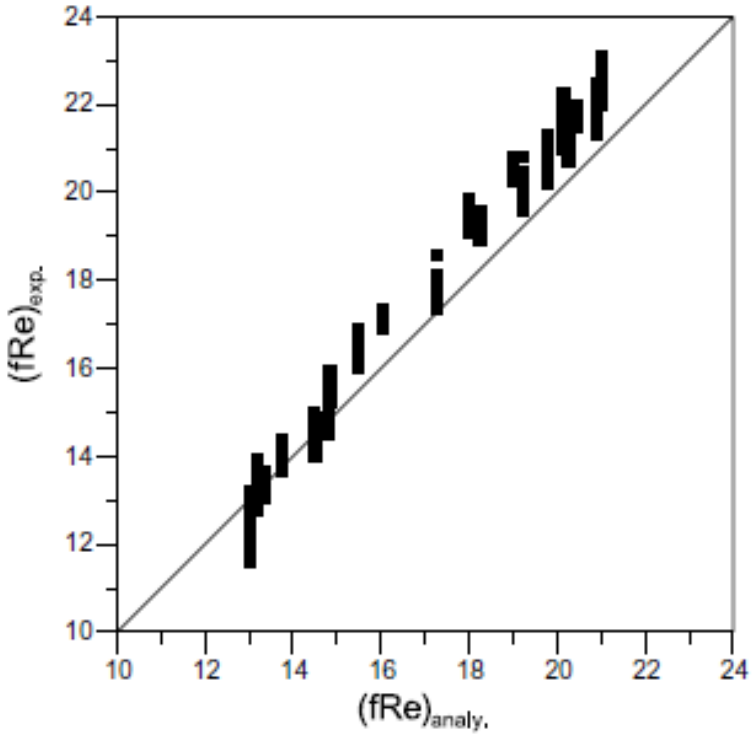

Figure 2.6 Comparison of experimental data and analytical solution (Wu and Cheng et al. 2003)

2.2 Applications of embedded obstacles in microchannels

2.2.1 Improved mixing of fluids

Effective micromixing is a very important application in bio and chemical analysis using micro TAS (total analysis systems) or lab-on-chips (Suh and Kang 2010) because of the nature of low Reynolds number flow. There are two types of mixing utilized in microfluidic systems. Active micromixers provide very effective mixing. However, such approaches are more use an external power sources. In contrast to active micromixer,

passive micromixers require no external power sources and primarily depend on the geometry of sidewalls or proper layout of embedded obstacles to obtain fluid mixing. Figure 2.7 introduces several micromixer designs for inducing artificial chaotic advection at the low and intermediate Reynolds numbers (Nguyen and Wu 2005).

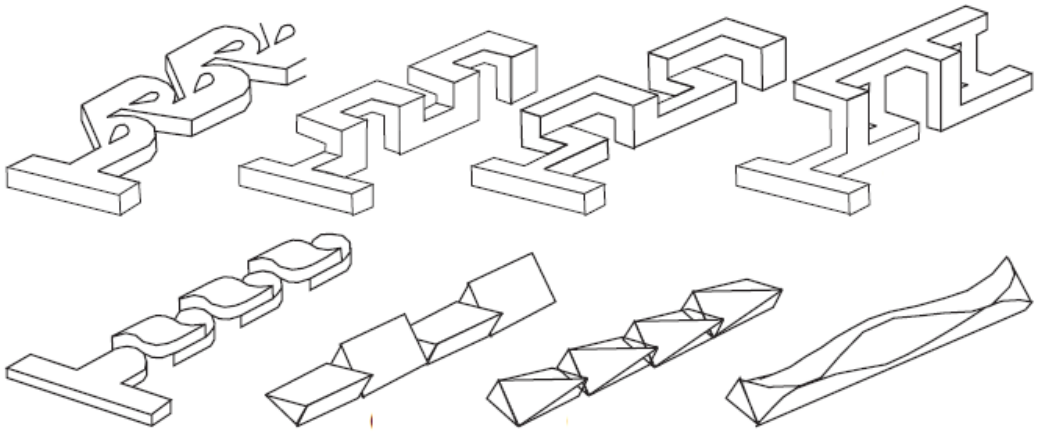

Fig 2.7 Various micromixer designs for mixing with chaotic advection (Nguyen and Wu 2005)

Bhagat et al. (2007) investigated a planar passive microfluidic mixer, which operated at the low Reynolds number. The micromixer they used maintained low pressure drops by using arrays of obstacles. Some of their passive mixing schemes are shown in Fig 2.8. Different shapes of obstructions and different arrangements of obstructions inside microchannels proved to be beneficial for enhancing mixing. They confirmed that the best mixing was observed when the circular obstructions were arranged with 1x1 repetitive patterns across the channel center. However, they found that mixing enhancement gradually decreased as the number of repetitions was increased.

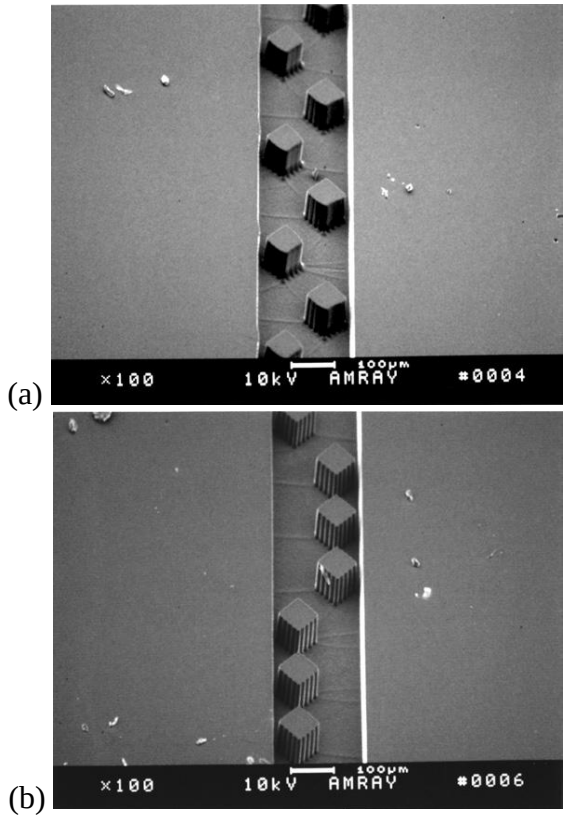

Figure 2.8 Micro-mixer in PDMS with obstructions **a** 1x1 **b** 3x3 configuration (Bhagat et al. 2007)

Tseng et al. (2011) theoretically investigated the mixing geometries of Bhagat et al. (2007) using CFD simulation. The predicted mixing index and Reynolds number from numerical simulation showed good agreement with the previous experimental results. Obstacles protruding from channel boundaries were observed to improve mixing because of diffusion-enhanced or convection-enhanced mixing. To obtain optimal passive micromixers, geometric design parameters, such as shape, length, width and location of boundary protrusion structures, must be carefully considered.

Jain et al. (2009) studied efficient mixing techniques at low Reynolds numbers. They dealt with optimization of the geometric shape of flow obstacles and the effects of

inducing vortices in the vicinity of the embedded obstacles. Jain et al. (2009) found that the triangle-shaped obstacles provided ideal mixing in the diffusion dominant region. The optimal design provided strong local flow vortices as well as maximum backflows due to their non-symmetric shapes.

Keoschkerjan et al. (2004) fabricated very dedicated micro-reactor systems, combining multi-lamination and chaotic advection effects. The mixing was effectively performed on overlapping micro-restrictions, which created micro-cavities in the two wafer levels. A continuous three-dimensional channel was made by good arrangement of cavities. The flow was forced to follow a tortuous route including many changes in the flow direction. Kim et al. (2004) investigated pressure-driven flow through a barrier embedded micromixer. The schematic of chaotic mixing mechanism induced chaotic flow created by periodic perturbations. The micromixer contained barriers along the upper surface and the lower surface of the channel. Periodically inserted barriers were located in the upper surface, while slant grooves were designed for inducing helical type flow on the lower surface. A confocal microscope was used to measure cross-sectional mixing behaviors in various positions as shown in Fig 2.9. The corresponding Reynolds number was very low, but the experimental results confirmed that the barrier deposited micromixer realized outstanding mixing efficiency within a short length of channel. Chen and Cho (2008) reported fluid injection through channel inlets, applying periodic velocity perturbations to the flows. In an attempt to increase the mixing efficiency, they designed a wavy-wall section as shown in Fig 2.10, which enabled isolation of sample flow. The repeated processes gave rise to “stretching-folding” behavior and eventually increased the mixing

efficiency. They claimed that the mixing performance was increased by increasing geometric wave amplitude or length of the wavy-wall section.

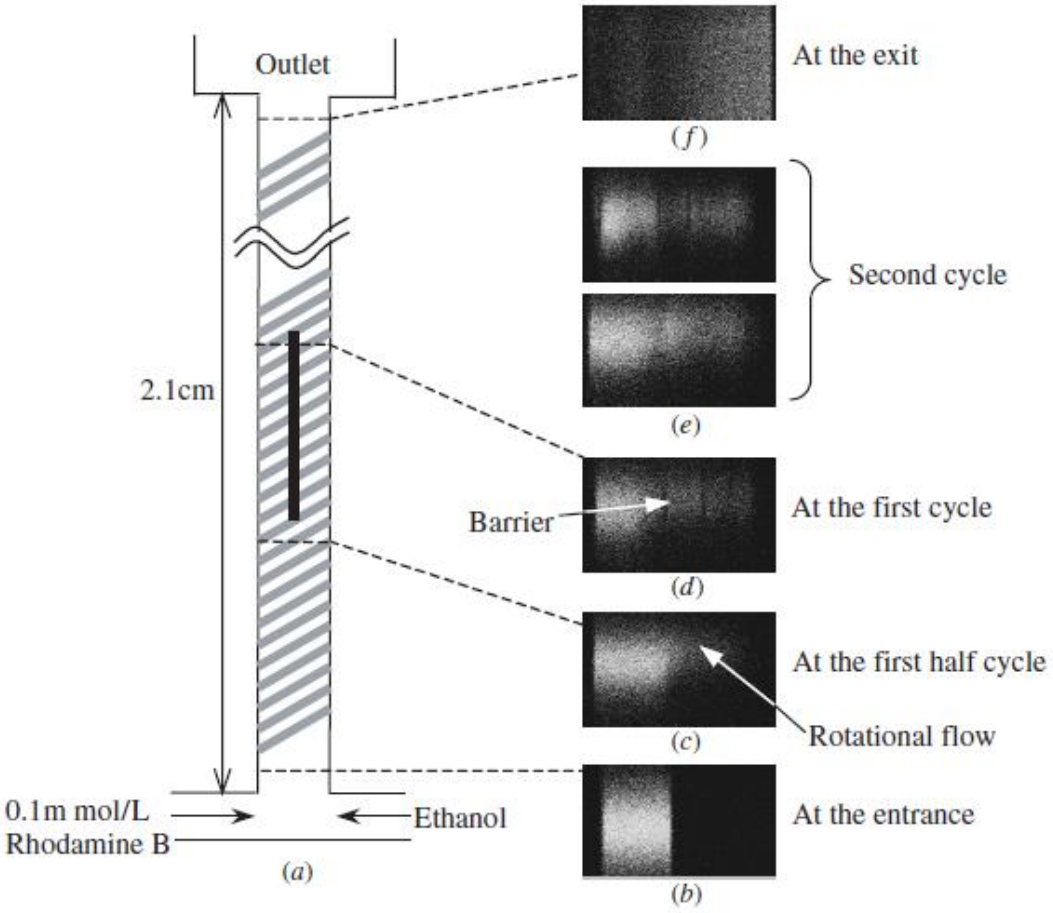

Figure 2.9 Cross-sectional confocal microscopy images at several positions **a** schematic micromixer design **b** mixing behavior at the entrance zone **c** no-barrier zone at the first half cycle **d** barrier zone at the first half cycle **e** barrier and no-barrier zone at the second cycle **f** at the exit zone (Kim et al. 2004)

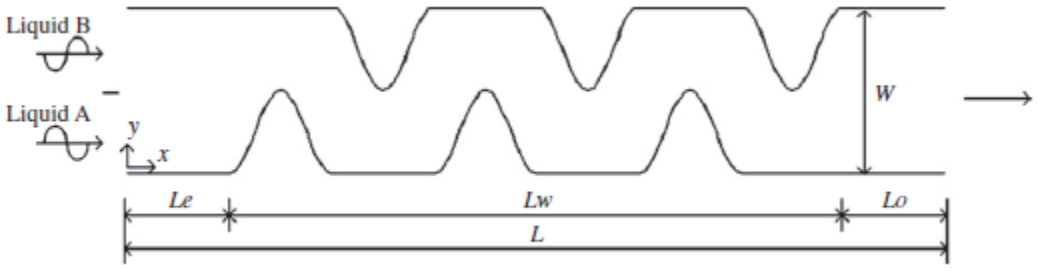

Figure 2.10 Schematic illustration of a microchannel with wave-wall section Chen and Cho (2008)

2.2.2 Enhanced reactions and heat transfer

Micropost arrays in microchannels have been widely used as components within micro-reactor, micro heat exchangers and micro-total analysis systems (μTAS). The functional microposts for enhancing heat transfer, adsorption/desorption and surface chemical reactions are caused by increasing surface area to volume ratio. Therefore, the optimum design of microposts provides a key parameter for μTAS devices. The surface area to volume ratio goes up when the geometry of the device becomes small. The downside is the increase the pressure drop across microchannels filled with microposts. Yeom et al. (2009) investigated the micropost-filled gas chromatography system to optimize the performance as shown in Fig 2.11. The key factor of its design was to maximize the surface area to volume ratio for microchannel geometry, while the flow resistance was to be minimized across the micropost-filled channels under low Reynolds number flows. They developed the flow resistance models which were strongly dependent on design parameters such as blockage ratio (the ratio of the radius of each post to the half-spacing between two adjacent posts). They also demonstrated that the drag per circular cylinder was proportional to the upstream velocity and the viscosity of fluid.

Mohammed et al. (2011) investigated triangular shaped microchannel heat sinks for the impact of different types of microposts and flow behaviors. They examined the performance on aluminum microchannel heat sinks. A variety of nanofluid coolants such as Al_2O_3, Ag, CuO, diamond, SiO_2, and TiO_2 were coordinated with the base fluid, water. The combination of diamond and water fluid provided the lowest temperature along with the highest heat transfer coefficient, while the combination of Al_2O_3 and water provided

the highest temperature along with the lowest heat transfer coefficient. In addition, the combination of SiO_2 and water fluid provided the highest pressure drop and wall shear stress, while the combination of Ag and water provided the lowest pressure drop and wall shear stress. Mohammed et al. (2011) claimed that the combination of both diamond and water and Ag and water was utilized to enhance heat transfer along with low pressure drops.

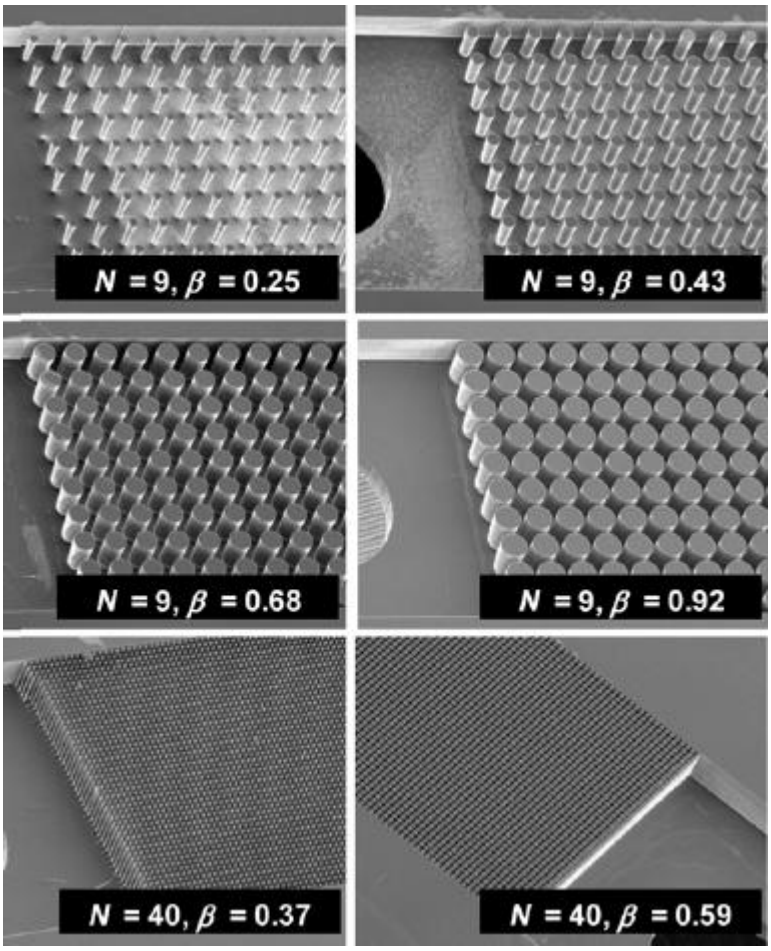

Figure 2.11 Actual SEM images with various arrangements of circular arrays (Yeom et al. 2009)

2.2.3 Bacteria motility studies

Lam et al. (2012) reported an integrated microfluidic system combined with elastometric micropost arrays and microcontact printing technologies. In an attempt to achieve independent controls and modulations of fluid shear, substrate rigidity and adhesive pattern, the geometry of the elastomeric micropost array in a microfluidic system was investigated. The arrangement of micropost arrays regulated substrate rigidity and adhesive patterns, and could be utilized as force sensors to map live-cell subcellular contractile forces. They investigated the flow-mediated endothelial mechanotransduction process and examined specifically the involvement of subcellular contractile forces in the morphological realignment process of endothelial cells under a sustained directional fluid shear. Lam et al. (2012) claimed that an integrated microfluidic strategy was able to modulate the *in vitro* cellular microenvironment with both defined soluble and insoluble signals. In the case of porous medium, the restricted geometry, such as embedded shapes and sizes of obstacles affects the swimming behaviors and the mechanism of bacterial motility. However, it still remains an unknown field caused by unclear mechanisms of bacteria motility under various microenvironments.

Long and Ford (2009) investigated bacterial dispersion with porous T-sensor microfluidic devices. Bacteria migrations are biased toward higher chemical concentrations; this is called chemotaxis. The chemotactic bacteria Escherichia coli HCB1 and a solution of chemical attractant α-methylaspartate were inserted into a porous microchannel with equal flow rate. Long and Ford (2009) observed that bacterial migration was increased by the attractant stream, and the response of chemotaxis was greater than the predicted values from an advection-dispersion equation model. They also found that flow through a

porous media increased transverse migration for chemotactic bacteria. Figure 2.12 shows that regular circular patterns were arranged in circular cylinders of 200μm diameter, as shown in Fig 2.13.

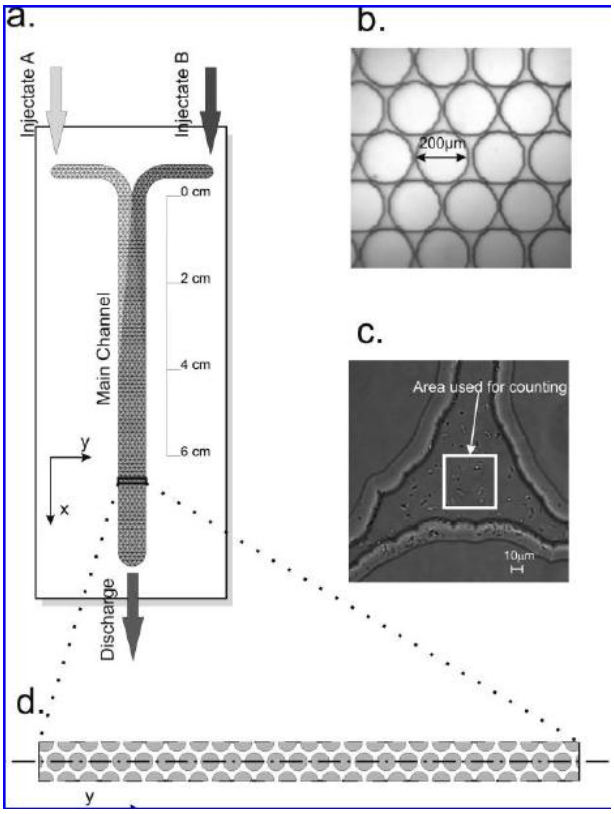

Figure 2.12 a Schematic illustration of the porous T-sensor design **b** an image of the inner obstacles **c** position for chemotaxis analysis **d** microchannel geometry (Long and Ford 2009)

Singh and Olson (2011) used three different pore geometries as shown in Fig 2.13 to increase contaminant mixing. The first was a uniform grain size with large pore throats (MFD-I). Another was a non-uniform grain size with restricted pore space (MFD-II). The third was a uniform grain size with small pore throats (MFD-III). *Escher-ichia coli* HCB 33 was used to investigate the effect of bacterial random motility on transverse mixing of a tracer. A mixing enhancement index (MEI) was defined as the ratio of transverse

dispersion coefficient with motile bacteria and without bacteria. They observed that motile bacteria increased their motility around 5-6 fold in MEI in MFD-II, while a nearly 4-fold increase found in MFD-I. They claimed that pore throat size and pore arrangement play key roles for contaminant mixing in porous media.

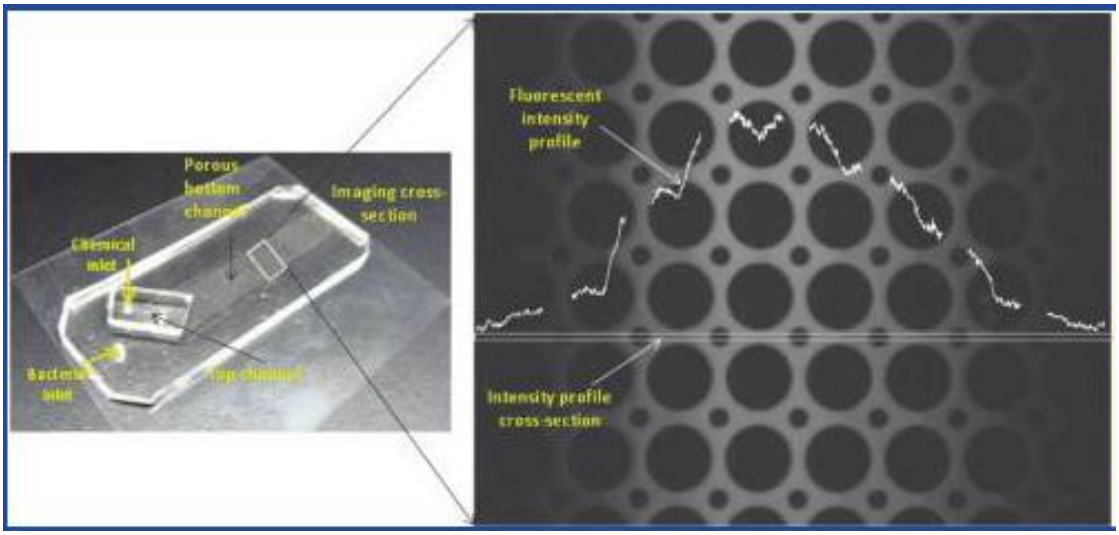

Figure 2.13 A microfluidic chip design (left) and porous structure (right) (Singh and Olson 2011)

2.3 PDMS deformation (bulging) effects during pressure- driven flows

Polydimethylsiloxane (PDMS) is commonly used in soft lithography processes due to its low cost, case of fabrication, transparency, biocompatibility and flexibility. However, the elasticity of PDMS can allow undesired deformation under pressure driven flow. Elastic bulging of microchannels decreases the pressure required to maintain a specific flow rate. Many studies have overlooked such issues during numerical or analytical modeling of PDMS microfluidic systems. PDMS deformation can become severe when pressure driven flow operates at high flow rates. Several attempts to

characterize PDMS deformation and its effect to flow property change have been reported.

Holden et al. (2003) suggested a quantitative technique to measure the bulging in PDMS/glass microfluidic systems. The experimentally determined channel deformation was examined by fluorescence microscopy as shown in Fig 2.14, even though this method did not quantitatively measure channel depth changes.

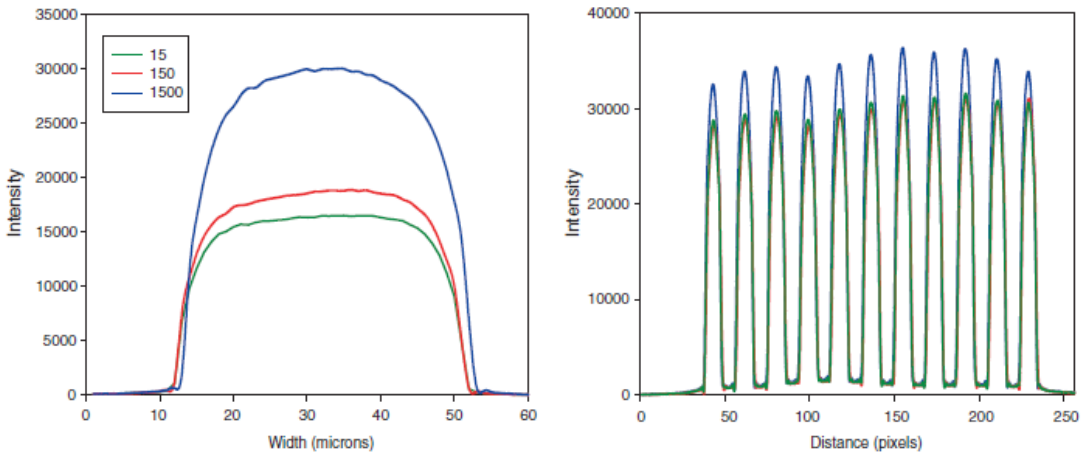

Figure 2.14 a Schematic illustration of a bulging microchannel under the pressure-driven flow **b** background fluorescence intensities subtracted from original intensity (Holden et al. 2003)

Gervais et al. (2006) studied PDMS microchannel deformation under various flow rates using 3D confocal microscopy with Imaris 4.2 image processing software. The non-linear relationship between flow rates and pressure drop indicated that pressure-driven flow gave rise to uncontrolled channel deformation. As expected, microchannel bulging was greatest at the inlet (highest pressure) and least at the microchannel outlet (lowest pressure). These researchers also modeled their microfluidic system utilizing a coupled computational fluid dynamics simulation of flow through a channel with flexible, semi-

infinite walls. Figure 2.15 illustrated 3D simulation results, including the flow velocity and pressure profile under an imposed pressure drop. The cross-sectional area along with the channel axis was related to the change of flow profiles. There was also significant PDMS bulging influence on macroscopic flow parameters. When the flow rates were increased by a factor of two, the pressure drop increment shown in Fig 2.16 was only increased by a factor of 1/2.

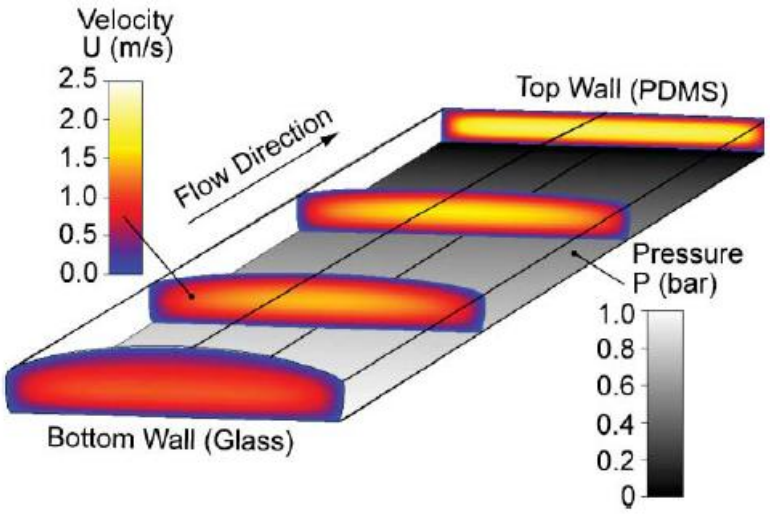

Figure 2.15 3D simulation result of the flow velocity and pressure profile under an imposed pressure drop (Gervais et al. 2006)

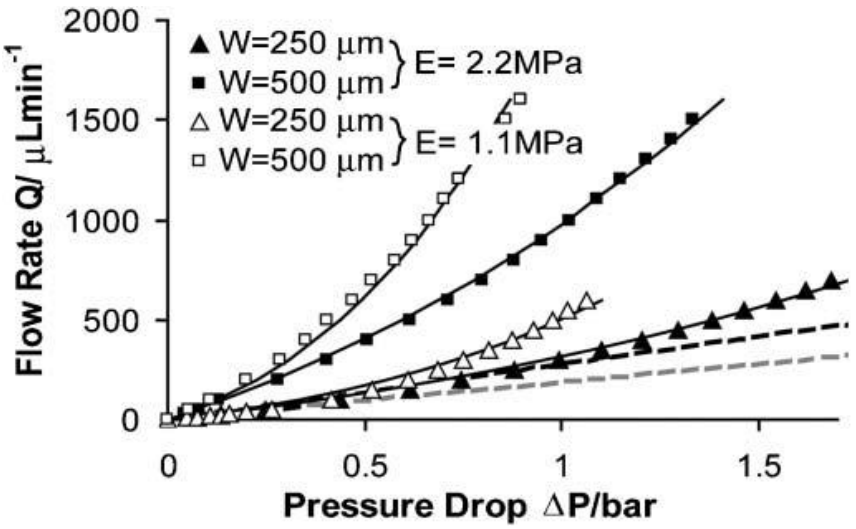

Figure 2.16 Analysis of relationship between flow rate and pressure drop in PDMS channels (Gervais et al. 2006)

Hardy et al. (2009) suggested an alternative fluorescence microscopy method to experimentally characterize the deformation of shallow microfluidic channels as shown in Fig 2.17. They suggested advanced techniques based on their previous work (Holden et al. 2003) to quantify PDSM deformation. A 6μM solution of Rhodamine 6G dye was directly pumped through microfluidic channels and the thickness of the dye layer (i.e., microchannel height) was directly correlated with the fluorescent intensity, enabling determination of the width and longitudinal deformation of the microchannels. They reported a 65% increase in the pressure drop when the flow rates were increased by 100%. Dangla et al. (2010) experimentally measured the deformation of PDMS microchannels when a microchannel was filled by solvents that induced PDMS swellings. The shapes of the channel roof bent inwards and became a parabolic shape. The maximum deformation found was 7μm when hexadecane filled a microchannel 1mm in

width and 50μm in height. They also found that PDMS deformation affected the trajectories of tracer droplets in solvents.

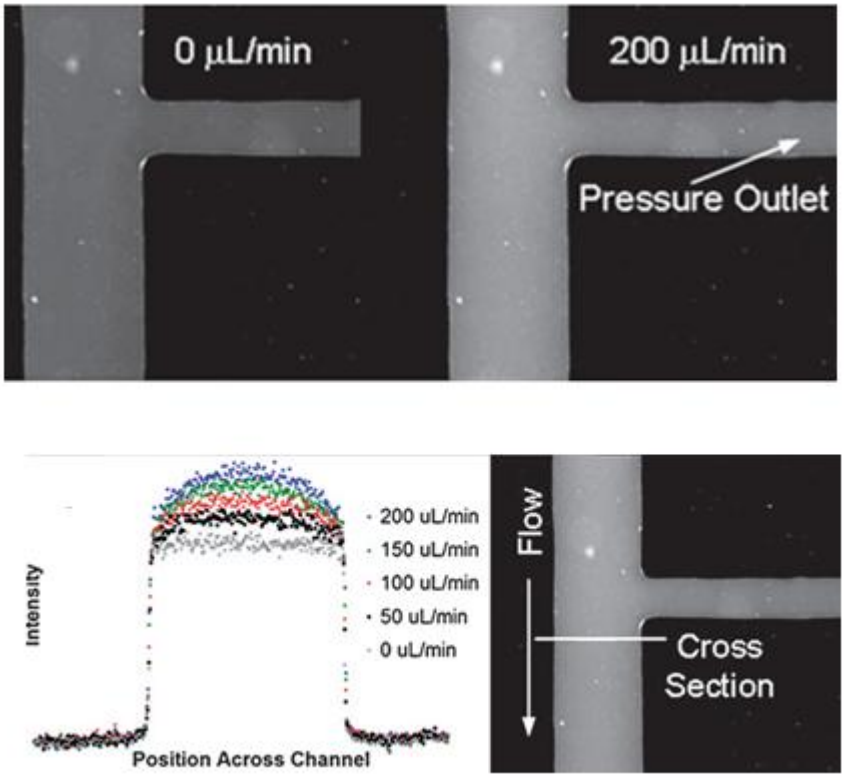

Figure 2.17 Analysis of PDMS deformation with fluorescent intensity (Hardy et al. (2009)

CHAPTER 3

OBJECTIVES OF THE RESEARCH

Obstacles arranged along the centerline of microchannels would be expected to mechanically "pin" the upper PDMS microchannel boundary and minimize bulging of the soft material. However, the preliminary experiments reported here indicated that this was not the case – especially for shallow microchannels. The purpose of this study was to quantitatively examine PDMS bulging effects for microchannels of various depths and containing periodically spaced flow obstacles. Macroscopic flow parameters such as volumetric flow rate, flow velocity, pressure drop and friction factor are known to be significantly dependent upon microchannel geometries. Three specific objectives were expected to be achieved.

Most studies of flow in microfluidic channels seek to obtain steady state conditions through the microchannel chip and ignore (i) transient start-up conditions as well as (ii) bulging-induced dimensional changes along the length of the microchannel. The first objective of the present investigation was to develop experimental techniques to characterize start-up flow in microchannels and theoretically establish the attainment of quasi-steady state flow for comparison with steady state literature data. The concept of hydraulic diameter is frequently used to quantify the dimensional nature of complex flow geometries in macroscopic systems but has been little used for microfluidic devices. Reliable experimental techniques for investigating start-up flows would enable numerous

new studies of microfluidic behavior in conditions of interest to microfluidic sensor engineers.

The second objective of this investigation was to examine the role of linearly arranged flow obstacles to minimize microchannel deformation/bulging effects in PDMS microchannels of various depths. Obstacles and arrays of obstacles of various sizes and geometries are frequently exploited for passive mixing applications in microfluidic systems. Bulging effects are usually ignored in such designs since the embedded obstacles might be expected to constrain the microchannel dimensions are mitigate pressure-induced bulging of the channel top surface. However, no quantitative experimental studies have been reported on this subject and the increasing complexity of microfluidic systems makes understanding such phenomena all the more important. The effects of embedded obstacles and microchannel bulging effects on expected flow parameters of volumetric flow rate, flow velocity, pressure drop and friction factor are especially important.

The third objective was to experimentally investigate the ability of changes in PDMS composition (i.e., mixing ratio) to influence microchannel bulging effects under a pressure driven flows. In addition, a simplified 2D theoretical study of microchannel bulging effects would be expected to provide additional insight and understanding of the phenomenon and provide the basis for more complex 3D microfluidic chip designs.

CHAPTER 4

EXPERIMENTAL PROCEDURES

This chapter reports the experimental procedures to fabricate and characterize the microfluidic behavior in PDMS microchannels of interest. The first portion describes the various materials utilized while the second part describes the silicon wafer fabrication procedures to fabricate shallow (15μm deep) and deep (50, 100 and 200μm) microfluidic channels. The experimental arrangements for measuring the various important flow parameters (e.g., pressure drop, flow velocities) are discussed in the third section. In the last section, quantitative measurements of PDMS microchannel deformation is reported as well as numerical simulations of PDMS stress-strain behavior using the finite element method (FEM).

4.1 Materials

A water-based food dye liquid solution from ESCO Foods Inc. (San Francisco, CA) was utilized for flow property investigations of flow velocities, pressure drops and friction factors for the various microchannels investigated. The density and viscosity of this test liquid were characterized at room temperature by a tensiometer (KSV Sigma 702, Scientific Solutions, Queensland, Australia) and viscometer (Nametre Viscoliner, Lowell, MA), respectively. The density (ρ) was measured as 0.685 ± 0.006 g/cm^3 while the viscosity (μ) was determined to be 1.5625 ± 0.0016cP.

Standard capillary rise measurements were used to characterize the surface tension of the water-based food dye liquid solution. The surface tension is defined as (Nguyen and Wereley 2006)

$$\sigma = \frac{\rho g L R}{2 \cos \theta} \tag{4.1}$$

where ρ is the density of the solution, g is the acceleration due to gravity, L is the length of capillary rise, θ is the liquid/capillary contact angle and R is the radius of capillary tube. The surface tension of the food dye solution used was measured as 58 ± 0.3mN/m.

These properties of the fluid were assumed to be constant for the experiments reported here.

Bulging displacements of the PDMS microchannels during pressure driven flows (described below in Section 4.6) were measured by fluorescence microscopy as a syringe pump delivered a 100μM solution of rhodamine 6G dye (Sigma Aldrich, USA) into the microchannels.

4.2 Microfluidic channel fabrication procedures

4.2.1 Shallow microchannels

AutoCAD software (AutoDesk Inc., San Rafel, CA) was used to produce a mask design which was then printed on a transparent film by CAD/Art Service Inc. (Bandon, OR). The silicon wafer fabrication process by the standard wet etching process is summarized in Figure 4.1. A positive photoresist (AZ P4620) was spin-coated onto a 4 inch silicon wafer by Silicon Quest International Inc. (Santa Clara, CA). Appropriate UV exposure through the transparent mask design followed by photoresist development enabled the basic microchannel chip design to be transferred to glass. A mold of height

(around 5µm) was then placed on the wafer surrounding the photoresist layer. Polydimethylsiloxane (PDMS, GE RTV 615; elastomer: cross-linker=10:1) was then poured onto the wafer inside the mold structure to produce the 5mm thick chip with the fluidic structure to be characterized. The microfluidic channel was cured at 85^{o}C for 1 hour to increase PDMS cross-linking and harden the PDMS. The microfludic channel was then peeled off the wafer/photoresist and holes for inlet and outlet ports were fabricated using a 19 gauge punch (Technical Innovations, Inc., Brazoria, TX). The microfluidic channel and glass slide (Fisher Scientific, Pittsburgh, PA) were exposed to oxygen plasma (Plasma cleaner PDC-326, Harrick Plasma Inc., USA) to make a hydrophilic surface, allowing for easier filling and strong bonding (Eddings et al. 2008). The punched fluidic layer was finally bonded with the control layer.

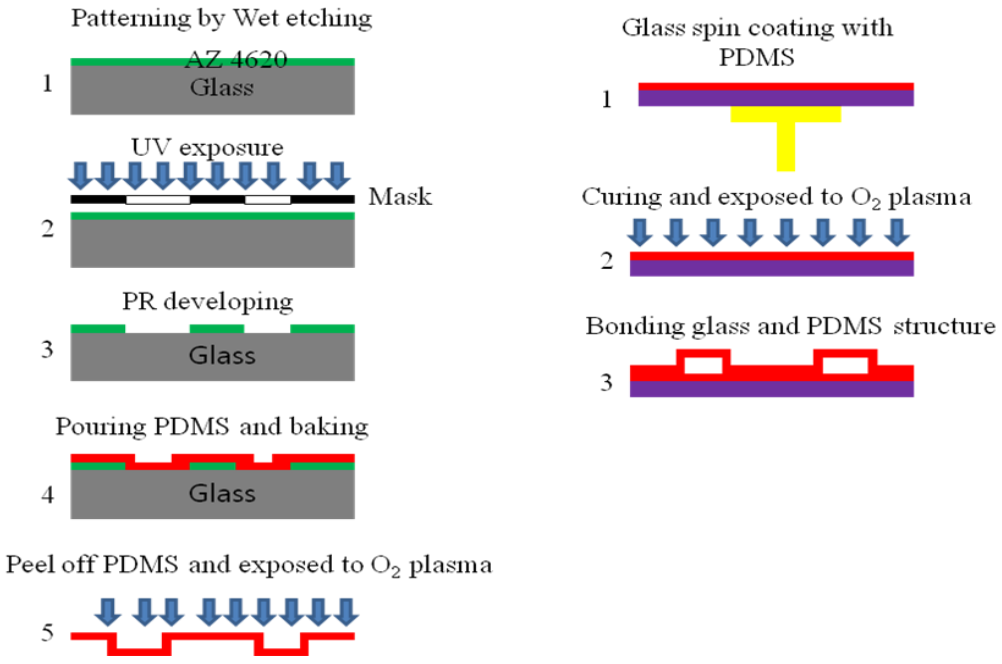

Figure 4.1 Silicon wafer fabrication by wet etching process

4.2.2 Deep microchannels

The fabrication of the deeper microfluidic channels with the embedded obstacles required a different approach to enable maintenance of vertical microchannel surfaces. Reactive ion etching (RIE) techniques are able to make high-aspect-ratio structures with high etching rates, straight sidewalls and complex geometries (Gassend et al.2010; Chen et al.2002) and was utilized for microchannels with depths greater than 15 μm. The process shown in Fig. 4.2 is briefly described below. Software (AutoDesk Inc., San Rafel, CA) was again used to produce a mask design which was then printed on a transparent film by CAD/Art Service Inc (Bandon, OR). As before, positive photoresist (AZ P4620) was applied to a 4 inch silicon wafer by Silicon Quest International Inc. (Santa Clara, CA). The silicon wafers were etched with a Surface Technology system (Redwood, CA) using 30 second etch – 5 second passivation cycles, producing an etch rate of around 2μm/min. Each etch/passivation cycle was followed with oxygen plasma exposure for removal of residual volatile organic species in the chamber and C_4F_8 (Perfluorocyclobutane) deposition for reducing sidewall roughness of the silicon mold. A Teflon coating was applied to the silicon substrate to protect the embedded obstacles inside the microchannels (Thangawng et al. 2007). In order to effectively protect the silicon wafer structures after completion of the etch/passivation cycles, the silicon wafer was additionally coated with (1,1,2,2 H perfluorooctyl)- trichlorosilane (PFTS). Surface coating with this chemical increased the silicon surface hydrophobicity so that the silicon mold-PDMS replica was less likely to stick together (Gao et al. 2006; Bubendorfer et al. 2007). The silicon surface uniformity achieved through reactive ion etching (RIE) was within 5% of design channel dimensions. The value of average surface roughness (Ra)

measured by surface profilometer (Veeco Dektak 150 Stylus, Bruker) ranged from 0.12μm to 0.18μm. Polydimethylsiloxane (PDMS, GE RTV 615; elastomer: cross-linker=10:1) was then poured onto the wafer inside the mold structure to produce the 5mm thick chip with the fluidic structure to be characterized. PDMS was also directly poured onto a glass slide to prevent a leaking by enhancing PDMS-PDMS bonding (Eddings et al. 2008). The membrane thickness of the glass layer was controlled to 10 ± 0.5μm by 60s of spinning at 28000 rpm. Just like previously described for the shallow microchannels, the fluidic chip layer was cured at 85^{o}C for 1 hour for PDMS cross-linking while the glass layer was cured at 85^{o}C for 10min. The fluidic layer was then peeled off the wafer/photoresist and holes for inlet and outlet ports fabricated using a 19 gauge punch (Technical Innovations, Inc., Brazoria, TX). The microfluidic channel and glass slide (Fisher Scientific, Pittsburgh, PA) were exposed to oxygen plasma (Plasma cleaner PDC-326, Harrick Plasma Inc.,USA) to make a hydrophilic surface, allowing for easier liquid filling and strong bonding (Eddings et al. 2008). The punched fluidic layer was then bonded with the glass layer.

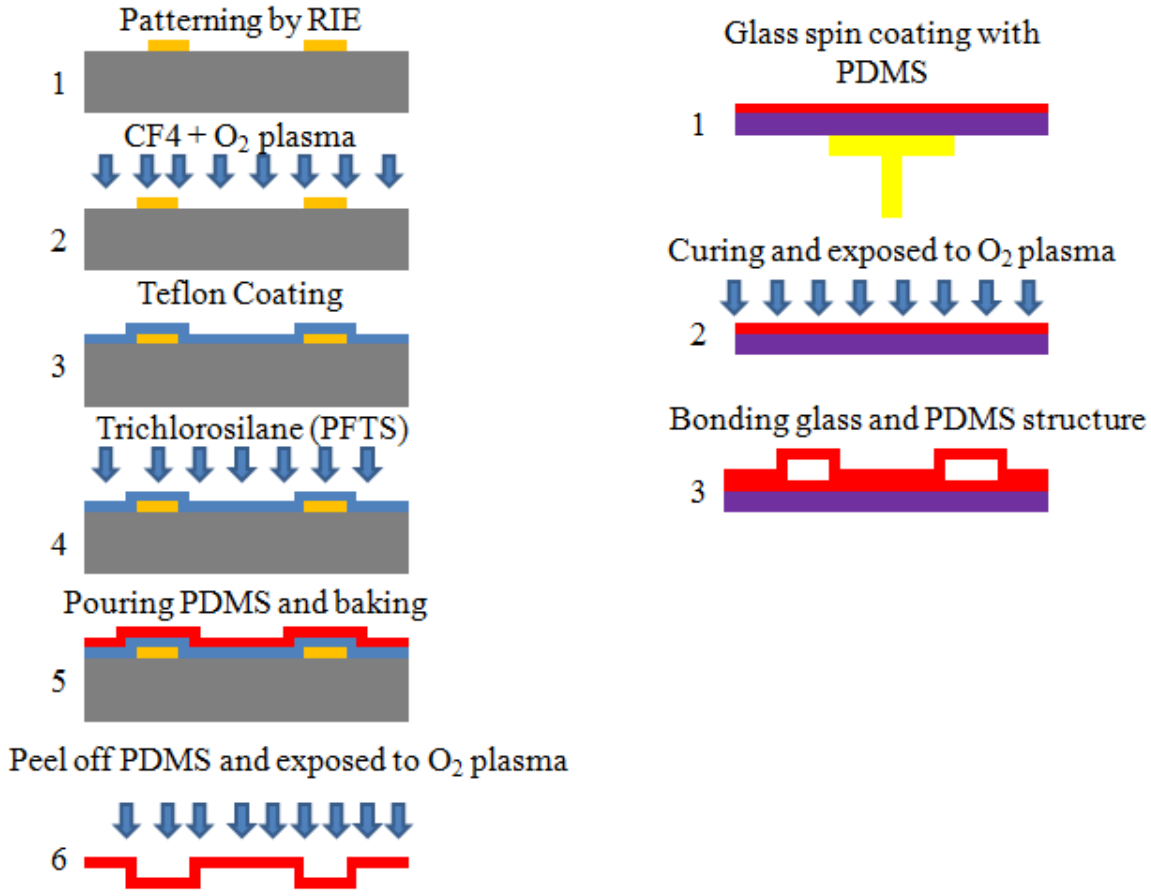

Figure 4.2 Microchannel fabrication process by reactive ion etching (RIE) technique

4.3 Microchannel geometries studied

By means of wet etching techniques, the shallow microfluidic channels had a measured width equal to 243±1μm and a measured height of 15±1μm. An aligned row of periodic obstacles was arranged along the centerline of each channel. The obstacle shapes that were investigated included circles, squares, hexagons and equilateral triangles with the obstacle geometries and characteristic lengths as defined in Figure 4.3. The microfabricated obstacles in this study exhibited characteristic lengths of 132μm, 152μm and 172μm. All obstacles were the same height as the channel and securely bonded to the

PDMS base layer with no gap between any obstacle and the microfluidic channel base layer.

Table 4.1 summarizes the investigated microfluidic channel and obstacle dimensions as well as the calculated hydraulic parameters of mean hydraulic diameter and mean porosity. The mean porosity is simply evaluated as the ratio of the channel volume available for flow to the total channel volume. As shown in Table 4.1, the minimum gaps between the obstacles and the channel walls were maintained at 35.6, 45.6 and 55.6μm for the largest to smallest obstacles, regardless of obstacle shape.

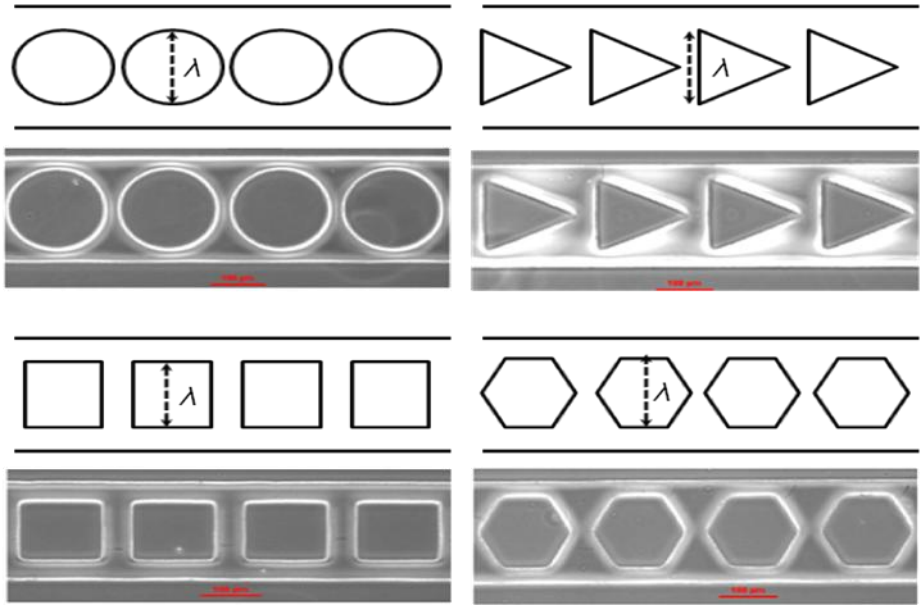

Figure 4.3 Close-up image of the obstacles used in shallow microfluidic channels (15μm)

Table 4.1 Dimensions and hydraulic parameters of the fabricated shallow (15μm depth) microfluidic chip systems

Obstacle and Microchannel Depth (H)	Obstacle Characteristic Length (λ)* (mm)	Overall Microchannel Length (L) (mm)	Minimum Obstacle to Wall Gap (μm)	Minimum Obstacle to Obstacle Gap (μm)	Mean Porosity (%)
FC2_15μm	0.172	10.1	35.6	35.6	54
FC3_15μm	0.152	9.63	45.6	45.6	62
FC4_15μm	0.132	9.14	55.6	55.6	70
FH2_15μm	0.172	10.1	35.6	35.6	56
FH3_15μm	0.152	9.63	45.6	45.6	64
FH4_15μm	0.132	9.14	55.6	55.6	72
FS2_15μm	0.172	10.1	35.6	35.6	41
FS3_15μm	0.152	9.63	45.6	45.6	52
FS4_15μm	0.132	9.14	55.6	55.6	62
FT2_15μm	0.172	10.1	35.6	35.6	71
FT3_15μm	0.152	9.63	45.6	45.6	76
FT4_15μm	0.132	9.14	55.6	55.6	81

The mean hydraulic diameter (sometimes called the equivalent diameter) was calculated in the usual way as

$$D_H = \frac{4 \times cross\,sectional\ flow\ area}{wetted\ \ perimeter}\left(\frac{L}{L}\right) = \frac{4 \times channel\ volume\ available\ for\ flow}{total\ wetted\ channel\ surface\ area} \qquad (4.2)$$

The maximum hydraulic diameter of 28.26μm is that for channels without any obstacle. The presence of obstacles naturally reduces the calculated values of hydraulic diameter. For the present set of experiments, the mean hydraulic diameters for channels with obstacles varied from 21.39~25.72μm.

The microfluidic channels produced by reactive ion etching (RIE) had a measured width of also 243±1 μm and measured depths of 50±2μm, 100±5μm, and 200±8μm, respectively. As before, an aligned row of periodic obstacles was arranged along the centerline of each channel. The circular obstacle geometries and characteristic lengths are defined in Table 4.2. The microfabricated obstacles in this study exhibited the same characteristic lengths as the shallow microfluidic channels. Table 4.2 summarizes the investigated microfluidic channels and obstacle dimensions as well as the calculated hydraulic parameters of the mean hydraulic diameter, which was calculated in the usual way as Eq. (4.2). In this experiment, the mean hydraulic diameters for channels with different channel height varied from 52.88 to 113.61 μm. The aspect ratio, ε, was calculated by

$$\varepsilon = \frac{H\ (Channel\ height)}{W\ (Channel\ width)} \tag{4.3}$$

The aspect ratios shown in Table 4.2 were 0.21, 0.41 and 0.82, respectively. As shown in Table 4.1, the minimum gaps between the obstacles and the channel walls were maintained at 35.6, 45.6 and 55.6 μm for the largest to smallest obstacles.

Table 4.2 Dimensions and hydraulic parameters of the fabricated deep microfluidic channels

	Obstacle Characteristic Length (λ) (mm)	Overall Microchannel Length (L) (mm)	Obstacle to wall Gap (μm)	Obstacle to Obstacle Gap (μm)	Mean As-fabricated Hydraulic Diameter (μm)	Aspect Ratio (H/W)
FC2_50μm	0.172	10.1	35.6	35.6	52.9	0.210
FC2_100μm	0.152	9.63	45.6	45.6	71.9	0.410
FC2_200μm	0.132	9.14	55.6	55.6	87.6	0.820
FC3_50μm	0.172	10.1	35.6	35.6	57.4	0.210
FC3_100μm	0.152	9.63	45.6	45.6	80.4	0.410
FC3_200μm	0.132	9.14	55.6	55.6	100	0.820
FC4_50μm	0.172	10.1	35.6	35.6	61.3	0.210
FC4_100μm	0.152	9.63	45.6	45.6	88.5	0.410
FC4_200μm	0.132	9.14	55.6	55.6	114	0.820

4.4 Measurement of flow velocity during transient start-up flows

In experiments on the shallow as well as the deeper microchannels, the experimental setups were the same and are shown schematically in Fig. 4.4. Tygon tubing (0.06” OD x 0.02” ID, Saint-Gobain Corp., Akron, OH) connected a syringe pump (Harvard Apparatus, Holliston, MA) to the microfluidic chip through a needle (0.025”OD x 0.013”ID, New England Small Tube Crop., Litchfield, NH) at the microfluidic chip inlet. The flow rates investigated in this study were maintained constant by the syringe pump

(±0.5% accuracy) at either 1.0µl/min or 2.0µl/min depending upon the experimental protocol. The transient position of the flow front along the microfluidic channel was followed by microscopic observation (Nikon Ti/U E20L80 Inverted Microscope, Japan) and recorded with an image intensifying CCD camera (Nikon Digital Sight DS-Q1MC). The camera pixel size was 1280 X 1024 pixels, and individual images were acquired at a rate of 19 frames per second. The recorded image movie files enabled direct determination of the position of the liquid front as a function of time and also calculation of the velocity of the liquid front versus time. The position of liquid front was analyzed by Nikon Elements software.

Each experiment was repeated a minimum of three times and new, unused microfluidic channels were used for each experimental measurement to eliminate the effect of systematic errors which might possibly arise due to the surface quality of the channels, surface chemistry, contamination, etc.

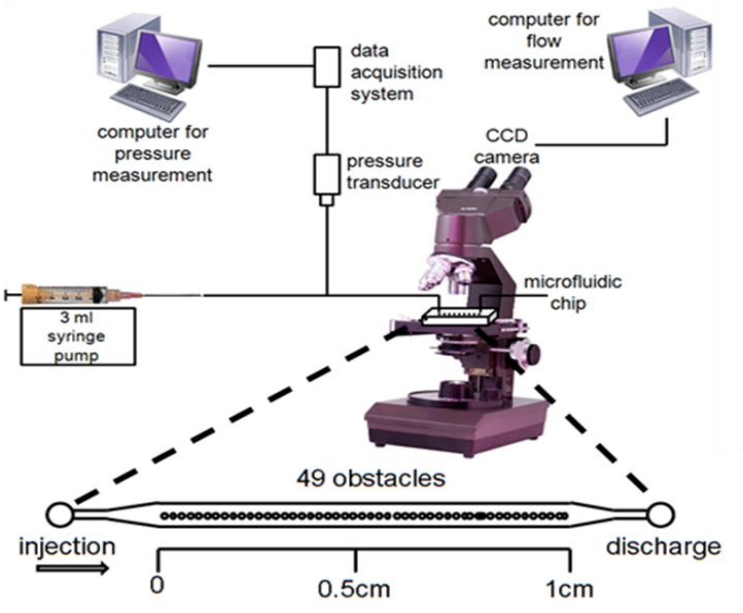

Figure 4.4 Schematic of the experimental apparatus in shallow and deep microfluidic channels

The experimental Reynolds number was calculated using the mean hydraulic diameter $\overline{D}_H$, the mean fluid velocity $\overline{V}$ (determined from the optical measurements) as well as the fluid density ρ and dynamic viscosity μ. Thus

$$Re = \rho \overline{V} \overline{D}_H / \mu \tag{4.4}$$

$\overline{D}_H$ is equal to the inner diameter for circular tubes and $\overline{D}_H = 2wh/(w+h)$ for rectangular channels where *w*=width and *h*=height.

The Darcy friction factor *f* is often used to characterize viscous losses in microfluidic systems and is defined as

$$f = \overline{D}_H \frac{\Delta P}{L} \frac{1}{\rho \overline{V}^2 / 2} \tag{4.5}$$

where *ΔP/L* is the steady state pressure drop per unit channel length (see Section 6.1.2).

For circular tubes $f = 64/Re$. *fRe* is known as the Poiseuille number (*Po*) and is a constant 64 for circular tubes. White (1994) shows that the Darcy friction factor for rectangular channels is a function of the channel's aspect ratio (α = *w/h*) of the rectangular channel. α varies from 1 for square channels to 0 for narrow rectangular channels and White showed that *fRe* varies from 56.9 for square channels to 96 for narrow rectangular channels.

4.5 Measurement of pressure drops

The time-dependent applied pressure was directly measured throughout each entire experiment by a gauge pressure transducer (PX138, Omega Engineering Inc., Stamford, Connecticut). The transducer voltage was digitized and recorded with a computerized

data acquisition system (DI-148U, DATAQ Instrument, Arkon, OH). Calibration of the pressure transducer voltage was performed using a water manometer prior to beginning experiments on the microfluidic devices. The outlet channel in the microfluidic channel was open to the atmosphere and remained at atmospheric pressure for the entire duration of the experiment. The pressure data recorded on one computer (see Fig. 4.4) were time stamped at the moment when the liquid front just touched the first obstacle, allowing time synchronization with the CCD image files recorded by the second computer (see Fig. 4.4).

4.6 PDMS microfluidic channel deformation measurement

The experimental microfluidic channels were strongly sealed on rigid glass slides to eliminate any bulging distortion at the glass bottom the the microfluidic channels. The measured pressures were always well below the critical pressure for debonding the PDMS/glass interface (Wu et al. 2010). Bulging displacements during pressure driven flows were measured by fluorescence microscopy (Nikon Ti/U E20L80 Inverted Microscope, Japan) as the syringe pump delivered a 100μM solution of rhodamine 6G dye into the microchannels. As shown in Fig. 4.5 a line scan technique was used to measure the intensity of the fluorescence dye as it moved through the microchannel. The measured fluorescence intensity was proportional to the rhodamine dye thickness as established by Hardy et al. (2009). The florescence intensity was initially measured at a zero flow rate and zero pressure for the various microchannel depths to establish the relationship between fluorescence intensity and rhodamine dye thickness.

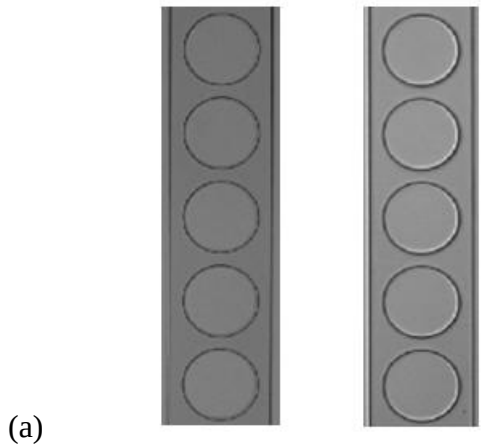

(a)

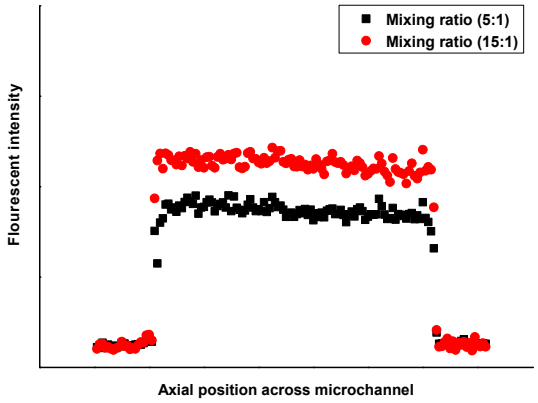

(b)

Figure 4.5 a Images of channel section with various mixing ratios at constant flow rate (1.0µl/min) (left: 5:1, right: 15:1) and line scan (red line) **b** analysis of fluorescent intensity by various mixing ratios

4.7 Tensile testing of PDMS materials

The elastic modulus of PDMS is the most important mechanical property controlling elastic bulging effects during pressure-driven flow. Standard tensile tests were used to measure the elastic modulus of PDMS tensile samples prepared with various mixing ratios and thicknesses of PDMS samples. Silicone RTV 615 (Momentive performance materials, NY, USA) consisting of part A and part B was used in this study. Part A of

RTV 615 is a siloxane oligomer, containing polydimethylsiloxane, while Part B of RTV 615 is the cross-linking oligomers, containing a cross-linker. The covalent bonding between the vinyl group of part A and silicon hydride of part B can be formed during the mixing process (Liu and Chen 2007). To measure the mechanical properties, PDMS tensile specimens with three different mixing ratios (ratio of A:B = 5:1, 10:1 and 15:1) were prepared with two different PDMS wall thickness (3mm and 6mm). Part A and Part B were well mixed with suggested ratios and the solution was poured into the prepared mold (4cm x 6cm). After degassing, the PDMS was cured at 85°C for 1hr. The cured PDMS was peeled off the mold and cut into samples.

Tensile testing was accomplished using a screw-driven Instron 4400R (Instron Inc., MA, USA) universal material testing machine in accordance with ASTM D3574, as shown in Fig. 4.5. Prior to the actual test, each specimen was very carefully inspected for any visible defect (i.e., crack, bubble, etc.). The test sample was mounted on specially created double-sided grippers to prevent slippage of the specimen as shown in Fig. 4.6. A tensile force was then applied to control specimens. Mechanical data such as the elongation of the PDMS and the corresponding force were automatically recorded on a computer and repeated several times. An example of the relationship between the computed stress and the corresponding strain was plotted in Fig.4.7 according to the experimental measurements of the elongation and the corresponding force. Stress and strain of the PDMS specimens was found to exhibit a linear relationship and the elastic modulus computed as the slope of the stress-strain curve.

(a) 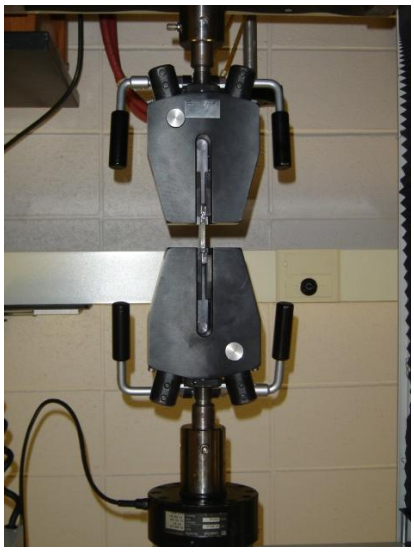 (b) 

Figure 4.6 a The experimental apparatus for the mechanical properties (before) **b** the experimental apparatus for the mechanical properties (after)

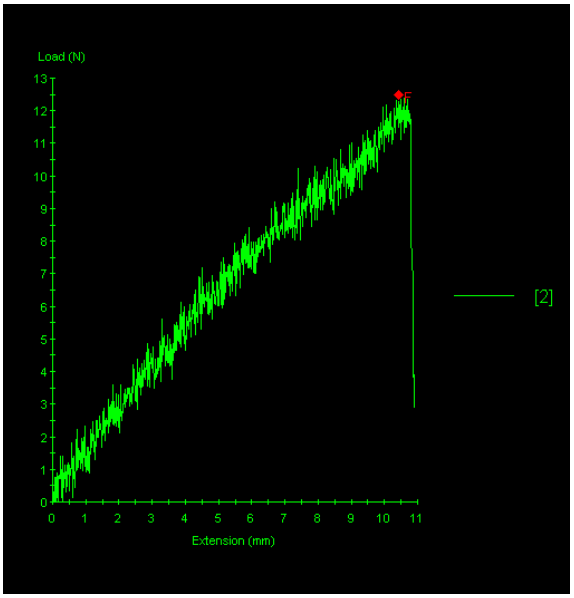

Figure 4.7 The experimental measurements of loads and displacement

4.7 Uncertainty analysis

Careful consideration of various sources of measurement uncertainties are a prerequisite for reliable interpretation of experimental results of pressure drops and friction factors in microchannels. The total uncertainty, U_G, propagating throughout an experimental measurement can be estimated using standard procedures (Moffat, 1988; Holman, 1989). When a total of j independent variables X are utilized to calculate a parameter G, the individual contributions to uncertainty from each individual measurement, U_j, to the total uncertainty, U_G, can be estimated by the root-sum-square method. Thus

$$U_G = \left[\left(\frac{\partial G}{\partial X_1} U_1 \right)^2 + \left(\frac{\partial G}{\partial X_2} U_2 \right)^2 + \ldots + \left(\frac{\partial G}{\partial X_j} U_j \right)^2 \right]^{1/2} \tag{4.6}$$

$\frac{\partial G}{\partial X_j}$ are often called the sensitivity coefficients of the parameter G on the variables X_j. If G is a product solution of the form $G = X_1^{a_1} X_2^{a_2}, \ldots, X_J^{a_J}$, then the fractional uncertainty in G can be expressed as

$$\frac{U_G}{G} = \left[\sum \left(\frac{a_j}{X_J} U_J \right)^2 \right]^{1/2} \tag{4.7}$$

Application of the above equation to the definition of the microfluidic friction factor yields the fractional uncertainty in the measurements of the friction factor f as

$$\frac{U_f}{f} = \left[\left(\frac{U_{\bar{D}_H}}{\bar{D}_H} \right)^2 + \left(\frac{U_{\Delta P}}{\Delta P} \right)^2 + \left(\frac{U_L}{L} \right)^2 + \left(\frac{U_\rho}{\rho} \right)^2 + \left(\frac{2U_{\bar{V}}}{\bar{V}} \right)^2 \right]^{1/2} \tag{4.8}$$

CHAPTER 5

ANALYSIS OF TRANSIENT FLOWS IN MICROCHANNELS

5.1 Analysis of pressure drops

The measured pressure, P_{System}, in the microfluidic system (see Fig. 4.5) during each transient start-up experiment is composed of the pressure drops through the chip connection tubing (ΔP_{Tubing}), chip injection needle (ΔP_{Needle}), chip entrance region ($\Delta P_{Entrance}$), obstacle region along the microchannel ($\Delta P_{Obstacles}$), capillarity effects due to the fluid free surface (ΔP_{Cap}) and the microchannel exit losses (ΔP_{Exit}). Thus

$$P_{System}=\Delta P_{Tubing}+ \Delta P_{Needle}+\Delta P_{Entrance}+\Delta P_{Obstacles}+\Delta P_{Cap}+\Delta P_{Exit} . \quad (5.1)$$

During start-up flow when the fluid front has not reached the end of the microchannel, the pressure drop due to the air exiting the microchannel in front of the liquid flow is negligible at the low flow rates used in this study. The total pressure required to drive the fluid through the apparatus tubing, injection needle, microchannel entrance region and to overcome microchannel capillarity effects up to when the fluid just reaches the first obstacle can be experimentally measured by the pressure transducer when the fluid initially contacts the first obstacle.

The pressure drop associated with capillarity effects ΔP_{Cap} at the liquid free surface is a large and non-negligible component of P_{System}. Huang et al. (2006) suggested that the capillary pressure drop inside rectangular microchannels can be calculated as

$$\Delta P = \frac{2(H + W)\sigma \cos \Theta}{HW} \tag{5.2}$$

where H is channel height, W is the channel width, σ is the liquid-air surface tension, and Θ is the liquid contact angle with the surfaces. Contact angles measured during filling of the microchannels in this study varied from 78-57^{o}. Thus ΔP_{Cap} can be estimated as 0.52-1.99 kPa for the microchannel dimensions of H (15 - 200μm) and W (243μm) used in this study. The capillary pressure drop would obviously rise as the flow divided and spread around individual obstacles to fill the two gaps between each obstacle and the microchannel sidewalls. Maximum values of ΔP_{Cap} can then be estimated as 1.59-2.23 kPa for the obstacle/sidewall gap dimensions of H (15 - 200μm) and W (35.6-55.6 μm) shown in Table 4.1.

5.2 Analysis of transient flows

Theoretically calculating the dynamics of transient liquid flow through microfluidic channels begins with Newton's second law applied to fluid motion. Figure 5.1 shows a free-body diagram of liquid flowing through a microchannel. Newton's second law states

$$\sum F = F_{\Pr essure} - F_{Viscous} - F_{Capillary} = m \frac{dv}{dt} \tag{5.3}$$

When the microfluid enters a new region of the microchannel (of particular interest here is the region containing the obstacles), the viscous drag forces increase due to the increased microchannel surface area, the capillary forces increase due to the decreased average cross sectional area and the pressure force increases to compensate in response to the syringe pump's constant volumetric flow rate requirement. In these experiments, the appearance of obstacles to liquid flow entering the microchannel leads to a transient

period of fluid acceleration to increase the average fluid velocity. This physical situation is very similar to that encountered during classical start-up flows except that in this case the original velocity is very low but not quite zero as is the case for classical start-up flow conditions.

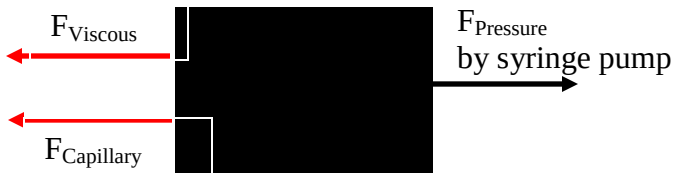

Figure 5.1 Free-body diagram schematic of liquid entering a microchannel

Tabeling (2005) examined the case of start-up flow of a compressible fluid driven by a constant flow rate syringe pump in a rigid microchannel. He showed that achievement of steady state conditions in such a first-order system would only occur after a certain amount of time had elapsed. The system time constant τ in his analysis was associated with the dimensions of the microchannel as well as the fluid viscosity and elasticity. Tabeling found that the microfluidic system behaved as a first order system and the time dependent pressure driving the microfluid varied as

$$P(t) = P_{SS}\,[1-\exp(-t/\tau)] \qquad (5.4)$$

where P_{SS} is the final steady state pressure. Other researchers have utilized first-order system approaches to understand more macroscale start-up problems like start-up of water supply pipes, sewer pipes and oil pipelines (Zhang and Vairavamoorthy 2005; Tijsseling 1996; Gornam et al. 2000; Ambastha and Zhange 1996). As discussed in the

next chapter, a similar first-order system methodology will be adopted to characterize the flow behavior in this work.

CHAPTER 6

RESULTS AND DISCUSSION

6.1 Experimental characterization of flow behavior

6.1.1 Microchannel deformation effects on Hagen-Poiseuille relation

Rigid microfluidic channels exhibit a linear relationship between the imposed flows and the pressure drop developed along the channel, consistent with the Hagen-Poiseuille relationship (Eq. 1.6). However, microfluidic channel deformation fabricated from flexible PDMS can lead to non-linear behavior as a result of uncontrolled microfluidic channel expansion. Moderate and high aspect ratio microfluidic channels can exhibit bulging of the channels and decrease the pressure needed to drive a given volumetric flow rate (Holden et al. 2003). The variation of pressure drop developed across a range of imposed flow rates for a 15μm deep microchannel with the smallest characteristic length of obstacles (FC4) is shown in Fig. 6.1. Such non-linear experimental behavior indicates significant bulging effects of the PDMS microchannels (Gervais et al. 2006).

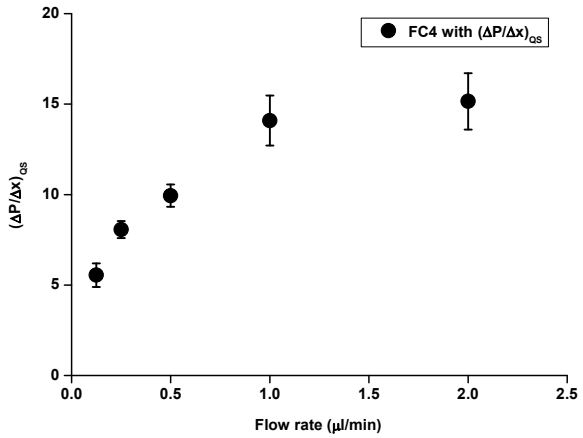

Figure 6.1 Experimentally determined relationship between the measured pressure drops and flow rate in 15μm shallow microfluidic channels containing circular obstacles (FC4)

The variations of pressure drop developed across a range of imposed flow rates for three different depths of microfluidic channels with circular obstacles (FC2) are shown in Fig. 6.2. Significant non-linear behavior is again seen in the 50 μm deep microchannels while the 100 μm deep microchannels exhibit noticeably less non-linearity. The 200 μm deep microchannels almost (but not quite) exhibit linear behavior. The decrease in non-linearity indicates a decrease in the amount of bulging associated with deeper channel depths. As might be expected from simple geometric considerations, shallow microfluidic channels with their correspondingly larger pressures would be expected to exhibit greater PDMS bulging effects than similar but deeper microchannels.

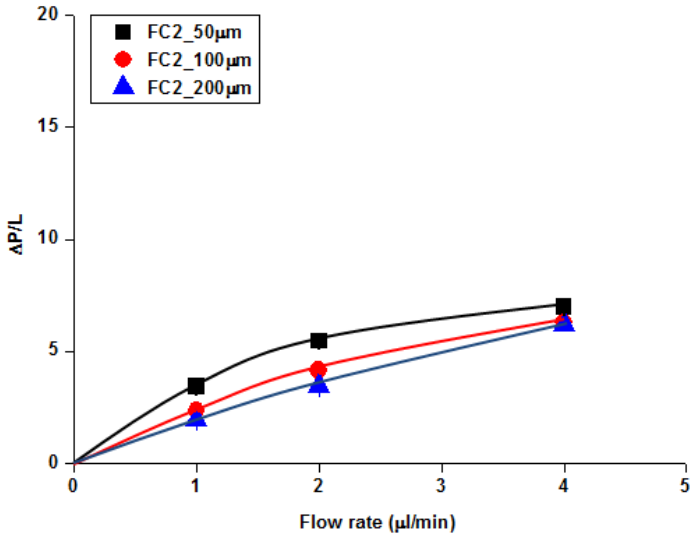

Figure 6.2 Experimentally determined relationship between the measured pressure drop and flow rate in 50-200µm deep microfluidic channels containing circular obstacles (FC2)

6.1.2 Characterization of microchannel deformation

The experimental microchannels were strongly bonded to rigid glass slides to eliminate any distortions along the microchannel bottoms. The measured pressures were all well below those expected to cause debonding at the PDMS/glass interface (Wu et al. 2010). Bulging-induced displacements during pressure driven flows was measured by fluorescence microscopy as the syringe pump delivered a 100µM solution of rhodamine 6G dye into the microfluidic channels. A line scan technique as shown in Fig. 6.3a was used to measure the intensity of the fluorescence dye as it along the microchannel. The PDMS microfluidic channel deformation can be observed in the increased fluorescence intensity with increasing flow rates, as shown in Fig. 6.3b. The principle of this measurement is based on rhodamine dye thickness (i.e., microchannel depth), which is proportional to fluorescence intensity (Hardy et al. 2009). Florescence intensity was

initially measured at a zero flow rate with an undeformed micochannel with the depth (H) was at its initial value. The initial value was then used to characterize the relationship between fluorescence intensity and rhodamine dye thickness. Note that the line scans shown in Fig. 6.3b indicate uniform depths across the microfluidic channel rather than a maximum depth at the center of the microchannel as reported by Gervais et al. (2006) for microchannels without obstacles.

Microfluidic channel deformation data in this study were collected at three different positions along the length of the microchannel (inlet, middle, and outlet) and under two flow rates. Tables 6.1 and 6.2 show the estimated experimental hydraulic diameters of the microchannels, modified as a result of bulging deformation. The percentage differences shown were calculated from the difference between the mean as-fabricated hydraulic diameters and these experimentally determined mean bulging-modified hydraulic diameters. As expected, the maximum difference was observed in the shallowest (15μm deep) channels with the largest obstacle characteristic lengths tested at the highest flow rate of 2μl/min.

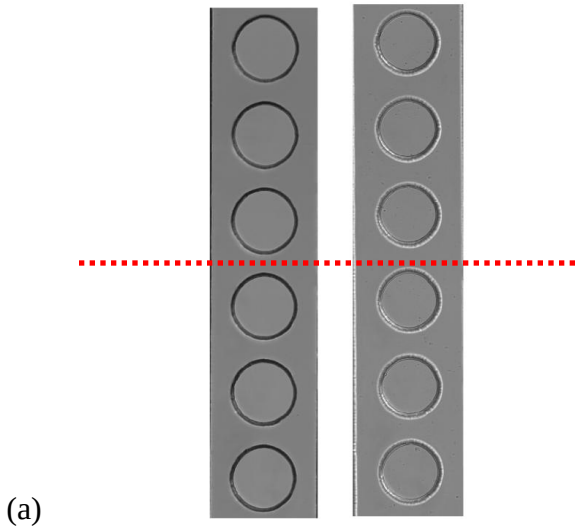

(a)

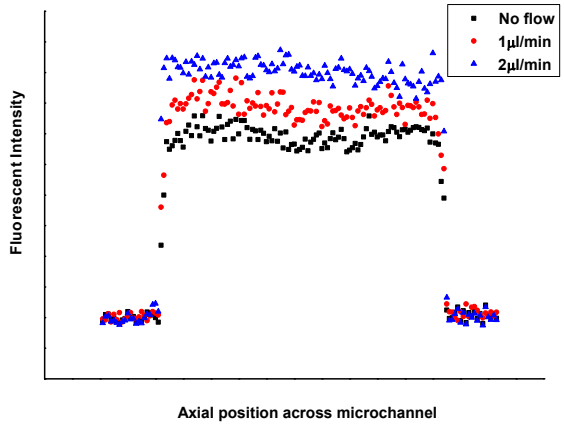

(b)

Figure 6.3 a Images of the channel section with mixing ratios (Left: no flow, Right: 2μl/min) and line scan (Red line) in 50μm channel depth **b** comparison of fluorescence intensity by flow rates

Table 6.1 Summary of channel dimensional changes in shallow (H=15μm) microfluidic channels due to PDMS deformation

Obstacle	Mean As-fabricated Hydraulic Diameter (μm)	1.0μl/min		2.0μl/min	
		Mean Bulging Modified Hydraulic Diameter (μm)	Difference (%)	Mean Bulging Modified Hydraulic Diameter (μm)	Difference (%)
FC2	23.7	25.6	7.42	25.7	7.78
FC3	24.5	26.4	7.20	26.5	7.55
FC4	25.2	27.0	6.67	27.1	7.01
FH2	23.8	25.7	7.98	25.8	8.40
FH3	24.6	26.4	7.32	26.7	8.54
FH4	25.2	27.0	7.14	27.1	7.54
FS2	21.4	23.2	8.41	23.3	8.88
FS3	22.9	24.7	7.86	24.9	8.73
FS4	24.1	25.6	6.22	25.9	7.47
FT2	24.9	26.4	6.02	27.1	8.84
FT3	25.3	26.5	4.74	27.2	7.51
FT4	25.7	26.6	3.50	27.3	6.23

Table 6.2 Summary of dimensional changes in deep (H=50-200μm) microfluidic channels due to PDMS deformation

Obstacle and Microchannel Depth (H)	Mean As-fabricated Hydraulic Diameter (μm)	1.0μl/min		2.0μl/min	
		Mean Bulging Modified Hydraulic Diameter (μm)	Difference (%)	Mean Bulging Modified Hydraulic Diameter (μm)	Difference (%)
FC2_50μm	52.9	56.5	6.37	56.8	6.87
FC2_100μm	71.9	74.9	4.01	75.7	5.02
FC2_200μm	87.6	90.7	3.42	90.8	3.52
FC3_50μm	57.4	60.3	4.81	60.4	4.97
FC3_100μm	80.4	82.4	2.43	82.5	2.55
FC3_200μm	100	102	1.96	103	2.91
FC4_50μm	61.3	63.7	3.77	64.3	4.67
FC4_100μm	88.5	90.5	2.21	90.8	2.53
FC4_200μm	114	115	0.87	116	1.72

6.1.3 Pressure and velocity data during transient start-up flows

Figure 6.4 a- 6.4 f shows typical results for a series of images of the fluid front as it moves through a shallow microfluidic channel (15μm) with circular obstacles having a characteristic length of 0.172 mm (FC2) and an imposed flow rate of 1μl/min. Similarly, figure 6.5 a- 6.5 f shows a series of images of the fluid front with a deep microfluidic channel (200μm) with the same shape, characteristic length of obstacle, and imposed flow rate as a shallow microfluidic channel. These images show that the fluid front sequentially flowed around the sides of each circular obstacle, filled the gaps between

obstacles, and then repeated the process flowing around the next obstacle. To enhance spatial and temporal repeatability, the flow velocity and pressure were measured when both sides of flow simultaneously touched an obstacle and just before the flow began envelopment of the obstacle. The measured spatial variability was less than 20μm in all cases. For the obstacles and flow rates reported here, no evidence was seen of bubble formation from any air entrapment during the flow experiments.

Figure 6.6 shows the experimentally determined fluid front meniscus position versus time and system pressure versus time data for the FC2 circular obstacles in a 50μm deep microchannel for imposed flow rate of 1 μl/min. The slope of the meniscus position versus time plot of Fig 6.6a is the fluid front velocity. The velocity is seen to begin from a very low initial value at the first obstacle and then increase to what appears to be an almost constant value as the liquid front moves along the microchannel. The measured system pressure shown in Fig. 6b begins at approximately 1.3 kPa and then increases to what appears to be a more or less constant value of system pressure equaling about 1.9 kPa.

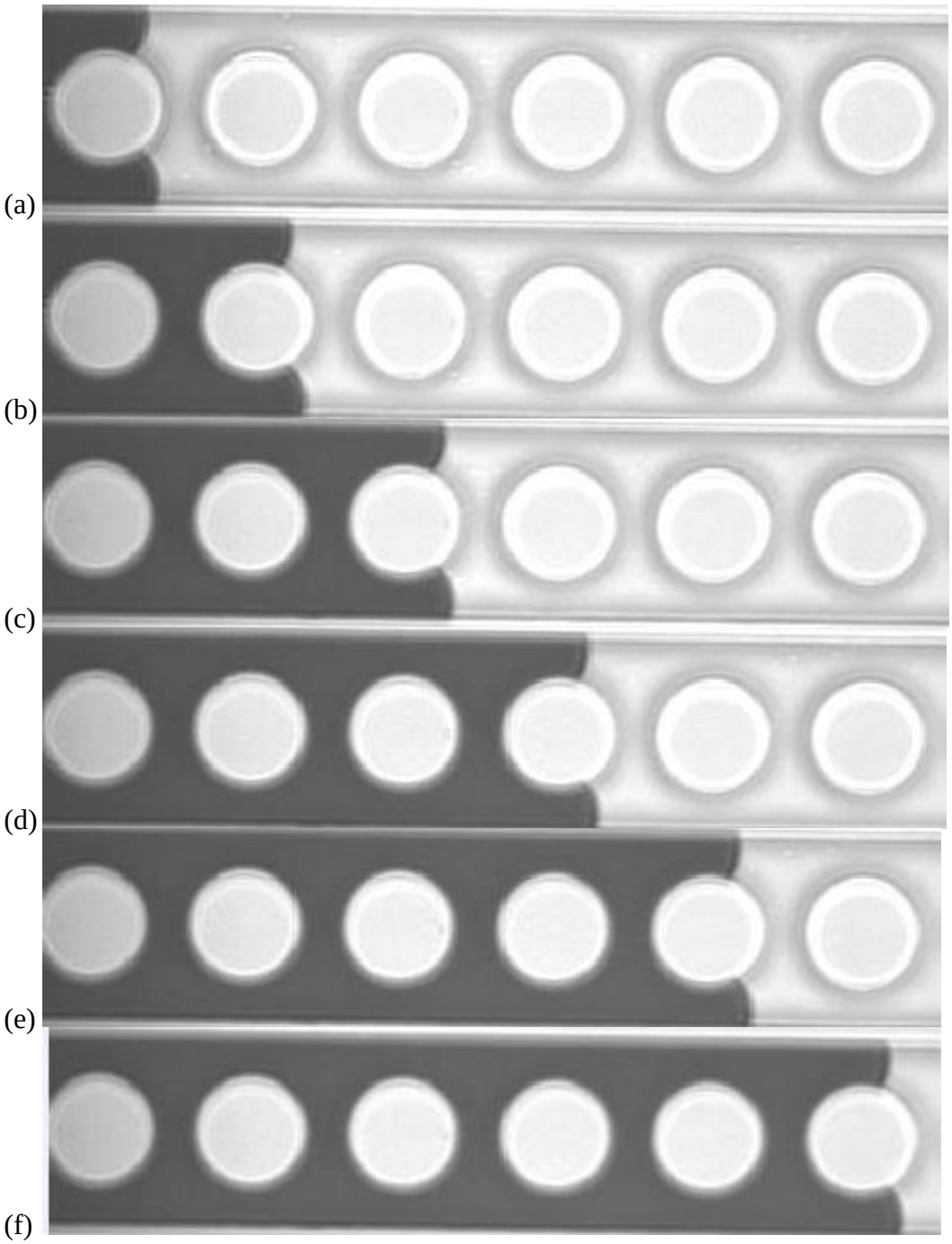

Figure 6.4 Flow images recorded for the circle obstacle in microfluidic chip (FC2, 1.0µl/min)
a t=236.8s **b** t= 239.76s **c** t= 242.76s **d** t= 245.66s **e** t=247.66 **f** t=250.67

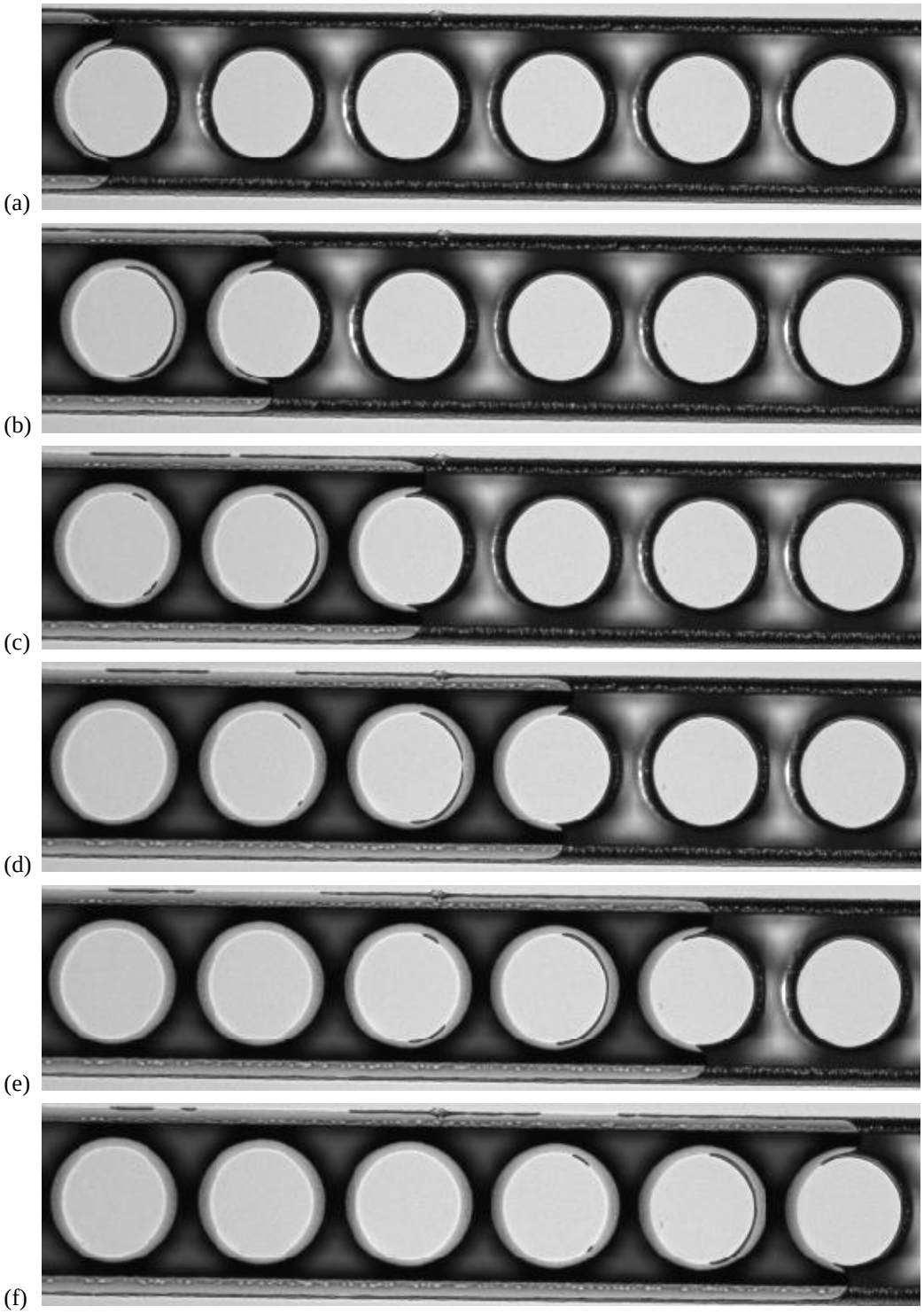

Figure 6.5 Consecutive flow images recorded for the circular obstacle (FC2) in 200µm microfluidic channel height with 1.0µl/min **a** t=1642.1s **b** t= 1649.9s **c** t= 1657.6s **d** t= 1665.3s **e** t=1672.9 **f** t=1680.5s

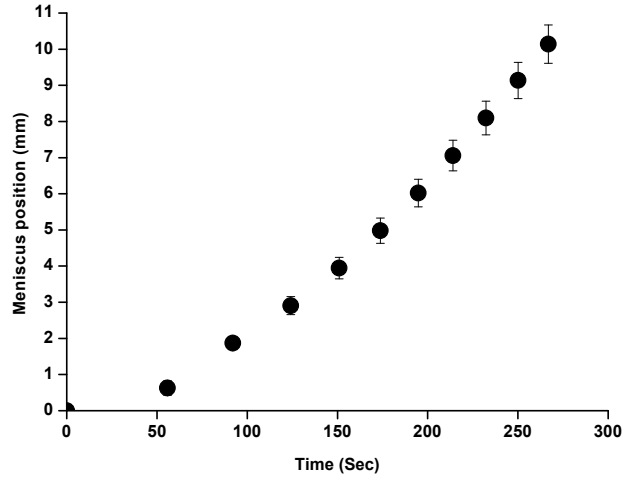

(a)

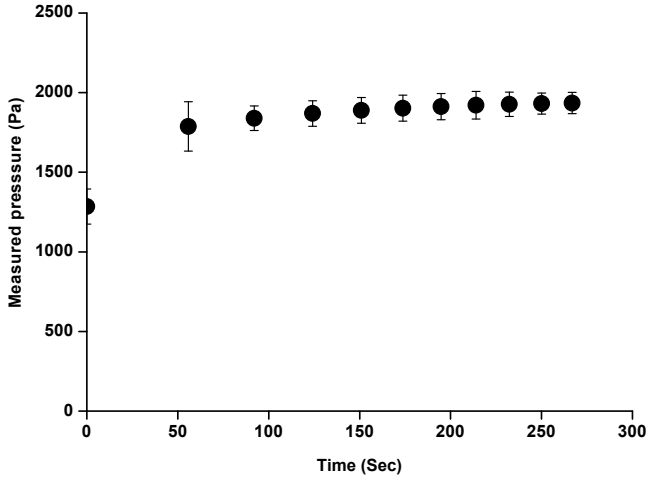

(b)

Figure 6.6 Flow results for 50μm channel depth with the largest characteristic lengths (i.e. minimum porosity: FC2) **a** developed meniscus position as a function of time at a flow rate 1.0μl/min **b** measured pressure for an imposed flow rate 1.0μl/min

Figures 6.7, 6.8 and 6.9 show the derived meniscus front velocities as well as the corresponding measured system pressures as a function of microchannel position for all obstacles (square, circles, hexagons and triangle) in 15μm deep microchannels for imposed flow rates of 1μl/min and 2μl/min. Data for channels with the largest obstacle characteristic lengths *(λ)* as defined previously, i.e. lowest mean porosity, are shown in Fig. 6.7 while data for channels with the middle and smallest obstacle characteristic lengths (intermediate and largest porosity levels) are given in Fig. 6.8 and Fig. 6.9, respectively. In each case, the measured flow velocity begins at a very low value, steadily increases as the flow stream moves through the channel, and then generally appears to approach a steady-state value as the fluid acceleration diminishes. As expected, the velocities measured at flow rates of 1μl/min were approximately half of those measured at flow rates of 2μl/min. Concurrent with each stream's increase in velocity was a corresponding increase in measured pressures. For both of the flow rates investigated, the measured pressure was recorded when the flow reached the first obstacle and then increased until an approximately constant slope *(ΔP/Δx)* was exhibited. The achievement of a roughly constant *ΔP/Δx* appeared to occur at about the same location as where the stream's velocity became constant.

Figures 6.10, 6.11 and 6.12 show the derived meniscus front velocities as well as the corresponding measured system pressures as a function of microchannel position for all three circular obstacles (FC2, FC3, and FC4) in 50μm, 100μm and 200μm deep microchannels for imposed flow rates of 1μl/min and 2μl/min. The transient microfluidic flow behavior seen in Figs. 6.10-6.12 was qualitatively similar to that observed in Figs.

6.7-6.9. However, as expected, the observed flow velocities and measured pressures decreased as the microchannel depth increased.

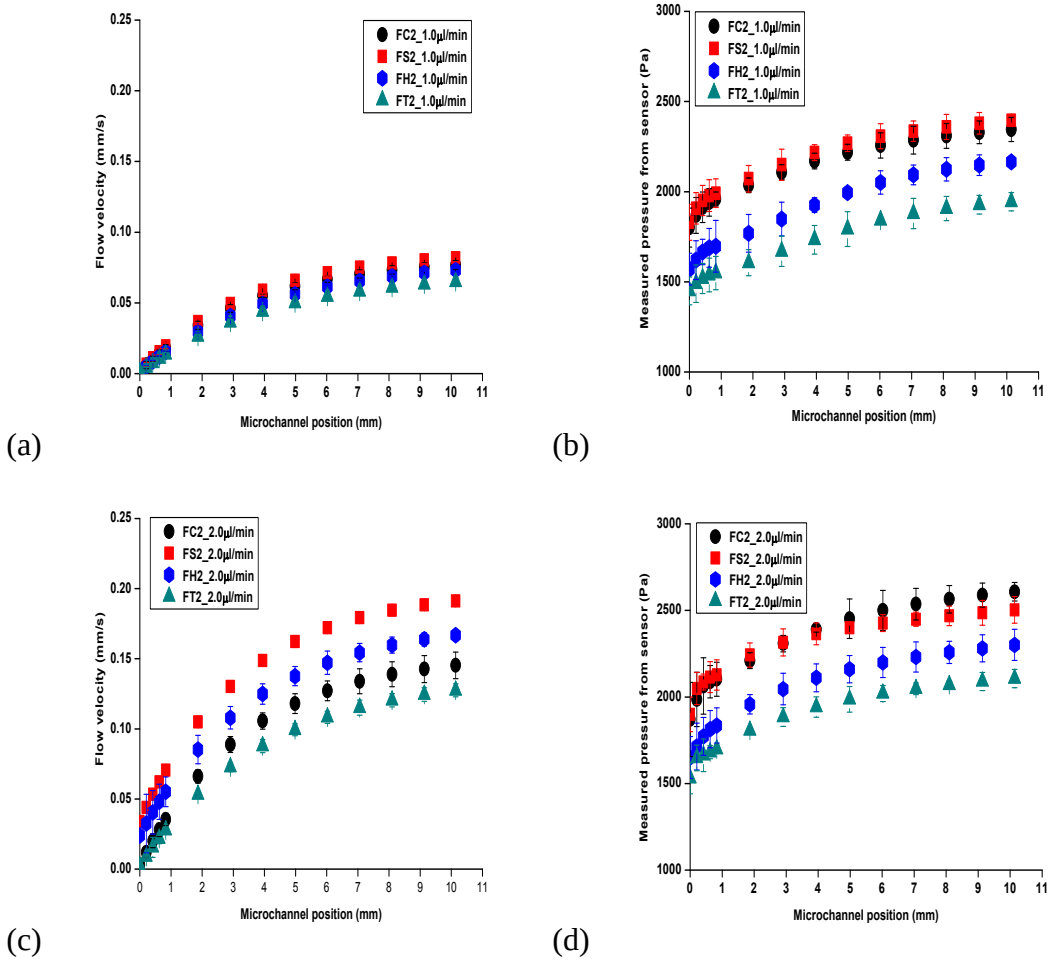

Figure 6.7 Flow results for various obstacles with the largest characteristic lengths (i.e., minimum porosity) in shallow (H=15µm) microfluidic channels **a** developed flow velocity as a function of position at 1.0µl/min and **b** developed pressure for an imposed flow rate of 1.0µl/min **c** developed flow velocity as a function of position at 2.0µl/min and **d** developed pressure for an imposed flow rate of 2.0µl/min

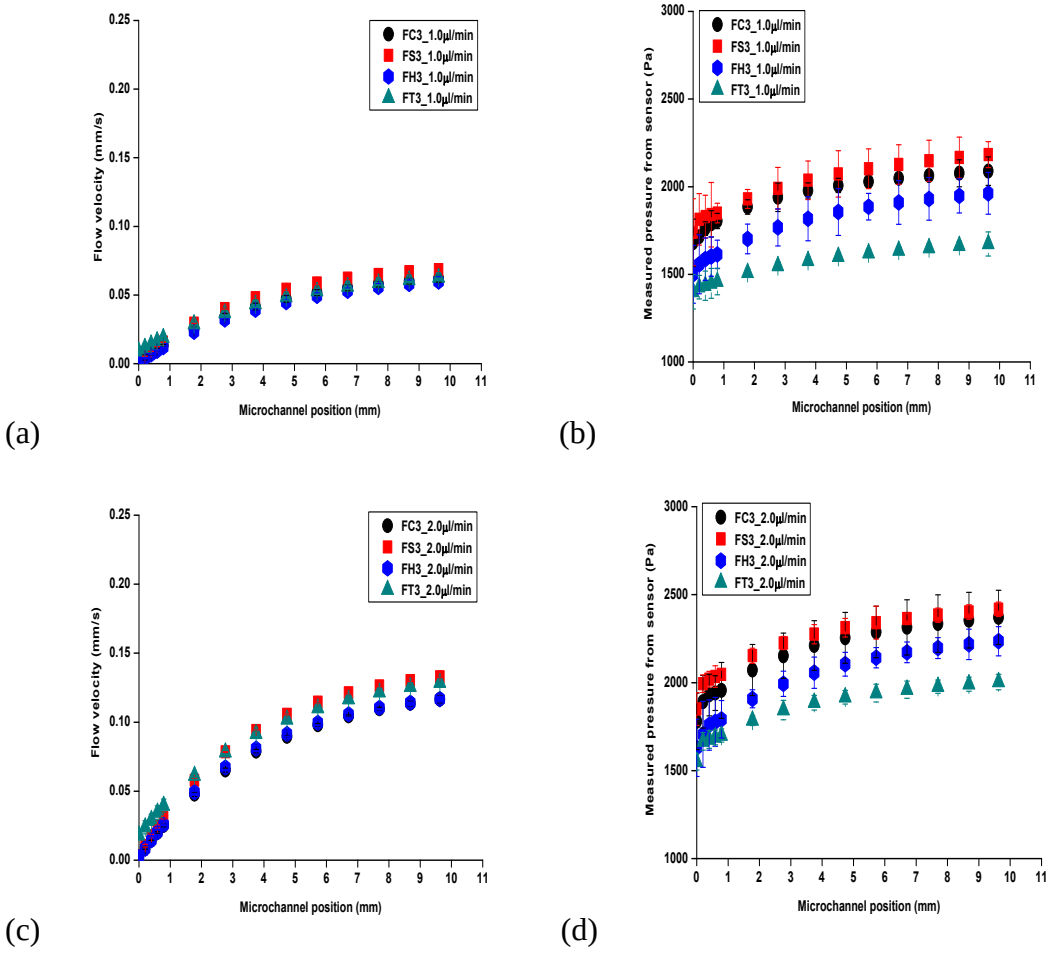

Figure 6.8 Flow results for various obstacles with the middle characteristic lengths (i.e., medium porosity) in shallow (H=15µm) microfluidic channels **a** developed flow velocity as a function of position at 1.0µl/min and **b** developed pressure for an imposed flow rate of 1.0µl/min **c** developed flow velocity as a function of position at 2.0µl/min and **d** developed pressure for an imposed flow rate of 2.0µl/min

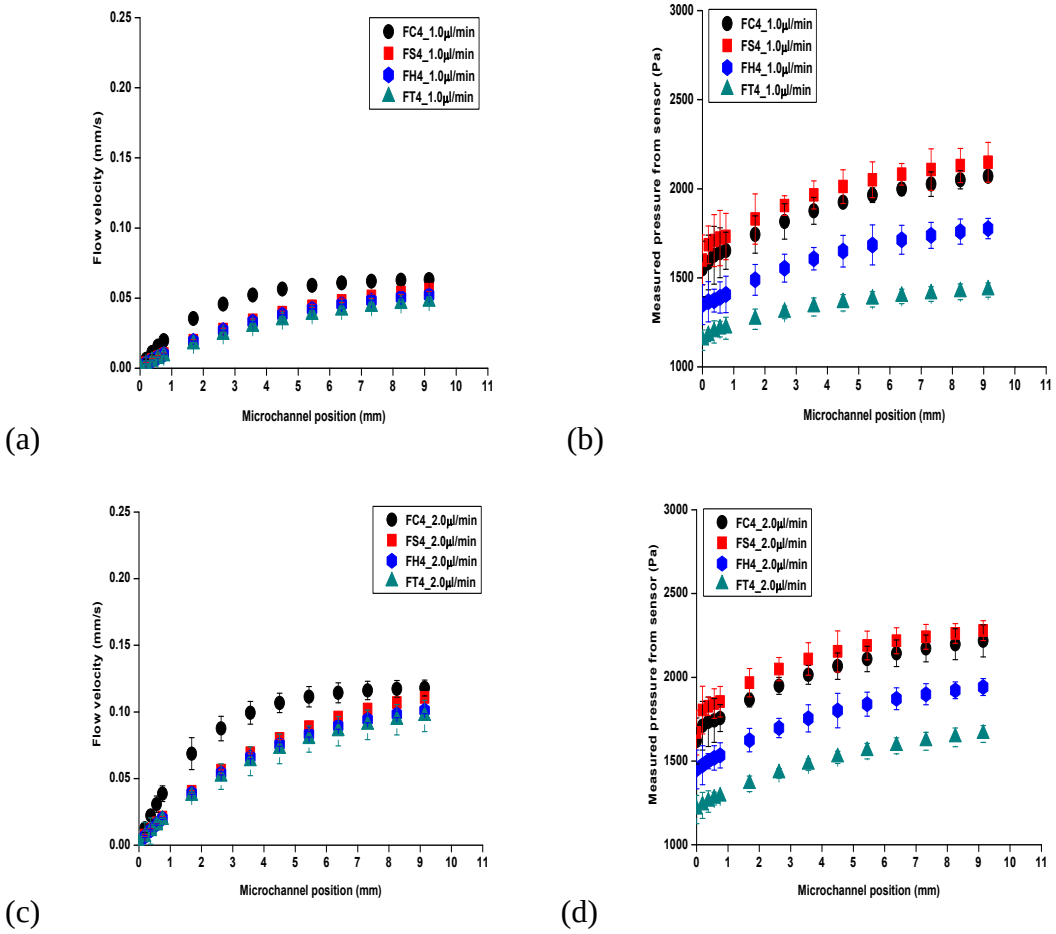

Figure 6.9 Flow results for various obstacles with the minimum characteristic lengths (i.e., largest porosity) in shallow (H=15µm) microfluidic channels **a** developed flow velocity as a function of position at 1.0µl/min and **b** developed pressure for an imposed flow rate of 1.0µl/min **c** developed flow velocity as a function of position at 2.0µl/min and **d** developed pressure for an imposed flow rate of 2.0µl/min

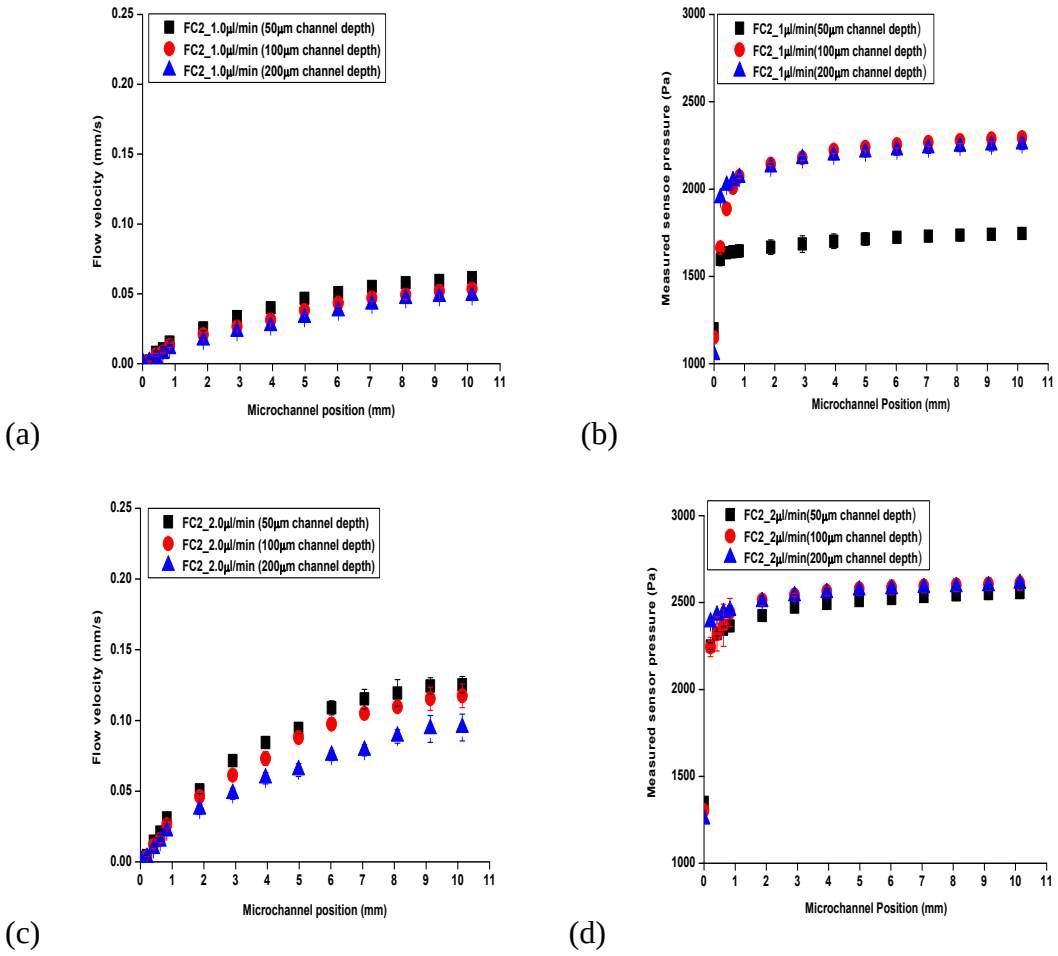

Figure 6.10 Flow results for various microfluidic channel depths with the largest characteristic lengths (i.e., minimum porosity) **a** developed flow velocity as a function of position at 1.0µl/min and **b** developed pressure for an imposed flow rate of 1.0µl/min. **c** developed flow velocity as a function of position at 2.0µl/min and **d** developed pressure for an imposed flow rate of 2.0µl/min

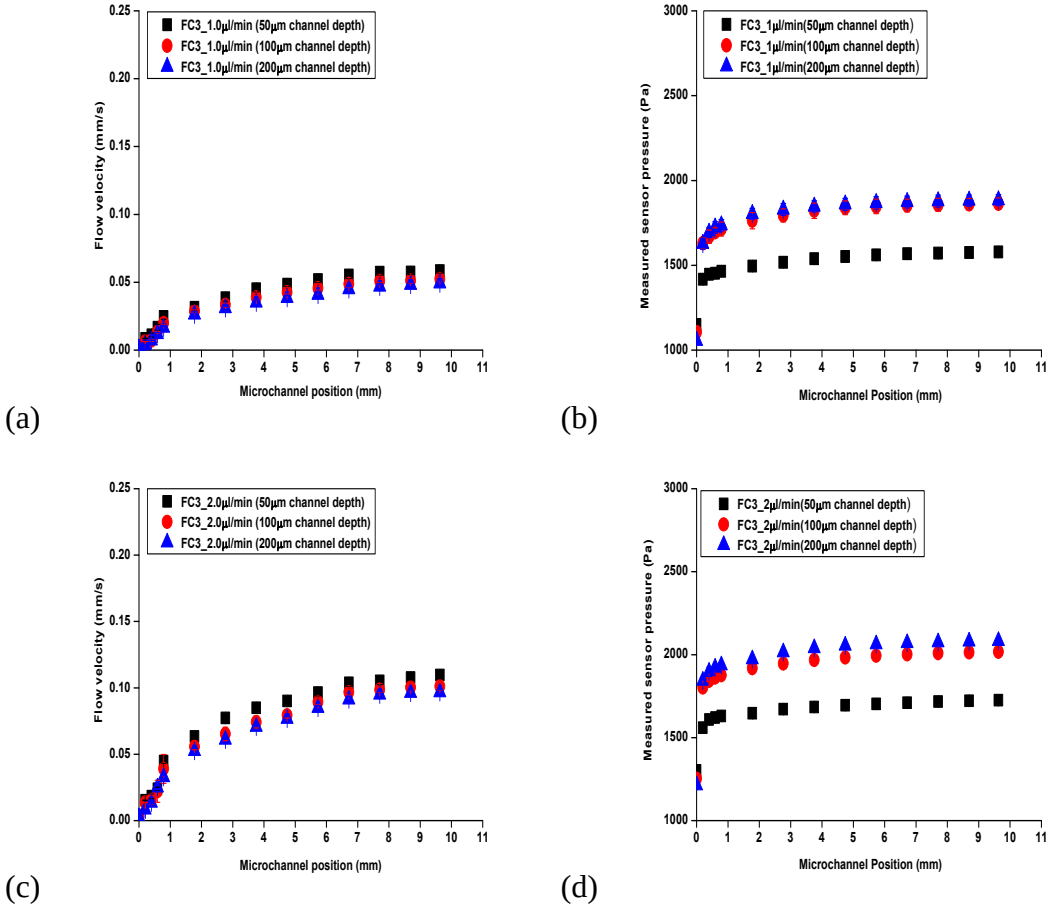

Figure 6.11 Flow results for various microfluidic channel depths with the middle characteristic lengths (i.e., medium porosity) **a** developed flow velocity as a function of position at 1.0µl/min and **b** developed pressure for an imposed flow rate of 1.0 µl/min. **c** developed flow velocity as a function of position at 2.0µl/min and **d** developed pressure for an imposed flow rate of 2.0µl/min

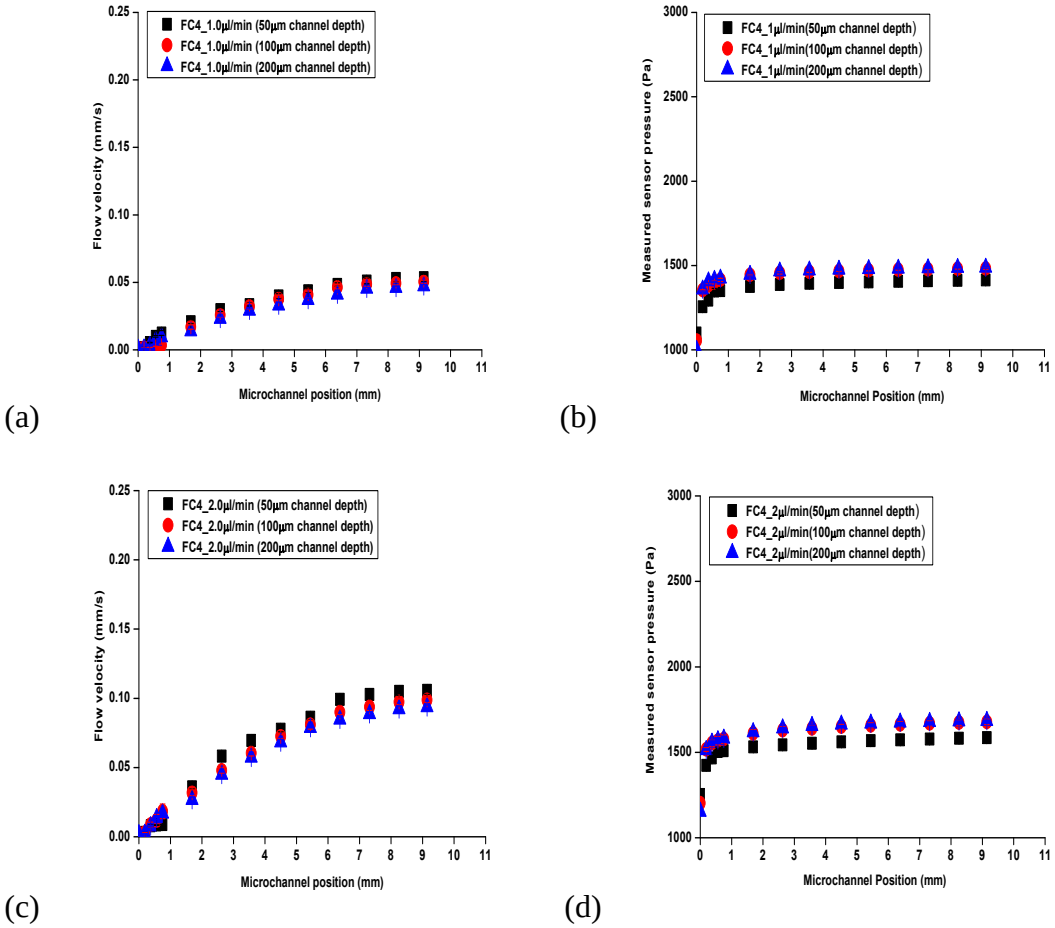

Figure 6.12 Flow results for various microfluidic channel depths with the minimum characteristic lengths (i.e., largest porosity) **a** developed flow velocity as a function of position at 1.0µl/min and **b** developed pressure for an imposed flow rate of 1.0µl/min. **c** developed flow velocity as a function of position at 2.0µl/min and **d** developed pressure for an imposed flow rate of 2.0µl/min

6.1.4 Estimation of quasi-steady state during start-up flows

The transient first-order system responses seen in measured velocity and pressure were explored more closely as follows. The transient increase in fluid velocity toward a quasi-steady constant value V_{QS} and the related decrease in $\Delta P/\Delta x$ from the large initial value to a much smaller and quasi-steady value $(\Delta P/\Delta x)_{QS}$ were examined by fitting exponential curves to the data sets using built-in fitting functions in Origin software (OriginLab, Northhampton, MA, USA). As noted in Chapter 5, a function of the transient flow velocity along the microchannel length x would be expected to be of the form of

$$V(x) = V_{QS}\left[1 - \exp(-\frac{x}{X_{DV}})\right] \tag{6.1}$$

The velocity decay constant X_{DV} exhibited by such a system is due to the combined effects of liquid inertia, viscous friction and other losses, meniscus capillarity and PDMS bulging. The associated pressure drop $\Delta P/\Delta x$ (where Δx is the slowly increasing length of the fluid-filled portion of the channel during start-up flow) driving the microfluidic flow was also analyzed as a simple first-order system. Although the measured system pressure increased as fluid filled the microfluidic channel, the pressure drop per unit length of fluid-filled channel $\left(\frac{\Delta P}{\Delta x}\right)$ asymptotically decreased towards a quasi-steady state value $\left(\frac{\Delta P}{\Delta x}\right)_{QS}$ as the fluid accelerated towards V_{QS}. Thus, a function of the transient pressure drop along with microfluidic channels would be anticipated to be of the form of

$$\frac{\frac{\Delta P}{\Delta x} - (\frac{\Delta P}{\Delta x})_{QS}}{(\frac{\Delta P}{\Delta x})_{initial} - (\frac{\Delta P}{\Delta x})_{QS}} = \exp\ (-\frac{x}{X_{DP}}) \tag{6.2}$$

The first-order system decay constant associated with the pressure X_{DP} in such a system is, as before, due to the combined effects of liquid inertia, viscous friction and other losses, meniscus capillarity and PDMS bulging. The transient increase in fluid velocity toward a quasi-steady constant value V_{QS} and the related decrease in $\Delta P/\Delta x$ from the large initial value to a much smaller and quasi-steady value $(\Delta P/\Delta x)_{QS}$ were examined by fitting exponential curves to the derived velocity vs. position data and the pressure vs. position data sets as shown in the examples of Figs. 6.13 a and b, respectively. A function of the form with respect to V_{QS} shown in Eq. (6.1) was fit to the velocity data of Fig. 6.13a, while a function of the form with respect to $(\Delta P/\Delta x)_{QS}$ shown in Eq. (6.2) was fit to the $\Delta P/\Delta x$ data of Fig. 6.13b. An example of the results of these curve fits is shown in Fig. 6.13. Transients during start-up over the initial 2mm of the microchannel lengths created relatively large errors and uncertainties and thus the curve fits utilized data from the 2mm position to the end of each microchannel. Eq. (6.1) was curve fit to the derived velocity data of the experimental results shown in previously in Figs. 6.7-6.12. The results of the velocity curve fits for shallow (H=15μm) and deep (H=50-200μm) microchannels are shown in Tables 6.3 and 6.4, respectively. In addition, the relationship of the mean velocities as a function of the mean bulging-modified hydraulic diameter is shown in Fig. 6.14a. The curve fits showed excellent correlation coefficients (R^2) with most fits exhibiting R^2 values of 0.98 or 0.99. The mean experimental velocities for an imposed flow rate of 2μl/min flow rate were compared to the mean velocities for the

1μl/min flow rate by taking the simple ratio of the two. A perfectly accurate and precise syringe pump delivering fluid to a perfectly rigid microchannel system should yield $\frac{V_{QS}\ (2\mu l\ /\ \min)}{V_{QS}\ (1\mu l\ /\ \min)} = 2$. The ratio of $\frac{V_{QS}\ (2\mu l\ /\ \min)}{V_{QS}\ (1\mu l\ /\ \min)}$ versus the mean bulging-modified hydraulic diameter is shown in Fig. 6.14b. The mean experimental ratio of the velocities for the shallow microchannels (H=15μm) was found to be 1.92, 4% less than expected. The mean experimental ratio of the velocities for the H=50μm microchannels was found to be 1.92, the same as found for the H=15mm microchannels. However, the mean velocity ratios for the H=100μm and H=200μm microchannels were found to be 1.96 and 1.97, respectively. Since the flow rates maintained by the syringe pump were accurate to $\pm$0.5%, the lower than expected velocity ratios are primarily attributable to a lack of rigidity of the PDMS microchannels. This conclusion is consistent with the shallowest microchannels exhibiting the largest deviation and the deepest microchannels exhibiting the least deviation.

Eq. (6.2) was curve fit to the derived pressure drop data of the experimental results shown in previously in Figs. 6.7-6.12. The results of the pressure drop curve fits for shallow (H=15μm) and deep (H=50-200μm) microchannels are shown in Tables 6.5 and 6.6, respectively. As before, the curve fits showed excellent correlation coefficients (R^2) with most fits exhibiting R^2 values of 0.98 or 0.99. The relationship of the mean pressure drop as a function of the mean bulging-modified hydraulic diameter is shown in Fig. 6.15a. As expected, the mean pressure drops decrease as the bulging-modified hydraulic diameters increase. The mean experimental pressure drops for an imposed flow rate of 2μl/min flow rate were also compared to the mean pressure drops for the 1μl/min

flow rate by again taking simple ratios of the two values of pressure drop. According to the Hagen-Poiseuille relationship, a perfectly rigid microchannel system should yield $\frac{(\Delta P / \Delta x)_{QS}\ (2\mu l / \min)}{(\Delta P / \Delta x)_{QS}\ (1\mu l / \min)} = 2$. The ratio of $\frac{(\Delta P / \Delta x)_{QS}\ (2\mu l / \min)}{(\Delta P / \Delta x)_{QS}\ (1\mu l / \min)}$ versus the mean bulging-modified hydraulic diameter is shown in Fig. 6.15b. The pressure drop ratio steadily increases towards the limit of 2 as the the mean bulging-modified hydraulic diameter increases for these microchannels. The mean experimental ratio of $(\Delta P/\Delta x)_{QS}$ for the shallow microchannels (H=15μm) was found to be 1.23, 38% less than expected. The mean experimental ratio of $(\Delta P/\Delta x)_{QS}$ for the H=50μm microchannels was found to be 1.71, 14% less than expected. The mean experimental ratio of $(\Delta P/\Delta x)_{QS}$ for the H=100μm microchannels was found to be 1.83, 8% less than expected while the ratio of $(\Delta P/\Delta x)_{QS}$ for the H=200μm microchannels was found to be 1.87, or only 6% less than expected. Bulging deformation of the PDMS microchannels exerted a much more significant effect on the measured pressure drops than on the measured velocities, especially for the more shallow microchannels. The microchannles with the greatest depth (H=200μm) exhibited the least bulging effects. It is also interesting to note that for three of the specific obstacle geometries (FC, FH, FT), the measured pressure drops consistently increased as the obstacle-to-wall gaps increased (e.g., FC2→FC3→FC4). This observation is consistent with the smallest porosity microchannels exhibiting the largest deviation and the microchannels with the greatest porosity exhibiting the least deviation.

The decay constants for the curve fits of Eq. (6.1) and Eq. (6.2) are shown in Table 6.7 and 6.8 for the shallow (H=15μm) microchannels and the deep (H=50, 100,

200μm) microchannels, respectively. No significant differences are seen in the values of X_{DV} for the various depths and obstacles investigated. In addition, no significant differences are seen in the values of X_{DP} for the various depths and obstacles investigated. However, the mean value of X_{DV} was 57% larger than the mean value of X_{DP} for all obstacles, microchannel depths and flow rates investigated. Thus the velocity response of the system was significantly slower than the pressure response after the liquid front began encountering the obstacles in the microchannels. This result appears reasonable but requires additional work to more quantitatively evaluate the implications.

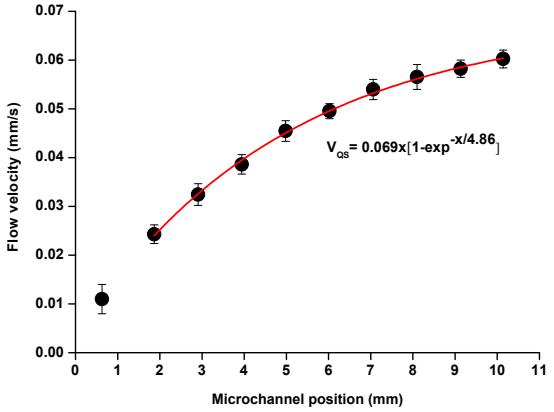

(a)

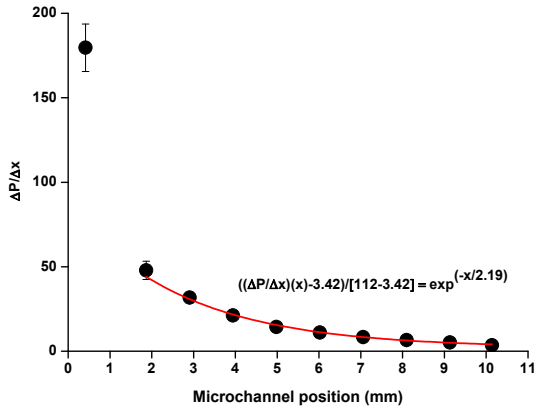

(b)

Figure 6.13 Analysis of transient flow velocity and pressure data for FC2 50μm channel depth at a flow rate 1.0μl/min

Table 6.3 Quasi-steady state flow velocity (V_{QS}) for shallow (H=15μm) microfluidic channels

Structure	1μl/min		2μl/min		V_{QS} Ratio
	V_{QS} (mm/s)	R^2	V_{QS} (mm/s)	R^2	
FC2	0.080	0.988	0.150	0.988	1.87
FC3	0.067	0.974	0.125	0.937	1.87
FC4	0.063	0.988	0.117	0.998	1.86
FH2	0.079	0.980	0.152	0.987	1.92
FH3	0.066	0.989	0.124	0.993	1.88
FH4	0.059	0.993	0.112	0.995	1.90
FS2	0.085	0.971	0.165	0.988	1.94
FS3	0.072	0.992	0.139	0.992	1.93
FS4	0.066	0.996	0.127	0.986	1.92
FT2	0.070	0.974	0.136	0.971	1.94
FT3	0.061	0.988	0.122	0.970	2.00
FT4	0.055	0.937	0.108	0.997	1.96

Table 6.4 Analysis of quasi-steady state flow velocity (V_{QS}) for deep (H=50-200μm) microfluidic channels

Structure & Depth	1μl/min		2μl/min		V_{QS} Ratio
	V_{QS} (mm/s)	R^2	V_{QS} (mm/s)	R^2	
FC2_50μm	0.069	0.998	0.136	0.973	1.97
FC2_100μm	0.067	0.994	0.133	0.987	1.98
FC2_200μm	0.065	0.997	0.129	0.998	1.98
FC3_50μm	0.061	0.960	0.115	0.976	1.89
FC3_100μm	0.058	0.996	0.112	0.987	1.93
FC3_200μm	0.056	0.982	0.109	0.988	1.95
FC4_50μm	0.061	0.987	0.116	0.972	1.90
FC4_100μm	0.056	0.974	0.111	0.988	1.98
FC4_200μm	0.054	0.985	0.107	0.986	1.98

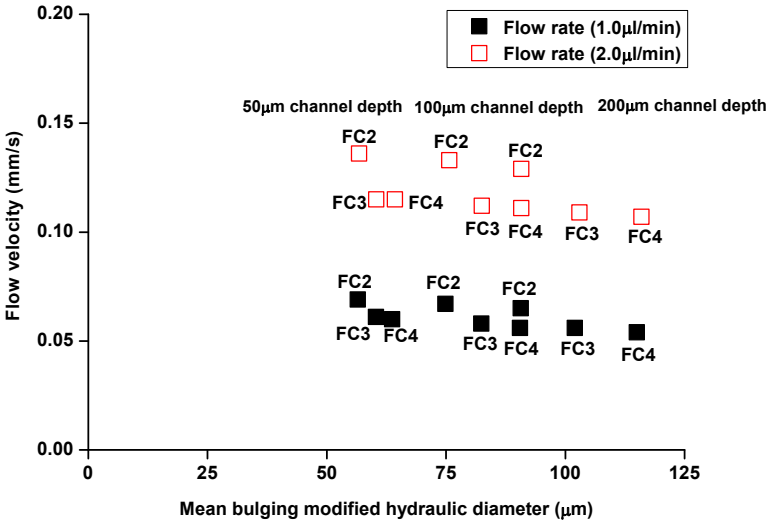

(a)

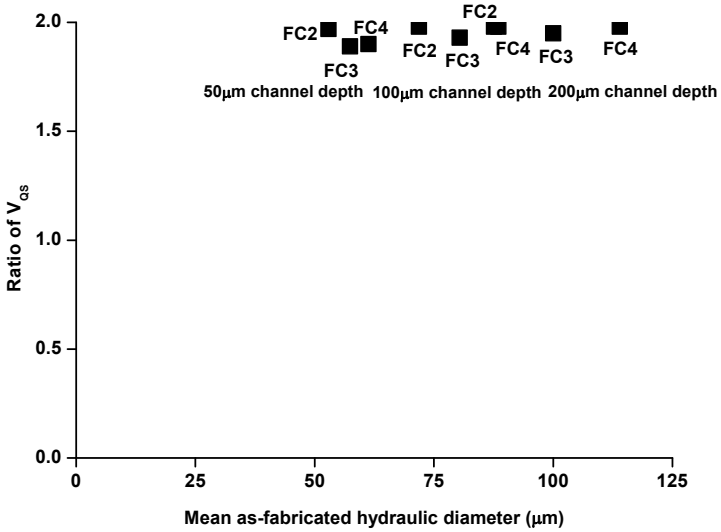

(b)

Figure 6.14 a Quasi-steady flow velocity V_{QS} vs. mean bulging modified hydraulic diameters **b** Analysis of ratio of V_{QS} vs. mean as-fabricated hydraulic diameters

Table 6.5 Quasi-steady pressure drop/unit length $(\Delta P/\Delta x)_{QS}$ in shallow (H=15μm) microfluidic channels

	Pressure drop/Length $(\Delta P/\Delta x)_{QS}$ (Pa/mm)				
Structure	1μl/min	R^2	2μl/min	R^2	$(\Delta P/\Delta x)_{QS}$ Ratio
FC2	11.5	0.977	13.9	0.958	1.20
FC3	11.0	0.966	13.3	0.975	1.21
FC4	10.7	0.946	13.0	0.978	1.22
FH2	10.9	0.998	13.5	0.978	1.24
FH3	10.1	0.988	13.0	0.988	1.29
FH4	9.20	0.998	12.6	0.985	1.37
FS2	14.1	0.984	15.2	0.997	1.08
FS3	13.5	0.984	14.4	0.994	1.07
FS4	12.4	0.979	14.0	0.983	1.13
FT2	9.49	0.963	12.0	0.982	1.27
FT3	8.27	0.977	11.0	0.986	1.33
FT4	7.34	0.996	10.3	0.955	1.40

Table 6.6 Analysis of quasi-steady pressure drop along with deep (H=50-200μm) microfluidic channels

	Pressure drop/Length $(\Delta P/\Delta x)_{QS}$ (Pa/mm)				
Structure	1μl/min	R^2	2μl/min	R^2	V_{QS} Ratio
FC2_50μm	3.42	0.998	5.46	0.988	1.60
FC2_100μm	2.33	0.983	4.15	0.989	1.78
FC2_200μm	1.94	0.984	3.47	0.991	1.79
FC3_50μm	2.95	0.991	4.90	0.997	1.66
FC3_100μm	2.21	0.998	4.00	0.997	1.81
FC3_200μm	1.29	0.935	2.38	0.995	1.84
FC4_50μm	2.49	0.991	4.62	0.966	1.86
FC4_100μm	1.34	0.998	2.53	0.998	1.89
FC4_200μm	0.85	0.965	1.68	0.995	1.98

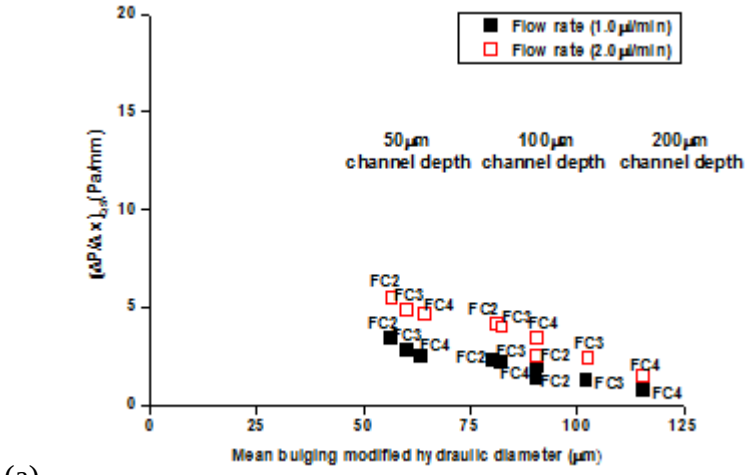

(a)

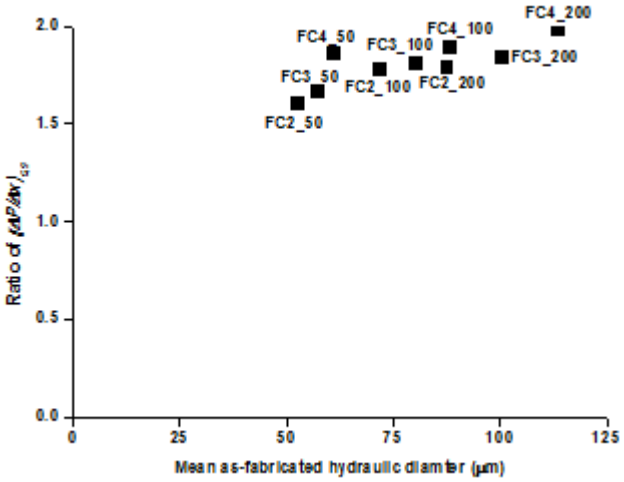

(b)

Figure 6.15 a Quasi-steady pressure drop/microfluidic channel length ($(\Delta P/\Delta x)_{QS}$ vs. mean modified hydraulic diameters **b** analysis of ratio of $(\Delta P/\Delta x)_{QS}$ vs. mean as-fabricated hydraulic diameters

Table 6.7 Decay constants in shallow (H=15μm) microfluidic channels

	Flow Velocity V_{QS}		Pressure drop/Length $(\Delta P/\Delta x)_{QS}$	
Structure	1μl/min	2μl/min	1μl/min	2μl/min
FC2	3.56	3.43	2.16	2.09
FC3	4.86	4.25	2.19	2.42
FC4	5.57	4.50	3.78	3.22
FH2	4.19	3.62	2.72	2.67
FH3	4.33	3.71	2.92	2.73
FH4	4.5	4.17	3.67	3.42
FS2	3.52	3.32	2.20	1.90
FS3	3.6	3.53	2.74	2.11
FS4	5.16	4.78	3.16	2.49
FT2	4.15	3.96	2.79	2.25
FT3	4.53	4.06	2.98	2.27
FT4	4.76	4.22	3.05	4.22

Table 6.8 Decay constants in deep (H=50-200μm) microfluidic channels

	Flow Velocity V_{QS}		Pressure drop/Length $(\Delta P/\Delta x)_{QS}$	
Structure	1μl/min	2μl/min	1μl/min	2μl/min
FC2_50μm	4.86	4.25	2.19	2.42
FC2_100μm	5.57	4.90	3.78	3.22
FC2_200μm	6.01	5.58	4.54	3.66
FC3_50μm	4.08	3.97	2.81	2.59
FC3_100μm	4.19	4.06	2.87	2.60
FC3_200μm	4.33	4.15	2.98	2.65
FC4_50μm	2.37	2.15	2.04	1.25
FC4_100μm	2.94	2.46	2.10	1.51
FC4_200μm	3.15	3.04	2.47	1.85

6.1.5 Analysis of friction coefficients during quasi-steady state flows

Figure 6.15a shows that increasing the mean as-fabricated hydraulic diameter of the microfluidic channels investigated here generally decreases the measured values of $(\Delta P/\Delta x)_{QS}$. Of more fundamental importance is the experimental dependence of viscous friction effects on the Reynolds number of the flow. The experimental Reynolds number for each flow condition was calculated using the mean bulging-modified hydraulic diameter $\overline{D}_H$ from Tables 6.1 and 6.2 and the mean quasi-steady fluid velocity $\overline{V}_{QS}$ predicted by the exponential curve fits as summarized in Tables 6.3 and 6.4. Thus

$$\mathrm{Re} = \frac{\rho \overline{V}_{QS} \overline{D}_H}{\mu} \tag{6.3}$$

The Darcy friction factors f for the obstacle-laden microchannels were calculated from the mean bulging-modified hydraulic diameters $\overline{D}_H$, quasi-steady pressure drop data from Tables 6.5 and 6.6, and quasi-steady velocity data (Tables 6.3 and 6.4) according to

$$f = \left(\frac{\Delta P}{\Delta x}\right)_{QS} \frac{\overline{D}_H}{\frac{\rho \overline{V}^2_{QS}}{2}} \tag{6.4}$$

The experimental dependence of f on Re is depicted in Fig. 6.16a for the shallow (H=15μm) microfluidic channels and in Fig. 6.16b for the deep channels (H=50, 100, 200μm) with all types of obstacles at both imposed flow rates (1 and 2μl/min). The theoretical relationship of $f \propto Re^{-1}$ is also shown for reference. Fig. 6.17 shows the experimental dependence of f on Re for just the circular obstacles (FC2, FC3, FC4) for the various depths of microfluidic channels (H=15, 50, 100, 200μm) at both imposed flow rates. The theoretical relationship of $f \propto Re^{-1}$ is again shown for reference. Figure

6.17 shows a significant difference between the viscous friction behavior of the shallow and the deep microchannels. The shallowest channels with H=15μm display a much greater dependence of *f* on *Re* than expected from theoretical considerations. The behavior of the deeper microchannels is much closer to the theoretical expectation with exponents of -1.10 to -1.12.

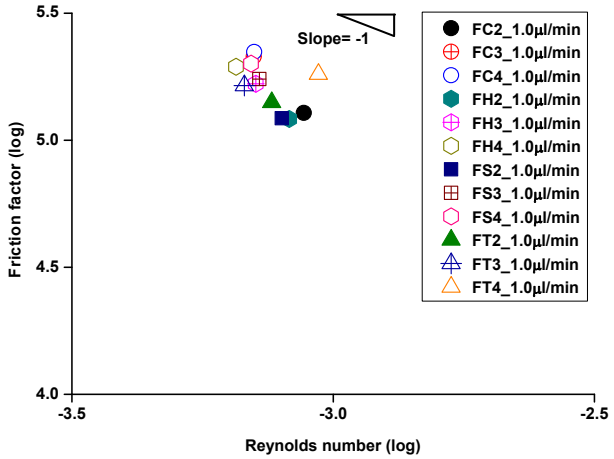

(a)

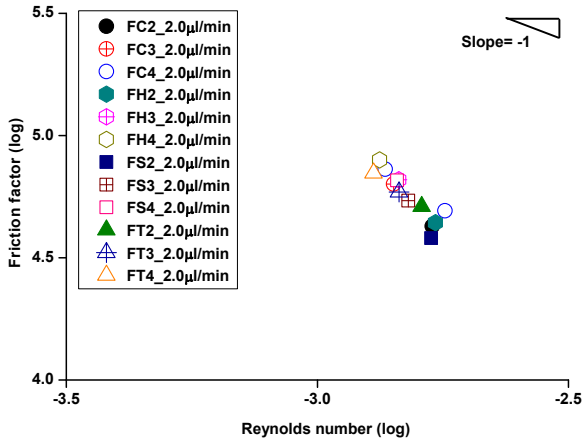

(b)

Figure 6.16 Friction factor (*f*) as a function of Reynolds number (*Re*) for shallow microfluidic channels **a** flow rate: 1.0μl/min and **b** flow rate: 2.0μl/min
Note: The vertical and horizontal scales (log *f*-log *Re*) from this figure are different and the slope of a line representing Re^{-1} dependence is not at 45 degrees.

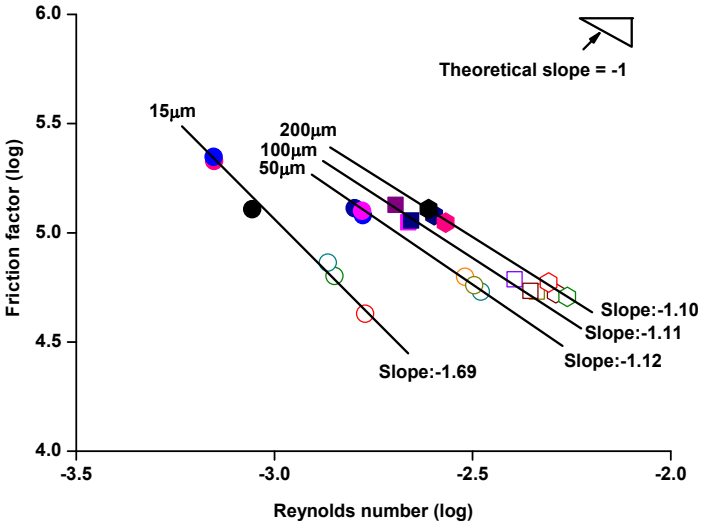

Figure 6.17 Friction factor (*f*) as function of Reynolds number (*Re*) for four different microfluidic channels with circular embedded obstacles
Note: The vertical and horizontal scales (log *f*-log *Re*) from this figure are different and the slope of a line representing Re^{-1} dependence is not at 45 degrees.

The experimental friction factor data shown in Figs. 6.16 and 6.17 are shown in Fig. 6.18 along with additional data from the literature covering a range of Reynolds numbers that spans almost 8 orders of magnitude. The new data set from the present investigation provides a significant new contribution to the literature data at very low values of Reynolds number (10^{-4} - 10^{-3}). Figure 6.18 also shows the minimum (*f=56.9/Re*) and maximum (*f=96/Re*) theoretical values of Darcy friction factor for typical rectangular microfluidic channels. The Darcy friction factor results from the present study show that the relative trend values agree well with the theoretically expected values at the very low Reynolds numbers investigated here.

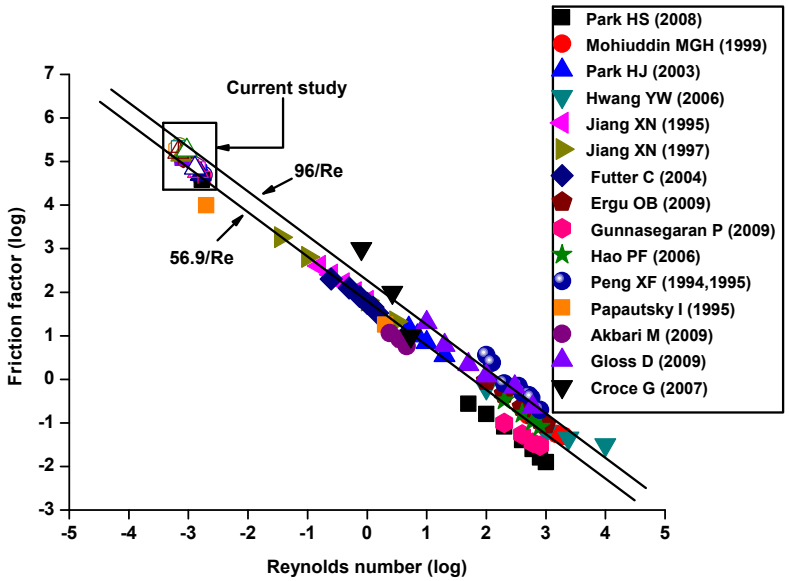

(a)

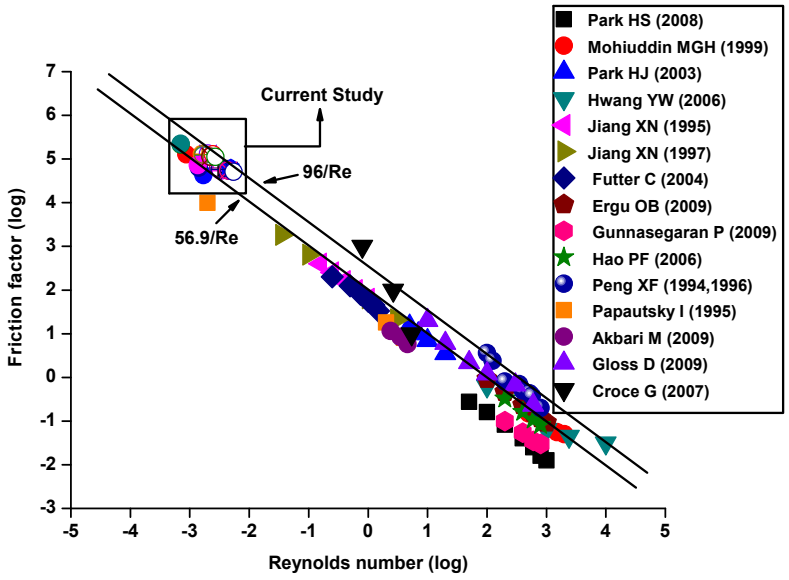

(b)

Figure 6.18 The results of the present investigation of the friction factor (*f*) at very low values of Reynolds number (*Re*) for channels with obstacles compared to a wide range of literature data for open microfluidic channels as well as the range of expected values for rectangular microchannels (56.9/*Re* to 96/*Re*) **a** shallow microfluidic channels (H=15μm) **b** deep microfluidic channels (H=50, 100, and 200μm)
Note: The vertical and horizontal scales (log *f*-log *Re*) from this figure are different and the slope of a line representing Re^{-1} dependence is not at 45 degrees.

The fractional uncertainties in friction factor were calculated from Eq. (4.8) and the results are listed in Table 6.9 for shallow microfluidic channels and Table 6.10 for deep microfluidic channels. Similar calculations of the uncertainty in Reynolds numbers for the experiments are also shown in Tables 6.9 and 6.10. The largest contributor to uncertainty in the present experiments is the uncertainty in the mean velocity of the liquid through the microfluidic channel. Note that the microchannel fluid velocities in this investigation were experimentally evaluated from time-based measurements of the actual position of the fluid front and were not simply derived from the volumetric flow rates utilized.

The experimental uncertainty in the bulging was related to the height measurement. The method of fluorescence intensity difference has been used for the standard bulging measuring techniques. However, experience has shown that very small displacements (>2μm) do not well defined at very low flow rates. It is usually because of unresolved fringes from the center to the edge of PDMS microchannels. The total height of the bulge was considered in this study and expressed as the sum of the bulging during the experiment. Shallow microchannels, occurred large bulging, showed large differences (~5%) with using Imaris 7.2.3 image analysis software (Bitplane Inc., South Windsor, CT) while the difference became smaller in deep microchannels (~3%).

Table 6.9 Analysis of the fractional uncertainty in the friction factor and Reynolds number for shallow (H=15μm) microfluidic channels

	Fractional uncertainty (%) in Reynolds number		Fractional uncertainty (%) in friction factor	
	1.0μl/min	2.0μl/min	1.0μl/min	2.0μl/min
FC2	6.82	4.72	9.48	7.11
FC3	6.91	4.98	10.19	7.73
FC4	7.20	4.76	11.77	6.38
FH2	8.99	5.16	8.94	9.26
FH3	8.17	4.30	11.19	7.39
FH4	6.31	4.69	8.19	6.40
FS2	8.45	5.52	8.81	8.58
FS3	6.14	4.79	9.20	9.62
FS4	6.40	4.85	7.78	8.26
FT2	6.99	4.88	10.76	8.99
FT3	7.99	4.62	10.40	6.87
FT4	6.03	4.64	7.23	10.45

Table 6.10 Analysis of the fractional uncertainty in the friction factor and Reynolds number for deep (H=50-200μm) microfluidic channels

	Fractional uncertainty (%) in Reynolds number		Fractional uncertainty (%) in friction factor	
	1.0μl/min	2.0μl/min	1.0μl/min	2.0μl/min
FC2_50μm	5.85	5.06	5.49	7.29
FC2_100μm	6.30	5.31	7.22	7.82
FC2_200μm	6.95	6.22	9.25	10.19
FC3_50μm	6.31	6.80	7.11	11.54
FC3_100μm	7.55	7.22	10.82	12.38
FC3_200μm	7.53	7.41	10.77	12.80
FC4_50μm	6.48	6.11	8.45	10.53
FC4_100μm	7.13	5.44	10.26	8.94
FC4_200μm	7.65	6.09	12.17	11.02

6.2 PDMS material studies

As noted previously PDMS is commonly used in the process of soft lithography and PDMS-based microfluidic channels continue to be a popular choice among researchers due to the ease of fabrication. However, many researchers that utilize PDMS materials do not report the elastic property changes that their systems might be experiencing under pressure-driven conditions. In this section, a detailed investigation is reported of the deformation of PDMS microfluidic channels containing periodically spaced circle obstacles. As noted previously, fluorescence intensity measurements were used to quantify channel deformation using the linear relationship between dye layer thickness and fluorescent intensity. The primary experimental variables of interest were PDMS

wall thicknesses, PDMS mixing ratios as well as the applied flow rates and resultant system pressures. Two different analyses were also employed to better understand the experimental behavior: finite element analysis (FEM) using ANSYS Workbench 13.0 and a scaling analysis reported by Gervais et al. (2006).

6.2.1 Effects of mixing ratio on PDMS elastic modulus

The mechanical properties of PDMS are dependent upon the amount of cross-linking agent (resin:hardener or elastomer base:crosslinker mixing ratio), UV exposure time, curing temperature and time. In this study, tensile tests were performed on the preparation of various mixing ratios (5:1, 10:1, 15:1) and two PDMS tensile sample thicknesses (3mm and 6mm) to characterize the mechanical properties. The effects of mixing ratio on elastic modulus are shown in Fig. 6.19. As expected, decreasing the ratio of resin:hardener from a 10:1 ratio to a 5:1 ratio increased the elastic modulus by slightly more than 50%. Increasing the ratio of resin:hardener from a 10:1 ratio to a 15:1 ratio further decreased the elastic modulus by approximately 50%. Figure 6.19 also indicates that the elastic modulus of PDMS slightly increased with increasing wall thickness from 3mm to 6 mm thickness.

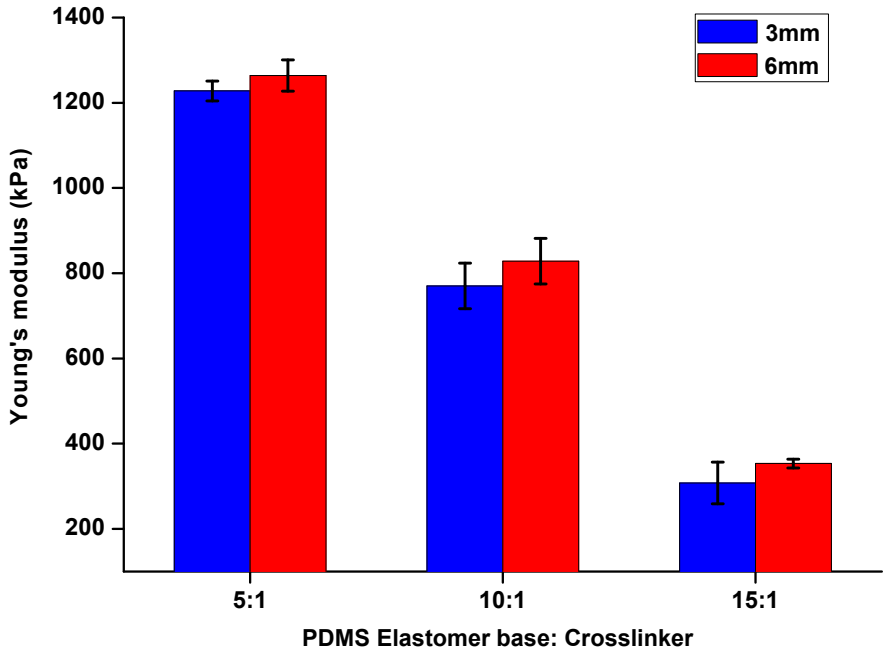

Figure 6.19 Experimental characterization of Young's modulus

6.2.2 Effects of mixing ratio on measured system pressures

As noted in Section 6.1.1, perfectly rigid microfluidic channels exhibit a linear relationship between the imposed flows and the pressure drop developed along the channel, consistent with the Hagen-Poiseuille relationship (Eq. 1.6). Fig. 6.2 showed significant non-linear behavior for the 50 μm deep microchannels while the 200 μm deep microchannels exhibited almost linear behavior. A 10:1 mixing ratio was used for the channels reported in Fig. 6.2. The variations of pressure drop developed across a range of imposed flow rates was investigated for three different PDMS mixing ratios for microfluidic channels with H=50μm and circular obstacles (FC2). These results are shown in Fig. 6.20. Decreasing the mixing ratio from 15:1 to 10:1 to 5:1 appears to

increase the stiffness of the 50μm deep microchannels and yield more linear behavior, at least for the 0-2 μl/min flow rate range.

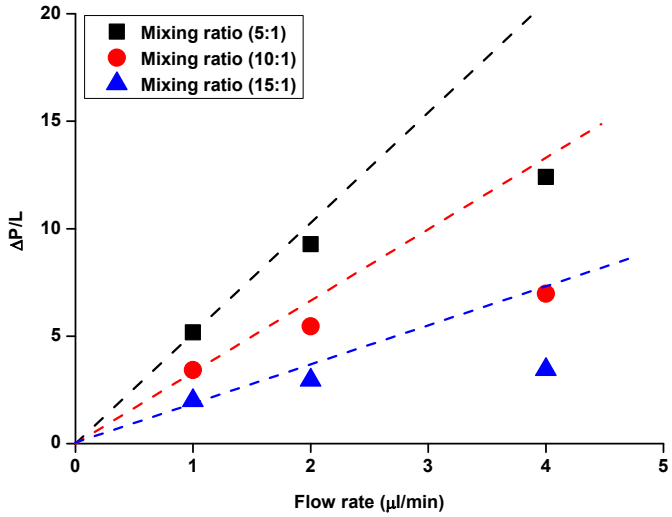

Figure 6.20 Experimentally determined relationship between pressure drop along with channel length and imposed flow rates

The effect of mixing ratio was examined again by characterizing the measured system pressure as a function of meniscus position for a 50μm deep microchannel in a PDMS chip with a wall thickness of 6mm and an imposed flow rate of 1.0μl/min. These data are presented in Fig. 6.21a. In addition, the measured system pressure as a function of meniscus position for a 50μm deep microchannel in a PDMS chip (5:1 mixing ratio) with wall thicknesses of 3 and 6mm and imposed flow rates of 1.0 and 2.0μl/min is shown in Fig. 6.21b. In all cases, PDMS materials with larger elastic moduli raise the measured system pressure over the entire length of the microchannel.

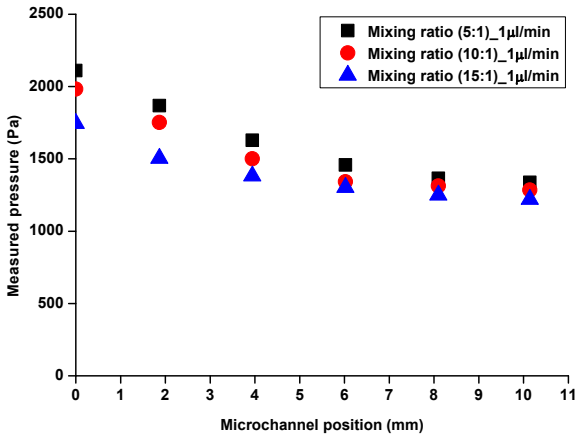

(a)

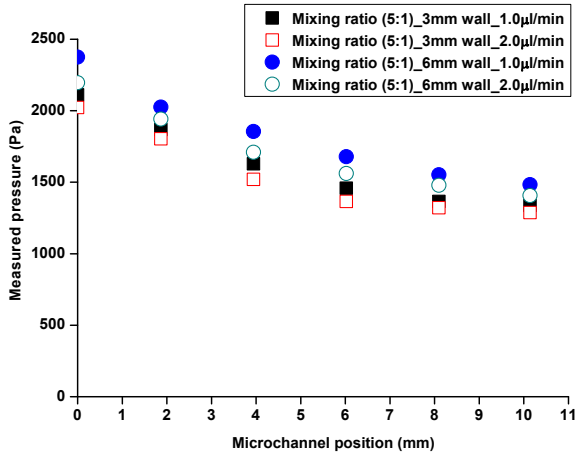

(b)

Figure 6.21 Flow results for developed pressure under various conditions **a** 6mm wall thickness in various mixing ratios at 1.0µl/min **b** different wall thicknesses and flow rates at a single mixing ratio (5:1)

6.2.3 Scaling analysis and finite-element analysis

A complete analytical solution of the Navier-Stokes equation to the coupled fluid-structure problem is too complicated, so a scaling approximation provides a useful estimate of the amount of channel deformation based on pressure-driven flows. The relative equation for the maximum depth variation of a microfluidic channel at any given position was described by Gervais et al. (2006).

$$\frac{\Delta h_{\max}}{h_0} = C_1 \frac{Pw}{Eh_0} \tag{6.5}$$

Where Δh_{max} is the maximum channel height at mid-width of the channel under deformation, h_0 is the initial (undeformed) channel height, w is the channel width, C_1 is an empirical fitting parameter, and E is the Young's modulus of PDMS (i.e., 750KPa). Gervais et al. (2006) show that the microfluidic channel height as a function of any position is dependent on the measured pressure $p(z)$ at those positions as

$$h(z) = h_0 \left(1 + \alpha \frac{p(z)w}{Eh_0}\right) \tag{6.6}$$

Where $\alpha = 2/3\ C_1$. The value of fitting parameter, C_1, for 1.0μl/min and 2.0μl/min were determined in these experiments as 1.29 and 1.21, respectively.

2D finite element simulations of the interaction between the liquid pressure and the flexible PDMS channel deformation were performed using the commercial software (ANSYS Workbench, NH, USA). The simplified geometry and mesh (3,277 nodes and 1,032 elements) used in this study is shown in Fig. 6.22. A mesh refinement study indicated that a mesh of 3,277 nodes and 1,032 elements would reliably simulate the current structure (Dadkhah and Zecher 2009). The PDMS structure used for channel

deformation measurements was created with two different wall thicknesses (3mm and 6mm) with a microchannel a depth of 50μm and width of 243μm. Poisson ratio was assumed as equal to 0.49. Numerical simulations used as elastic modulus of 750kPa (Choi and Park 2009) as well as the experimentally determined value. Both sidewalls were set as a free boundary condition, while the bottom wall between the PDMS structure and glass slide was set as a fixed support because the PDMS channels were strongly bonded to the glass slide.

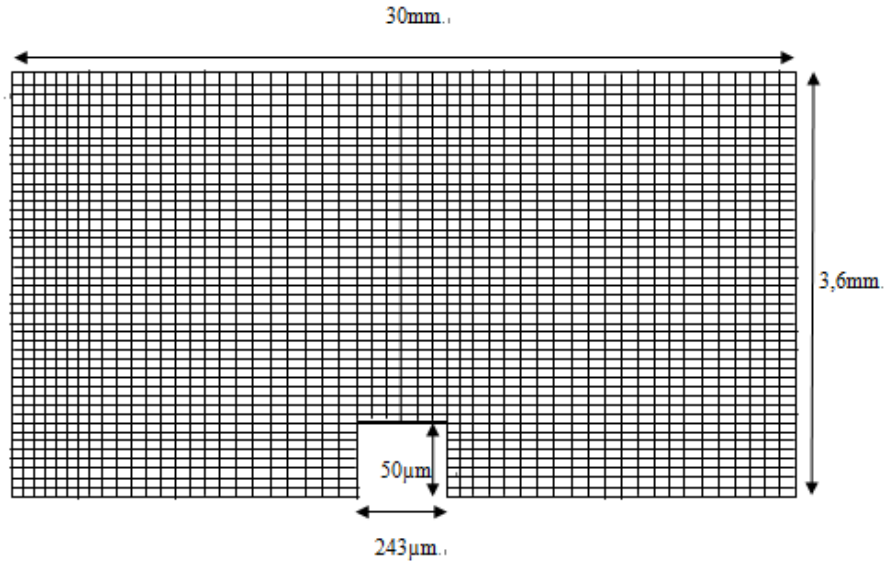

Figure 6.22 Geometry and mesh in ANSYS Workbench software for microfluidic channel deformations

A comparison of the predicted channel deformation along the entire channel length by the scaling analysis and the finite element analysis is shown in Fig. 6.23. These calculations were for a 10:1 mixing ratio, 6mm wall thickness of the microfluidic chip and a microchannel depth of 50μm. The maximum microchannel bulging is predicted at the inlet, as expected. In addition, good agreement is seen between the two approaches –

especially for the 2μl/min flow rate case. A slightly larger channel deformation is also predicted for the 2μl/min flow rate case.

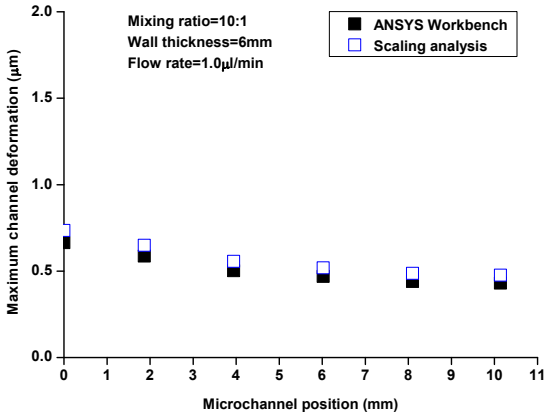

(a)

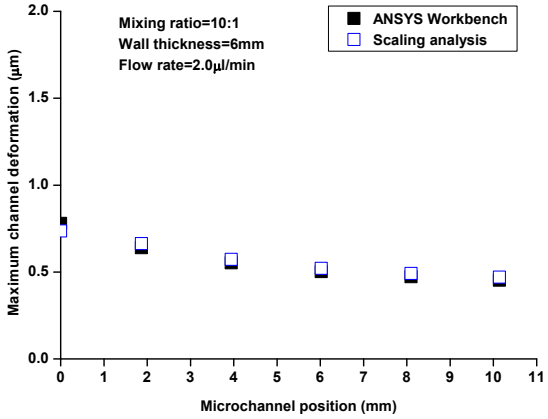

(b)

Figure 6.23 Analysis of finite element method and scaling analysis for FC2 50μm channel depth with the mixing ratio (10:1) and wall thickness (6mm) **a** flow rate at 1.0μl/min (c_1: 1.29) **b** flow rate at 2μl/min (c_1: 1.21)

A quantitative comparison of the experimentally measured microchannel bulging deformation along the microchannel length versus the ANSYS predicted bulging deformation is shown in Fig. 6.24 and Fig. 6.25. Figure 6.24 examines the effects of PDMS wall thickness and imposed flow rate while Fig. 6.25 characterizes the effects of PDMS mixing ratio and imposed flow rate. The experimentally measured bulging

deformation is generally greater than the ANSYS predicted values for all conditions. The best agreement is seen in the case with the lower flow rate, minimum bulging and maximum stiffness (Fig. 6.25a).

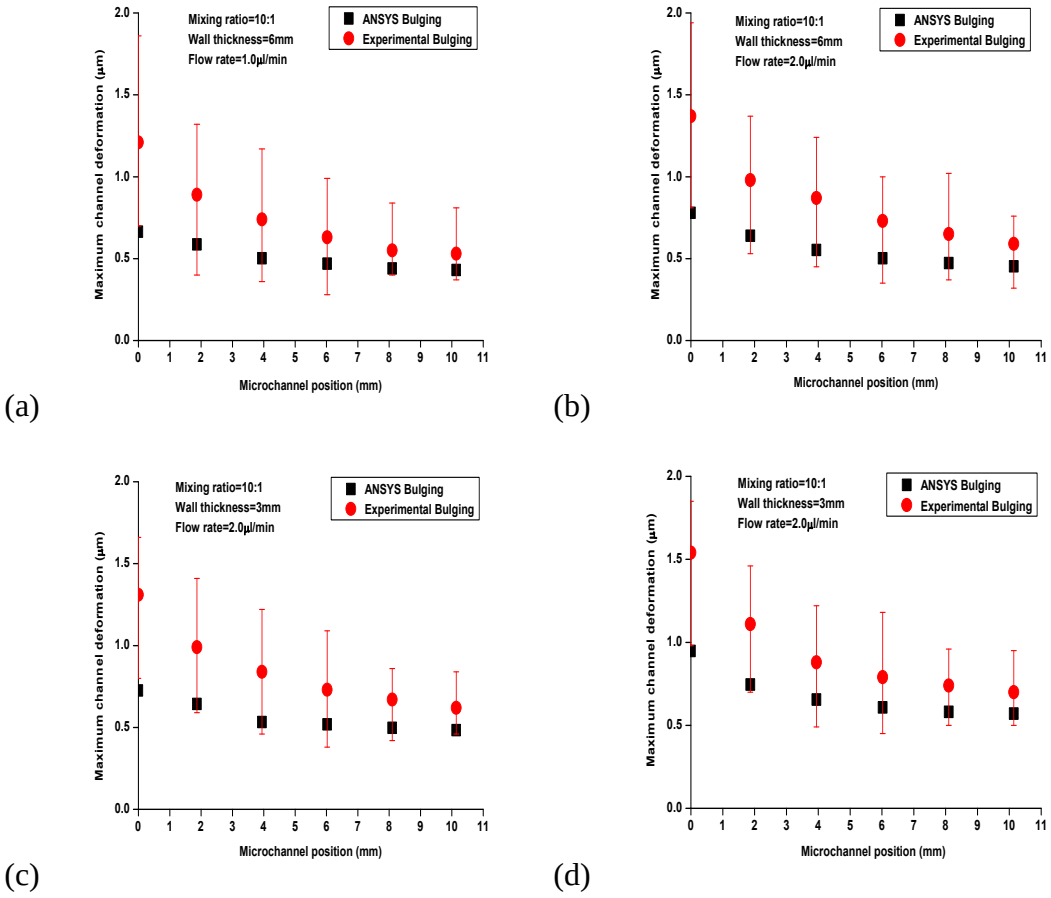

Figure 6.24 Analysis of 50µm depth of PDMS microfluidic channel bulging using two wall thicknesses (mixing ratio=10:1) **a** 6mm wall thickness at 1.0µl/min **b** 6mm wall thickness at 2.0µl/min **c** 3mm wall thickness at 1.0µl/min **d** 3mm wall thickness at 2.0µl/min

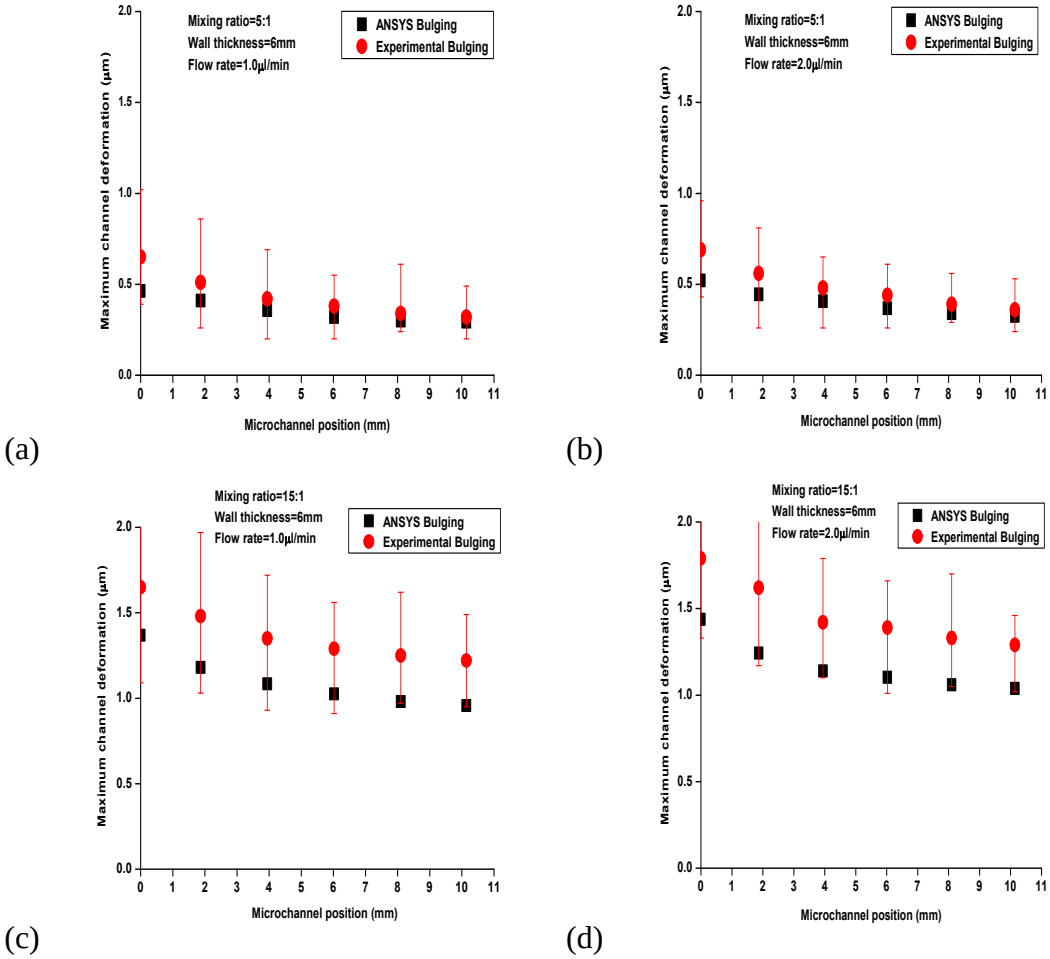

Figure 6.25 Analysis of 50µm depth of PDMS microfluidic channel bulging using various mixing ratios (wall thickness: 6mm) **a** mixing ratio (5:1) at 1.0µl/min **b** mixing ratio (5:1) at 2.0µl/min **c** mixing ratio (15:1) at 1.0µl/min **d** mixing ratio (15:1) at 2.0µl/min

CHAPTER 7

CONCLUSION

Although time consuming and tedious, tracking of the position and velocity of a liquid front during start-up flow in a microchannel using optical microscopy is a reliable technique to characterize the position and velocity during start-up flow. Treating the transient flows in these microfluidic channels as a first order system allowed the final quasi-steady flow velocities V_{QS} and pressure drops per unit length $(\Delta P/\Delta x)_{QS}$ to be experimentally determined.

The bulging-modified mean hydraulic diameter was shown to be an effective characteristic length scale for assessing the cross sectional area for flow in these obstacle-laden microfluidic channels. The experimentally determined relationship for Darcy friction factors *f* versus Reynolds number *Re* were found to be a function of microfluidic channel depths. The 200μm microfluidic channel depth exhibited the least bulging deformation and provided relatively good agreement with theoretical predictions of $f \propto Re^{-1}$. The 15μm microfluidic channel depth demonstrated the greatest bulging deformation and exhibited $f \propto Re^{-1.69}$, much greater than expected.

The experimentally determined Darcy friction factors for these low velocity flows were shown to agree with literature data covering approximately 8 orders of magnitude variation of the Reynolds number. The present data are also in agreement with standard

correlations of friction factors with Reynolds numbers for flow through rectangular microfluidic channels, i.e., $56.9/Re \leq f \leq 96/Re$.

PDMS microchannel bulging effects exerted a greater deleterious effect on $(\Delta P/\Delta x)_{QS}$ values than upon V_{QS} for these experiments using a volumetrically controlled syringe pump.

Measurements of bulging displacements of flexible PDMS microchannels using fluorescence microscopy provide a cost effective alternative method to confocal microscopy. Analysis of fluorescent intensity by means of a line scan technique indicated that the shape of the deforming channel was uniformly flat in a rectangular cross-section rather than parabolic as reported by other researchers. Measurements of bulging agreed with theoretical predictions using both the simplified scaling analysis of Gervais et al. (2006) as well as 2D finite element simulations.

Deformation of PDMS microfluidic channels was shown to be dependent on three important physical factors: wall thickness, resin:hardener mixing ratio and applied flow rate. Mixing ratios provided the largest effects while the wall thickness of the PDMS chip showed relatively minimal influence.

CHAPTER 8

SUGGESTIONS FOR FUTURE WORK

- Characterization of the transient start-up flow in deformable PDMS microchannels by modeling the system response as a first order system proved useful and provides opportunities for additional investigations of transient conditions in microfluidic flow. Examples of such interesting applications include microfluidic valve openings and closures and chemical reaction kinetics.
- Measurement of PDMS microfluidic channel bulging and deformation by means of fluorescence intensity can be applied to much more complex systems – for example liquid cooling of microelectronic devices. The data provided an excellent comparison against the finite element analyses in the current work and would be extremely useful in future studies of fluid-structure coupling in microfluidic systems.
- Passive mixing using arrays of obstacles in microfluidic reactors has received considerable recent interest and careful analysis of such systems is possible using the experimental techniques established in the present work. 3D configurations of obstacles are possible and offer promise for dramatic gains in mixing efficiency.
- Microfluidic devices have application for studying bacteria motility and bioflim development in highly idealized geometries with various microchannel surface roughness and chemical environments. The characterization techniques developed in

this work will enable a range of studies of bacterial twitching motility and attachment to channel surfaces.

REFERENCES

Akbari M, Sinton D, Bahrami M (2009) Pressure drop in rectangular microchannels as compared with theory based on arbitrary cross section. J Fluids Engineering 131:041202-1 -041202-8

Ambastha AK, Zhang MY (1996) Iterative and numerical solutions for pressure-transient analysis of stress- sensitive reservoirs and aquifers. Computer and Geoscience 22:601-606

Ansari MA, Kim KY, Anwar K, Kim SM (2010) A novel passive micromixer based on unbalanced splits and collisions of fluid streams. J. Micromech. Microeng. 20:055007

Balagadde FK, You L, Hansen CL, Arnold FH, Quake SR (2005) Long-term monitoring of bacteria undergoing programmed population control in a microchemostat. Science 309:137-140

Bhagat AAS, Peterson ETK, Papautsky I (2007) A passive planar micromixer with obstructions for mixing at low Reynolds numbers. J. Micromech. Microeng.17:1017-1024

Bird RB, Stewart WE, Lightfoot EN (2002) Transport phenomena. John Wiley & Sons Inc, USA

Bubendorfer A, Liu X, Ellis AV (2007) Microfabrication of PDMS microchannels using SU-8/PMMA molding and their sealing to polystyrene substrates. Smart Mater. Struct. 16:367-371

Campbell DJ, Beckman KJ, Calderon CE, Doolan PW, Ottosen RM, Ellis AB, Lisensky GC (1999) Replication and compression of bulk and surface structures with polydimethylsiloxane elastomer. Journal of Chemical Education. 75:537-541

Chen CK, Cho CC (2008) A combined active/passive scheme for enhancing the mixing effiency of microfluidic devices. Chem. Eng. Sci. 63:3081-3087

Chen KS, Ayon A, Zhang X, Spearing S (2002) Effect of process parameters on the surface morphology and mechanical performance of silicon structures after deep reactive ion etching (DRIE). J.Micromech.Microeng. 11:264-275

Clarson SJ, Semlyen JA (1993) Siloxane polymers. Prentice-Hall Inc, USA

Cortes-Quiroz CA, Azarbadegan A, Moeendarbary E (2010) An efficient passive planar micromixer with fin-shaped baffles in the tee channel for wide Reynolds numer flow range. World Academy of Science, Engineering and Technology 61:170-175

Dadkhan F, Zecher J (2009) ANSYS Workbench software. Schroff Developmenmt Corporation, KS, USA

Dangla R, Gallaire F, Baroud CN (2010) Microchannel deformations due to solvent-induced PDMS swelling. Lab Chip 9:935-938

Eddings MA, Johnson MA, Gale BK (2008) Determing the optimal PDMS-PDMS bonding technique for microfluidic devices. . J. Micromech Microeng 18:067001

Gao JX, Yeo LP, Chan-Park MB, Miao JM, Yan YH, Sun JB, Lam YC, Yue CY (2006) Antistick postpassivation of high-aspect-ratio silicon molds fabricated by deep-reactive ion etching. J Micromech. Microeng. 15: 84-93

Gassend BLP, Velásquez-García LF, Akinwande (2010) Design and fabrication of DIRE-patterned complex needlelike silicon structures. J Micromech. Microeng. 19: 589-598

Geankoplis CJ (1993) Transport processes and unit operations. Prentice Hall Inc, USA
Gervais T, El-Ali J, Gunther A, Jensen KF (2006) Flow-induced deformation of shallow microfluidic channel. Lab Chip 6:500-507

Gervais T, El-Ali J, Gunther Axel, Jensen KF (2006) Flow-induced deformation of shallow microfluidic channels. Lab Chip 6:500-507

Gornam DG, Reese JM, Zhang YL (2000) Vibration of a flexible pipe conveying viscous pulsating fluid flow. Journal of Sound and Vibration 2:379-392

Groisman A, Lobo C, Cho H, Campbell JK, Dufour YS, Stevens AM, Levchenko A (2005) Amicrofluidic chemostat for experiments with bacterial and yeast cells. Nature Methods 2:685-689

Hansen CL, Classen S, Berger JM, Quake SR (2006) A microfluidic deivce for kinetic optimization of protein crystallization and in situ structure determination. J. Am. Chem. Soc. 128:42-43

Hardy BS, Uechi K, Zhen J, Kavehpour P (2009) The deformation of flexible PDMS microchannels under a pressure driven flow. Lab Chip 9:935-938

Hocheng H, Chen CM, Chou YC, Lin CH (2010) Study of novel electrical routing and integrated packing on bio-compatible flexible substrate. Microsyst Technol 16:423-430

Holden MA, Kumar S, Beskok A, Cremer PS (2003) Microfluidic diffusion diluter: bulging of PDMS microchannels under the pressure driven flow. J. Micromech.

Microeng. 13:412-418

Holman JP (1989) Experimental Methods for Engineers, McGraw-Hill, New York

Hsieh SS, Lin CY, Huang CF, Tsai HH (2004) Liquid flow in a microchannel. J. Micromech. Microeng. 14:436-445

Huang W, Liu Q, Li Y (2006) Capillary filling flows inside patterned-surface microchannels. Chem. Eng. Technol. 29:716-723

Jacobson S, Hergenroder R, Moore A, Ramsey J (1994) Precolumn reactions with electrophoretic analysis integrated on a microchip. Anal. Chem. 66:4127-4132

Jain M, Yeung A, Nandakumar K (2009) Induced charge electro osmotic mixer: obstacle shape optimization. Biomicrofluidics 3:022413

Jung JY, Kwak HY (2008) Fluid flow and heat transfer in microchannels with rectangular cross section. Heat Mass Transfer 44:1041-1049

Keoschkerjan R, Richter M, Boskovic D, Schnürer F, Lobbecke S (2004) Novel multifunctional microreaction unit for chemical engineering. Chem. Eng. J 101:469-475

Khan MN, Islam M, Hasan MM (2011) Experimental approach to study friction factor and temperature profiles of fluid flow in circular microchannels. Journal of Mechanical Engineering Research 3:209-217

Kim DS, Kwon TH (2006) Modeling, analysis and design of centrifugal force-driven transient filling flow into a circular microchannel. Microfluid Nanofluid 2:125-140

Kim DS, Lee IH, Kwon TH, Cho DW (2004) A barrier embedded kenics micromixer. J. Micromech. Microeng. 14:1294-1301

Kim DS, Lee SW, Kwon TH, Lee SS (2004) A barrier embedded chaotic micromixer. J. Micromech. Microeng. 14:798-805

Kim E, Xia Y, Whitesides G (1995) Polymer microstructures formed by molding in capillaries. Nature 376:581-584

La Fuente LD, Montanes E, Meng Y, Li Y, Burr T, Hoch HC, Wu M (2007) Assessing adhesion forces of type I and type IV pili of xylella fastidiosa bacteria by use of a microfluidic flow chamber. Applied and Environmental Microbiology 73:2690-2696

Lam RHW, Sun Y, Chen W, Fu J (2012) Elastometric microposts integrated into microfluidics for flow-mediated endothelial mechanotransduction analysis. Lab Chip 12:1865-1873

Liu J, Hansen C, Quake SR (2003) Solving the "world-to-chip" interface problem with a microfluidic matrix. Anal. Chem. 75:4718-4723

Liu M, Chen Q (2007) Characterization study of bobded and unbounded polydimethylsiloxane aimed for bio- micro-electromechanical systems-related applications. J. Micro/Nanolith. MEMS MOEMS 6:023008

Liu M, Sun J, Sun Y, Bock C, Chen Q (2009) Thickness-dependent mechanical properties of polydimethylsiloxane membranes. J. Micromech. Microeng. 19:035028

Liu RH, Nguyen T, Schwarzkopf K, Fuji HS, Petrova A, Siuda T, Peyvan K, Bizak M, Danley D, McShea A (2006) Fully integrated miniature device for automated gene expression DNA microarray processing. Anal. Chem. 78:1980-1986

Long T, Ford RM (2009) Enhanced transverse migration of bacteria by chemotaxis in a porous T-sensor. Environ. Sci. Technol. 43:1546-1552

Lötters JC, Olthius W, Veltink PH, Bergveld P (1997) The mechanical properties of the rubber elastic polymer polydimethylsiloxane for sensor applications. J. Micromech. Microeng. 7:145-147

Mala GM, Li D (1999) Flow characteristics of water in microtubes. Int. J. Heat Fluid Flow 20:142-148

Melin J, Quake SR (2007) Microfluidic large-scale integration: The evolution of design rules for biological automation. Annu. Rev. Biophys. Biomol. Struct. 36:213-231

Mello AJD, Habgood M, Lancaster NL, Welton T, Wootton RCR (2004) Precise temperature control in microfluidic devices using Joule heating of ionic liquids. Lab Chip 4:417-419

Moffat, RJ (1988) Describing the uncertainties in experimental results. Experimental Thermal and Fluid Science 1:3-7

Mohammed HA, Gunnasegaran P, Shuaib NH (2011) The impact of various nanofluid types on triangular microchannels heat sink cooling performance. International Communications in Heat and Mass Transfer 38:767-773

Neff H, Lima AMN, Loureiro FCCL, Almeida LAL (2007) Transient response analysis and modeling of near wall flow conditions in a microchannel: evidence of slip flow. Microfluid Nanofluid 3:591-602

Nguyen NT, Wereley ST (2006) Fundamentals and applications of microfluidics. Artech House USA

Nguyen NT, Wu Z (2005) Micromixers-a review. J. Micromech. Microeng 15:R1-R16

Papautsky I, Gale BK, Mohanty S, Ameel TA, Frazier BA (1999) Effects of rectangular microchannel aspect ratio on laminar friction constant. Proceedings of SPIE 3877:147-158

Peiyi W, Little WA (1983) Measurement of friction factors for the flow of gases in very fine channels used for microminiature Joule-Thomson refrigerators. Cryogenics 5:273-277

Peng XF, Peterson GP, Wang BX (1994) Frictional flow characteristic of water flow through rectangular microchannels. Experimental Heat Transfer 7:249-264

Qu W, Mala GM, Li D (2000) Pressure-driven water flows in trapezoid silicon microchannels. Int. J. Heat Mass Transfer 43:3925-3936

Reyes D, Iossifidis D, Auroux PA, Manz A (2002) Micro total analysis systems. 1. Introduction, theory, and technology. Anal. Chem. 74:2623-2636

Sharma K, Müller N, Selerowicz W (2006) Experimental friction factor study for microchannel flows. 6th International workshop for Micro and Nanotechnology for power generation and energy conversion applications. Berkeley USA

Singh R, Olson MS (2011) Transverse mixing enhancement due to bacterial random motility in porous microfluidic devices. Environ. Sci. Technol. 45:8780-8787

Skelley AM, Scherer JR, Aubrey AD, Grover WH, Ivester RHC (2005) Development and evaluation of a microdevice for amino acid biomarker detection and analysis on Mars. Proc. Natl. Acad. Sci. USA 102:1041-1046

Steinke ME, Kandlikar SG (2006) Single-phase liquid friction factors in microchannels. International Journal of Thermal Sciences 45:1073-1083

Streeter VL, Wylie EB (1975) Fluid Mechanics, McGraw-Hill, New York

Suh YK, Kang S (2010) A review on mixing in microfluidics. Micromachines 1:82-111

Tabeling P (2005) Introduction to microfluidics. Oxford University Press, USA

Thangawng AL, Ruoff RS, Swartz MA, Glucksberg MR (2007) An ultra-thin PDMS membrane as a bio/micro- nano interface: fabrication and characterization. Biomed Microdevices 9:587-595

Thompson LF, Wilson CG, Bowden MJ (1994) Introduction to microlithography. American Chemical Society, Washington D.C.

Thorsen T (2003) Microfluidic technologies for high-thourghput screening applications. Ph.D thesis. Calif. Inst. Tech 155

Tijsseling AS (1996) Fluid-structure interaction in liquid-filled pipe systems: a review. Journal of Fluids and Structures 10:109-146

Tseng LY, Yang AS, Lee CY, Hsieh CY (2011) CFD-based optimization of a diamond-obstacles inserted micromixer with boundary protrusions. Engineering Application of Computational Fluid Mechanics 5:210-222

Tung YC, Zhang M, Lin CT, Kurabayashi K, Skerlos S (2004) PDMS-based opto-fluidic micro flow cytometer with two-color, multi-angle fluorescence detection capability using PIN photodiodes. Sensors and Actuators B 98:356-367

Unger MA, Chou HP, Thorsen T, Scherer A, Quake SR (2000) Monolithic microfabricated valves and pumps by multilayer softlithography. Science 288:113-116

Van Krevelen DW and Hoftyzer (1976) Properties of polymers. Elsevier, USA

Wang H, Iovenitti P, Harvey E, Masood S (2003) Passive mixing in microchannels by applying geometric variations. Proceedings of SPIE 4982:282-289

Wang L, Zhang M, Yang M, Zhu W, Wu J, Gong X, Wen W (2009) Polydimethylsiloxane-integratable micropressure sensor for microfluidic chips. Biomicrofluidics 3: 034105

Wang X, Chen X, Ma X, Kong X, Xu Z, Wang J (2011) Fast DNA hybridization on a microfluidic mixing device based on pneumatic driving. Talanta 84:565-571

White, FM (1994) Fluid Mechanics. McGraw-Hill, New York

Wu GW, Shih WP, Hui CY, Chen SL, Lee CY (2010) Bonding strength of pressurized microchannels fabricated by polydimethylsiloxane and silicon. J Micromech Microeng 20:115032

Wu H, Cheng P (2003) Friction factors in smooth trapezoidal silicon microchannels with different aspect ratio. Int. J. Heat Mass Transfer 46:2519-2525

Yang CY, Wu JC, Chien HT, Lu SR (2003) Friction characteristics of water, R-134a, and air small tubes. Microscale. Thermophy. Eng. 7:335-348

Yeom J, Agonafer DD, Han JH, Shannon MA (2009) Low Reynolds numbers flow across an array of cylindrical microposts in a microchannel and figure-of-merit analysis of micropost- filled microreactors. J. Micromech. Microeng. 19:065025

Yun JY, Jambovane S, Kim SK, Cho SH, Duin EC, Hong JW (2011) Log-scale dose response of inhibitors on a chip. Analytical Chemistry 83:6148-6153

Zhang Y, Vairavamoorthy (2005) Analysis of transient flow in pipelines with fluid-structure interaction using method of lines. Int. J. Numer. Meth. Engng. 63:1446-1460

APPENDICS

APPENDIX A ANALYSIS OF PDMS DEFORMATION BY DIFFERENT METHODS

Table A.1 Comparison of PDMS deformation measurement results by two methods

	Fluorescence microscopy	Confocal microscopy		Fluorescence microscopy	Confocal microscopy	
	1.0μl/min	1.0μl/min	Difference (%)	2.0μl/min	2.0μl/min	Difference (%)
FC2	1.53	1.62	5.61	1.84	1.96	6.53
FC3	1.39	1.46	5.10	1.69	1.78	5.50
FC4	0.65	0.68	4.67	1.39	1.46	4.93
FH2	1.45	1.54	5.92	1.92	2.04	6.13
FH3	1.33	1.40	5.43	1.77	1.87	5.45
FH4	1.17	1.23	5.38	1.35	1.42	5.42
FS2	1.70	1.81	6.52	2.11	2.25	6.67
FS3	1.33	1.41	5.79	1.80	1.91	5.88
FS4	1.05	1.10	4.40	1.71	1.80	5.12
FT2	1.31	1.39	5.77	1.41	1.49	5.90
FT3	1.12	1.18	4.96	1.19	1.25	5.01
FT4	0.84	0.88	4.86	0.98	1.03	4.96

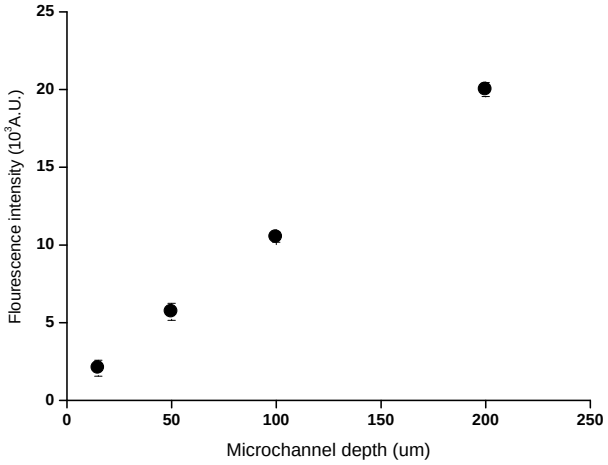

Figure A.1 Florescence intensity difference based on microchannel depths

APPENDIX B ANALYSIS OF CAPILLARY EFFECTS

Table B.1 Comparison of theoretical and experimental capillary pressure drops

	Predicted contact angle (°)		Theoretical capillary pressure drop (kPa)	Experimental capillary pressure drop (kPa)	
	1.0μl/min	2.0μl/min		1.0μl/min	2.0μl/min
FC2_15μm	79	78	1.91-2.23	2.00	2.23
FC2_50μm	71	69	1.91-2.09	1.86	2.06
FC2_100μm	67	64	1.80-1.94	1.75	1.96
FC2_200μm	64	61	1.68-1.80	1.73	1.91
FC3_15μm	79	78	2.14-2.49	1.98	2.21
FC3_50μm	69	67	1.82-1.98	1.77	1.92
FC3_100μm	63	60	1.74-1.85	1.72	1.88
FC3_200μm	60	57	1.56-1.66	1.68	1.83
FC4_15μm	79	77	2.04-2.38	1.95	2.18
FC4_50μm	68	66	1.65-1.79	1.69	1.86
FC4_100μm	61	58	1.57-1.72	1.61	1.78
FC4_200μm	60	58	1.33-1.41	1.59	1.77

APPENDIX C DIFFERENCE OF CHANNEL DEFORMATION

Table C.1 Comparison of % difference from an original channel depth (FC2 50μm) (Mixing ratio=10:1, PDMS wall thickness=6mm, flow rate=1.0μl/min)

	1.0μl/min					
Microchannel position (mm)	Scaling analysis (μm)	FEA analysis (μm)	Experimental measurement (μm)	Scaling analysis (%)	FEA analysis (%)	Experimental measurement (%)
0	0.74	0.71	1.28	1.48	1.42	2.56
1.87	0.65	0.58	0.85	1.30	1.16	1.70
3.94	0.53	0.49	0.74	1.06	0.98	1.48
6.02	0.50	0.48	0.65	1.00	0.96	1.30
8.10	0.49	0.47	0.53	0.98	0.94	1.06
10.1	0.48	0.46	0.51	0.96	0.92	1.02

Table C.2 Comparison of % difference from an original channel depth (FC2 50μm) (Mixing ratio=10:1, PDMS wall thickness=6mm, flow rate=2.0μl/min)

	2.0μl/min					
Microchannel position (mm)	Scaling analysis (μm)	FEA analysis (μm)	Experimental measurement (μm)	Scaling analysis (%)	FEA analysis (%)	Experimental measurement (%)
0	0.72	0.78	1.31	1.44	1.56	2.62
1.87	0.68	0.66	1.02	1.36	1.32	2.04
3.94	0.55	0.52	0.85	1.10	1.04	1.70
6.02	0.53	0.51	0.73	1.06	1.02	1.46
8.10	0.50	0.49	0.69	1.00	0.98	1.38
10.1	0.49	0.48	0.61	0.98	0.96	1.22

APPENDIX D ANALYSIS OF CURVE FITTING

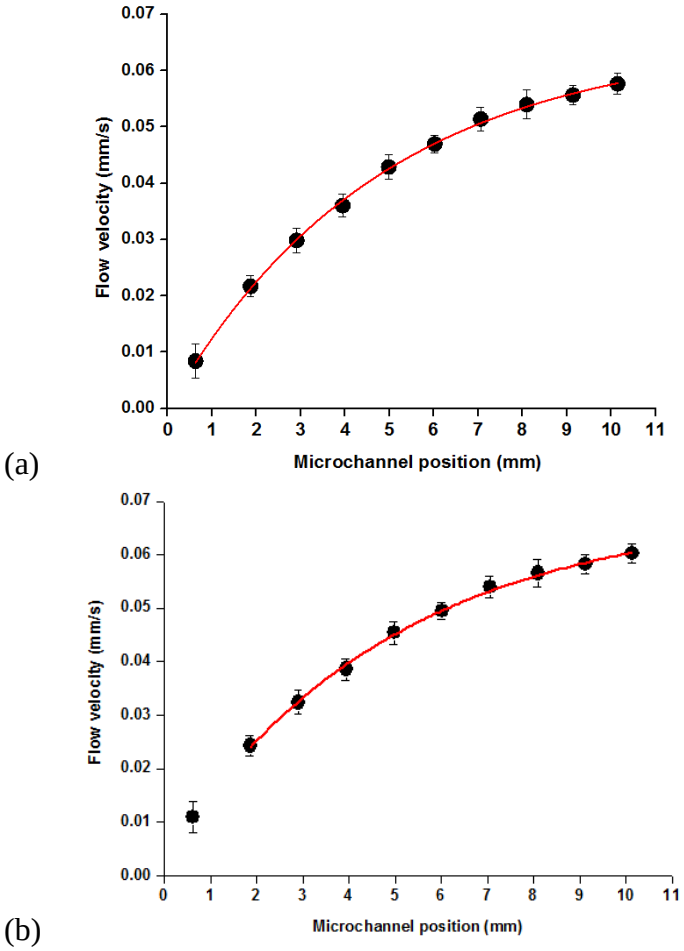

Figure D.1 a Analysis of transient flow velocity (FC2 50µm) at flow rate 1.0µl/min with capillary effects **b** analysis of transient flow velocity (FC2 50µm) at flow rate 1.0µl/min without capillary effects

(a)

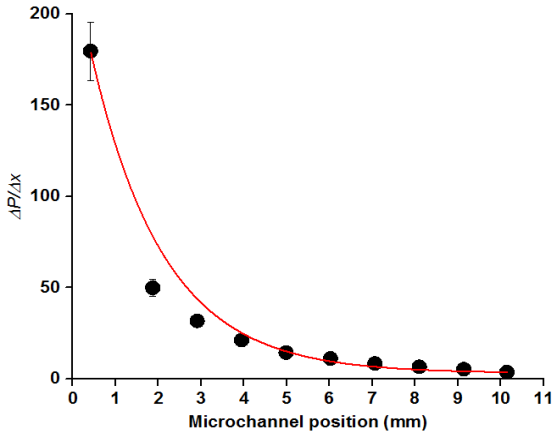

(b)

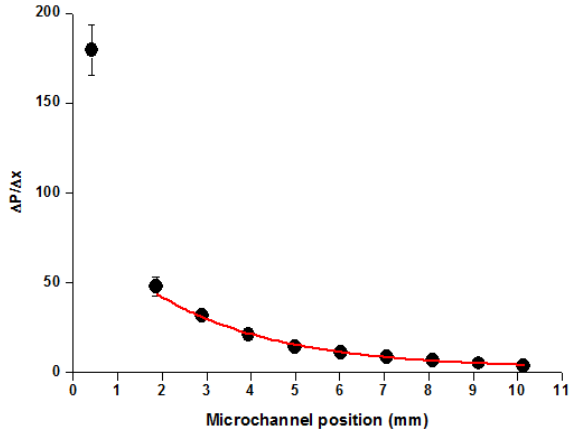

Figure D.2 a Analysis of transient pressure data (FC2 50µm) at flow rate 1.0µl/min with capillary effects **b** analysis of transient pressure data (FC2 50µm) at flow rate 1.0µl/min without capillary effects

Table D.1 Analysis of transient flow velocity and pressure data with/without capillary effect

	1.0μl/min	
	With capillary effects	Without capillary effects
V_{QS}	0.065 mm/s	0.069 mm/s
X_{DV}	4.75	4.86
R^2	0.988	0.998
$(\Delta P/\Delta x)_{QS}$	3.00 Pa/mm	3.42 Pa/mm
X_{DP}	1.70	2.19
R^2	0.932	0.998

APPENDIX E FRICTION FACTOR (*f*) AS FUNCTION OF REYNOLDS NUMBER (*Re*) WITH THE AS-FABRICATED HYDRAULIC DIAMETERS

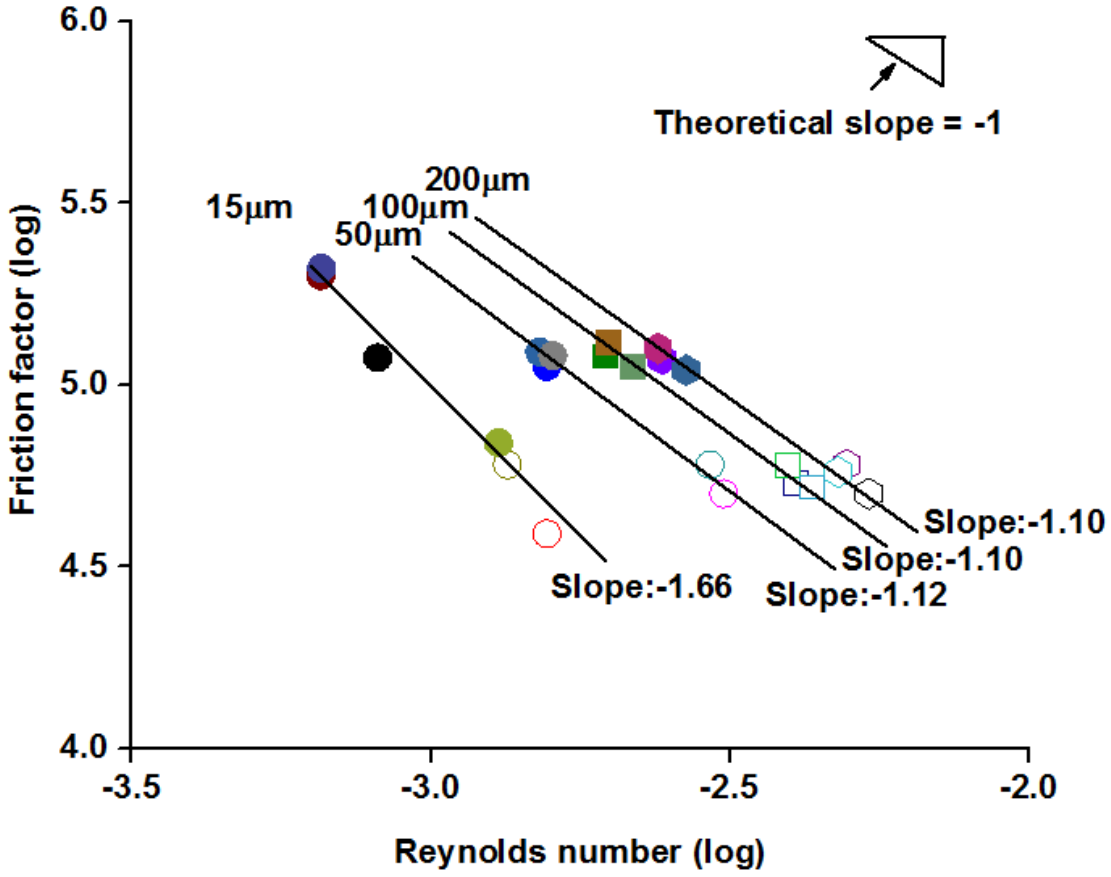

Figure E.1 Friction factor (*f*) as function of Reynolds numer (*Re*) for four different microfluidic channel depths using the as-fabricated hydraulic diameters